University of Alberta

Magnetization dynamics in the presence of nanoscale spatial inhomogeneity

by

Zhigang Liu ©

A thesis submitted to the Faculty of Graduate Studies and Research
in partial fulfillment of the requirements for the degree of

Doctor of Philosophy

Department of Physics

Edmonton, Alberta
Fall 2007

Library and
Archives Canada

Published Heritage
Branch

395 Wellington Street
Ottawa ON K1A 0N4
Canada

Bibliothèque et
Archives Canada

Direction du
Patrimoine de l'édition

395, rue Wellington
Ottawa ON K1A 0N4
Canada

Your file Votre référence
ISBN: 978-0-494-33019-7
Our file Notre référence
ISBN: 978-0-494-33019-7

NOTICE:
The author has granted a non-exclusive license allowing Library and Archives Canada to reproduce, publish, archive, preserve, conserve, communicate to the public by telecommunication or on the Internet, loan, distribute and sell theses worldwide, for commercial or non-commercial purposes, in microform, paper, electronic and/or any other formats.

The author retains copyright ownership and moral rights in this thesis. Neither the thesis nor substantial extracts from it may be printed or otherwise reproduced without the author's permission.

AVIS:
L'auteur a accordé une licence non exclusive permettant à la Bibliothèque et Archives Canada de reproduire, publier, archiver, sauvegarder, conserver, transmettre au public par télécommunication ou par l'Internet, prêter, distribuer et vendre des thèses partout dans le monde, à des fins commerciales ou autres, sur support microforme, papier, électronique et/ou autres formats.

L'auteur conserve la propriété du droit d'auteur et des droits moraux qui protège cette thèse. Ni la thèse ni des extraits substantiels de celle-ci ne doivent être imprimés ou autrement reproduits sans son autorisation.

In compliance with the Canadian Privacy Act some supporting forms may have been removed from this thesis.

While these forms may be included in the document page count, their removal does not represent any loss of content from the thesis.

Conformément à la loi canadienne sur la protection de la vie privée, quelques formulaires secondaires ont été enlevés de cette thèse.

Bien que ces formulaires aient inclus dans la pagination, il n'y aura aucun contenu manquant.

Canada

Reproduced with permission of the copyright owner. Further reproduction prohibited without permission.

Abstract

Magnetization dynamics in various ferromagnetic thin film samples is investigated using time-resolved magneto-optical Kerr effect microscopy. The results have sub-picosecond time resolution and sub-micrometer spatial resolution, and are successfully compared with micromagnetic simulations. Related theoretical models and calculations are also discussed.

There are two types of spatial inhomogeneity that influence the observed magnetization dynamics. In the first project, the magnetic sample is a uniform, continuous thin film, but the excitation magnetic pulse is highly localized within several micrometers (in one dimension). Different types of spin waves can be excited depending on the relation between the bias magnetic field and the wave vector, and they can be quantitatively described by micromagnetic simulations. A semi-analytical *k*-space integration method is also proposed; this method is effectively as accurate as those obtained by micromagnetic simulations, but can save a great deal of time and computer resources. It is also found that a single magnetic damping constant is enough to interpret all the observed phenomena, although their apparent damping may look very different.

The second type of spatial inhomogeneity means that the sample itself is

patterned into very small elements with the diameters less than 200 nm, while the excitation pulse is relatively uniform. The nanomagnets (nanodisks in this case) are either in quasi-single domain state or in vortex state at equilibrium, and they can switch from one to another by changing the applied bias field. As a result, the magnetization dynamics and associated frequencies will change dramatically when the state transitions (vortex annihilation and vortex nucleation) occur. The real shape of the nanodisks characterized by a "domed" top, rather than the normal "flat" top cylinder model, needs to be considered in micromagnetic simulations to accurately reproduce the critical fields for both vortex annihilation and nucleation. The physical nature of these phenomena is also discussed based on the simulated results.

Acknowledgements

The years I've been a graduate student of the University of Alberta meant a lot more to me than just taking courses, doing projects and making a Ph.D degree entitled. What's really invaluable, say after many years, will be those unforgettable faces engraved in my mind, those never hesitated to stand beside me through all the progresses, confusions, difficulties and happiness. I'm glad to have a couple of pages to write down my thanks, but I know they are not enough – actually there won't be such a place except my own heart.

I want to thank my supervisor, Prof. Mark Freeman, who cares every detail through my study and research with his unique enthusiasm, patience and professionalism. His unbelievable insight on the field of magnetic materials and dynamics has been inspiring me in such a global and sophisticated way that I would never made it by myself.

I want to thank Prof. Richard Sydora, who has been my co-supervisor and has used his great vision as a theorist to help me with my research projects, especially on computational physics. Richard and Mark can always show me different angles of thinking and then multiphase suggestions, and I believe not every student can benefit from such mentoring.

I'm also lucky enough to be a member of a wonderful group. I would like to thank Dr. Xiaobin Zhu for his warmhearted help and talented suggestions. I thank Dr. Feng Wang, Dr. Fabian Giesen, Dr. Miroslav Belov, Dr. David Fortin, Dr. Greg Ballentine, Dr. Sasha Krichevsky, Dr. Wayne Hiebert and Dr. Kristen Buchanan. And I have special thanks to Ms. Lynn Chandler who has been so nice to me and has helped me in many things. Without any of you, there would have been much less success on my research, and more importantly, there would have been much less fun.

I would like to thank other faculties who offered help with my Ph.D projects and program monitoring, especially Prof. Marek Malac (who also works in NINT) and Prof. Frank Hegmann. Frank's former postdoc fellow, Dr. Markus Walther, and students Jianbo Gao and Grey Arnup, also helped me a lot.

I would like to thank the "super"-technicians, Don Mullin and Greg Popowich, who have created a professional *and* funny culture for all the people working in their lab, and again I'm so lucky to be one of them.

A significant part of my work was done in the Nanofab of the University of Alberta, and I would like to thank the great staff there, especially Stephanie Bozic and Keith Franklin who have been so patient and generous to train me and help me. There were other users in the Nanofab who had their own work to do but never hesitated to give a hand to me; for example, Hue Nguyen kindly helped me to do the EBL fabrication when I was preparing the nanomagnet samples, which was a key step in the entire project.

I also thank Daniel Salamon, who was operating NINT's high-resolution SEM and helped me to inspect the nanomagnet samples.

Last but not the least, I want to thank the collaborating colleagues from other institutes. Dr. Marco Beleggia, from Prof. Yimei Zhu's group in the Brookhaven National Lab, showed me very neat results on calculating the volume-average demagnetization field, which formed the basis of the relevant content in Chapter 2 of this thesis. Prof. Bret Heinrich from Simon Fraser University, and his students Oleksander Mosendz and Bartek Kardasz, provided their multilayer samples made by MBE and offered an opportunity to investigate them using our TRMOKE experiment, which will be a valuable extension for the work discussed in this thesis.

Again, thank you, my dear friends.

Table of contents

List of figures

List of symbols and abbreviations

α: Gilbert's damping constant

Δ: the gap between the planes of the Permalloy film and the coplanar transmission lines

ε: energy density (functional)

ε_K : Kerr ellipticity

γ: gyromagnetic ratio

λ: Landau-Lifshitz damping coefficient

μ: magnetic dipole moment

μ_B: Bohr magneton

θ_K : Kerr rotation angle

τ: (intrinsic) magnetic damping rate

ψ: magnetostatic potential (in Walker's theory)

A_x: exchange stiffness coefficient

BLS: Brillouin light scattering

e: electron charge; base of natural logarithm

EBL: electron beam lithography

FFT: fast Fourier transforms

FMR: ferromagnetic resonance

g: the g-factor

$\hbar$: Planck's constant

IPA: isopropyl alcohol

k_B: Boltzmann constant

LLG: Landau-Lifshitz-Gilbert (equation)

MFM: magnetic force microscopy

MRFM: magnetic resonance force microscopy

M_s: saturation magnetization

MSBVW: magnetostatic backward volume waves

MSSW: magnetostatic surface waves

$\mathcal{N}$: demagnetization tensor

N.A.: numeric aperture

NSOM: near-field scanning optical microscopy

ODE: ordinary differential equation

PMMA: polymethylmethacrylate

SEM: scanning electron microscopy

SEMPA: scanning electron microscopy with polarization analysis

SP-STM: spin polarized scanning tunneling microscopy

SQUID: superconducting quantum interference device

STXM: scanning transmission X-ray microscopy

T_c: Curie temperature

TRMOKE: time-resolved magneto-optical Kerr effect (microscopy)

TRSKEM: time-resolved scanning Kerr effect microscopy

v_g: group velocity

v_p: phase velocity

X-PEEM: X-ray photoemission electron microscopy

YIG: yttrium iron garne

Chapter 1

Background introduction

1.1. Motivations

The last two decades have seen a phenomenal bloom of research on magnetism and magnetic materials. Condensed matter physicists have realized that the magnetic nature of electrons, a.k.a. spins, can be used as a new degree of freedom (other than electric charge) to carry and process information, opening a new field known as magnetoelectronics or spintronics [Berger1996, Slonczewski1996, Zutic2004, Johnson2005]. This idea calls for deeper investigations on magnetic systems themselves and their interactions with surrounding nonmagnetic media. In the same period, new technologies and instruments have been developed and have made great advances on *microscopic* material synthesis, fabrication, inspection and manipulation. Now researchers are able to make and study systems smaller than one nanometer (i.e., size of single atoms or molecules), and many new phenomena and open questions have arisen in the presence of such nanoscale spatial confinements.

There are also other driving forces, such as invention of new magnetic materials, novel magnetic phenomena in organic and biological objects, rapidly growing power of computers, etc. Today's magnetism has become an interdisciplinary test-bed, attracting wide interests and offering exciting opportunities for fundamental physics, nanotechnology, material engineering, computer simulation techniques and much more.

1.2. Brief survey on studies of spin wave dynamics

A magnetic system usually consists of a very large number ($O(10^{23})$) of electron spins which interact nonlinearly with each other via many different mechanisms, so to exactly describe the associated phenomena has been formidably difficult. In 1930, Bloch introduced the concept of spin wave as the elementary excitation in magnetism [Bloch1930]. This idea has been so important because the dynamics in any magnet, which is usually excited out of its static state, can be written in terms of (sinusoidal) spin waves (Taylor's expansion); based on this representation, the dynamics can be greatly simplified by using, for example, well-developed Fourier transform techniques. In 1935, Landau and Lifshitz proposed the equation of motion (LL equation) under a classical interpretation [Landau1935]. Spin wave solutions under specific geometries can be derived by linearization of the LL equation with proper boundary conditions (Maxwell equations). Gilbert also made an important contribution by proposing an equation of motion conditionally equivalent to that of Landau and Lifshitz (therefore it is known as LL equation of Gilbert form or simply LLG equation) [Gilbert1955]. Using the LLG equation, the energy loss of a magnetic system is addressed by a dimensionless, phenomenological damping coefficient, α. Other forms of equation of motion were also developed due to, for example, Bloch and Bloembergen [Bloch1946, Bloembergen1950]. Based on these theories, some pioneering studies were carried out by Feynman, Kittel, Herring, Rado, Walker etc. to determine the properties of spin waves (dispersion laws, spectral densities) in ferromagnetic thin films [Herring1951, Walker1957]. Spin wave modes in which *magnetostatic* interaction plays a dominant role, such as those first studied by and named after Damon and Eshbach [Damon1961], have been attracting wide interest since then. There were also a great deal of contributions on the more complicated dipole-exchange spin waves, such as those due to De Wames and Wolfram [DeWames1970], and those generalized by Kalinikos and Slavin for arbitrary bias field orientation (with respect to the wave vector and thin film plane) [Kalinikos1986].

Ferromagnetic resonance was experimentally observed as early as 1946 by Griffiths [Griffiths1946] and then by Yager *et al.* [Yager1950]. Magnetic reversal experiments also appeared a little later [Smith1958], where an oscilloscope was already able to show the time-resolved magnetization change of a Permalloy film. Non-metallic ferrimagnet yttrium iron garnet (YIG) has also been intensively studied over many decades partially because of its very low damping ($\alpha \sim 10^{-4}$). In addition, YIG samples are perfect for studying highly nonlinear spin wave phenomena. With the deeper involvement of nanotechnology, new techniques have been developed in the demand of investigating *microstructured* magnetic samples. For static magnetic properties, there are powerful tools such as scanning SQUID microscopy [Kirtley1995, Kirtley1999, Woods2001], magnetic force microscopy (MFM) [Seo2005], scanning electron microscopy with polarization analysis (SEMPA) [Scheinfein1991] and spin-polarized scanning tunneling microscopy (SP-STM) [Bode1999]. To investigate the dynamics in real time, the successful techniques include scanning Kerr effect microscopy [Hiebert1997, Acremann2000, Choi2001], micro-focus Brillouin light scattering (BLS) [Demidov2004, Perzlmaier2005], and various inductive FMR techniques [Silva1999]. In 1997, Hiebert *et al.* performed the first spatiotemporal spin wave measurement on an 8

μm Permalloy disk [Hiebert1997]. The frequency information can be deduced from the time-domain data by Fourier transform analyses. This type of investigations has also been done on other micrometer-scale disks, squares, rings, narrow strips, etc. [Park2002, Choe2004, Perzlmaier2005, Neudecker2006a, Neudecker2006b]. Buess *et al.* adopted a useful Fourier transform technique to resolve both the amplitudes and phases of the time-domain data from a Permalloy disk, such that the spatial distributions of individual spin wave modes can be separated (mode reconstruction) [Buess2004]. Continuous films excited by a tiny excitation source are also interesting and challenging in detection, such as the work of Covington *et al.* who demonstrated the Damon and Eshbach modes in real time and space [Covington2002]. For the technologically important switching dynamics, it has been shown that domain wall motion (not small-amplitude spin waves) is the dominant mechanism; but even in such problems, the LLG formalism has still been successful, and many concepts and techniques in spin wave studies remain useful [Choi2001, Schumacher2003a, Schumacher2003b, Gerrits2002].

Other than spin wave dynamics, some recent outstanding accomplishments in magnetism are worthy to be listed below for a more general view (a very limited list, of course): magnetic behavior of a single molecule has been measured by superconducting quantum interference devices (SQUID) [Wernsdorfer2000]; magnetic resonance force microscopy (MRFM) is now able to detect signals from virtually a single spin [Sidles1992, Rugar2004]; time-resolved measurements have been achieved on nanomagnet dynamics driven by a spin-polarized current [Krivorotov2005]; Bose-Einstein condensation of spin wave modes has been experimentally observed [Demokritov2006, Dzyapko2007]. Most of these cutting-edge developments need thorough knowledge of magnetic dynamics on very small scales.

1.3. About this thesis

The present work aims to addressing some of the widely-concerned issues on the spatiotemporal dynamics in ferromagnetic thin film samples using magneto-optic measurements. Basic theoretical discussions are presented in the next Chapter. Most texts just follow the existing theories, but certain problems are closely related to the subsequent experimental work and will be discussed based on the author's own derivations. The appendix of Chapter 2 presents a formalism for calculating volume-average demagnetization tensors, which belongs to one of the kernel problems in micromagnetic simulation. Chapter 3 introduces the experimental aspects of this work, including sample preparation and experimental methods. Chapter 4 presents the results on the magnetostatic spin waves in a Permalloy thin film excited by a micrometer-scale transmission line structure, and Chapter 5 presents the results on the spin dynamics in 10^2-nm-scale Permalloy nanomagnets. Note the different types of inhomogeneities: in Chapter 4 the sample is a uniform continuous film but the excitation pulse is highly localized, while in Chapter 5 the sample itself is spatially confined but the excitation is rather uniform. Clearly, both of these spatial inhomogeneities are important for fundamental research and applications, and the conclusion remarks on them are presented in Chapter 6.

Chapter 2

Theoretical basis and numerical calculations

2.1. The basic equation

A magnetic dipole moment $\boldsymbol{\mu}$ behaves like a spinning top in a magnetic field $\boldsymbol{H}$, driven by a torque in the form of

$$\boldsymbol{T} = \boldsymbol{\mu} \times \boldsymbol{H} \qquad (2\text{-}1)$$

The torque is the time derivative of the angular momentum:

$$\boldsymbol{T} = \frac{d\boldsymbol{L}}{dt} \qquad (2\text{-}2)$$

so Eq.(2-1) can be written as

$$\frac{d\boldsymbol{\mu}}{dt} = \gamma \boldsymbol{\mu} \times \boldsymbol{H} \qquad (2\text{-}3)$$

where γ is the gyromagnetic ratio (of the magnetic dipole moment to the mechanical angular momentum):

$$\gamma = \frac{\boldsymbol{\mu} \cdot \boldsymbol{L}}{L^2} \qquad (2\text{-}4)$$

Fundamentally, $\boldsymbol{\mu}$ stems from electron's intrinsic spin angular momentum $\boldsymbol{s}$. If classical mechanics was good enough to describe an electron, Eq.(2-4) would have led to

$$\gamma_{\text{classical}} = -\frac{e}{2m_e} \qquad (2\text{-}5)$$

However this is not true, since an electron is not a classical sphere whose angular momentum can be deduced classically; quantum electrodynamics has to take over here to capture the right picture, which introduces in the electron's g-factor ($g \approx 2.00232$):

$$\gamma_{\text{quantum}} = -g\frac{e}{2m_e} \qquad (2\text{-}6)$$

As a spin-half fermion, electron's spin is quantized as

$$\boldsymbol{s} = \frac{\hbar}{2}\boldsymbol{\sigma} \qquad (2\text{-}7)$$

where $\hbar$ is the Planck's constant, and $\boldsymbol{\sigma}$ is a dimensionless "spin" (or "spinor"), with eigenvalues of ±1 corresponding to the so-called spin-up and spin-down electrons. Measuring the z-component of electron's magnetic dipole moment will then give the expectation values

$$\mu_z = -g\frac{e}{2m_e}\cdot \pm\frac{\hbar}{2} \equiv \pm\frac{g}{2}\mu_B \approx \pm\mu_B \qquad (2\text{-}8)$$

where μ_B is the Bohr magneton.

In macroscopic systems, $\boldsymbol{\mu}$ can also belong to a nanometer-scale magnetic grain in a material, in which a large number of electron spins are forced to orient along one direction to form a single domain, due to the strong internal interactions which will be discussed in detail later in Section 2.3. The grain can then be classically treated as an individual dipole using Eq.(2-3), since the behavior of all spins will be coherent. When the grain size goes larger, the single domain cannot hold on and nonuniform magnetic structures will emerge, such as domain walls and magnetic vortices (of course, these cannot be considered as a "grain" any more). In addition, if the material is excited by nonuniform magnetic fields, the dynamics will also be nonuniform. An effective tool to solve these problems is numerical calculation, which usually divides the system into many finite-elements. Each finite-element is set sufficiently small (but still *macroscopic* as compared to single electrons or atoms) so that the nonuniformity is negligible as if it was a single-domain grain, and then Eq.(2-3) can be directly applied. The behavior of the whole system can be obtained by solving all the finite-elements simultaneously.

There is a unique type of magnet that naturally allows the single-domain configuration for arbitrary sizes, as long as the shape belongs to the general group of *ellipsoid* [Gurevich1996]. These shapes include spheres, infinitely thin planes and infinitely thin cylinders. They are related to some very important magnetic samples such as nanoparticles, thin films, and nanowires. Eq.(2-3) can be used to describe their *coherent* dynamics, and it will be shown that even incoherent dynamics can be studied rather easily for these special shapes.

So far, this section has discussed a wide range of magnetic objects that obey the simple Eq.(2-3), but there is a fundamental question – are these classical and quantum mechanical treatments equivalent? According to Arrott in [Arrott2005], this question was answered by Rabi and Schwinger, quoted here as "the classical motion of an electron in a magnetic field can be taken over into quantum mechanics without change, provided that a quantum interpretation is given in terms of the two components of the spin". Therefore in the remainder of this thesis, the magnetic dynamics will be interpreted in a classical frame, but the quantum-mechanically determined γ_e will be used. It is then more convenient to use the magnetization $\boldsymbol{M}$ as the basic quantity, defined as the averaged magnetic moment in a sufficiently small volume V:

$$\boldsymbol{M} = \frac{\sum_V \boldsymbol{\mu}}{V} \qquad (2\text{-}9)$$

which is usually a continuous function of space and time, $\boldsymbol{M}(\boldsymbol{r},t)$. Eq.(2-3) is rewritten as

$$\frac{\partial \boldsymbol{M}}{\partial t} = -\gamma_0 \boldsymbol{M} \times \boldsymbol{H}_{\text{eff}} \qquad (2\text{-}10)$$

Here two notation changes are made. The negative-valued γ is replaced by $-\gamma_0$, where γ_0 is the absolute value of the gyromagnetic ratio. A subscript is added for the magnetic field; $\boldsymbol{H}_{\mathrm{eff}}$ is called the effective field, in order to describe the complicated magnetic interactions between the studied object (a grain or a finite-element) and its macroscopic environment, which will be discussed in detail in Section 2.3.

2.2. Magnetic damping: Landau-Lifshitz's form and Gilbert's form

In real materials, a magnetic sub-system will exchange energy with its nonmagnetic environment; without external pumping, the magnetization will finally stop at its equilibrium state. Therefore a dissipation term must be added to the equation of motion to bring the magnetization to equilibrium. According to Eq.(2-10), this can be realized by making $\boldsymbol{M} \parallel \boldsymbol{H}_{\mathrm{eff}}$, when there is no torque to be applied on the magnetization. Some phenomenological damping terms have been proposed, and the widely acknowledged versions are due to Landau and Lifshitz [LL1935], and Gilbert [Gilbert1955]. The Landau-Lifshitz (LL) equation is

$$\frac{\partial \boldsymbol{M}}{\partial t} = -\gamma_0 \boldsymbol{M} \times \boldsymbol{H}_{\text{eff}} - \frac{\gamma_0 \lambda}{M^2} \boldsymbol{M} \times (\boldsymbol{M} \times \boldsymbol{H}_{\text{eff}}) \qquad (2\text{-}11)$$

The Landau-Lifshitz-Gilbert (LLG) equation is

$$\frac{\partial \boldsymbol{M}}{\partial t} = -\gamma_0 \boldsymbol{M} \times \boldsymbol{H}_{\text{eff}} + \frac{\alpha}{M} \boldsymbol{M} \times \frac{\partial \boldsymbol{M}}{\partial t} \qquad (2\text{-}12)$$

The damping parameters are λ (with dimensionality of *M*) and α (dimensionless), respectively. These two equations is formally equivalent by making the substitutions

$$\begin{aligned} \gamma_0 &\rightarrow \frac{\gamma_0}{1+\alpha^2} \approx \gamma_0 \\ \lambda &\rightarrow \frac{\alpha M}{1+\alpha^2} \approx \alpha M \end{aligned} \qquad (2\text{-}13)$$

The approximation signs are valid since most known materials have very small damping, in general $\alpha < 0.01$. The physical interpretations of these two mechanisms are also similar. The added damping torques in Eq.(2-11,2-12) are perpendicular to $\boldsymbol{M}$ and pointing to the vector of $\boldsymbol{H}_{\text{eff}}$, so both of them can pull the $\boldsymbol{M}$ vector towards $\boldsymbol{H}_{\text{eff}}$ (the equilibrium orientation) through a damping precession.

Another important property of the two damping torques is that they will not change the length of the $\boldsymbol{M}$ vector, ensured by the cross products in Eq.(2-11,2-12). This is consistent with most observations that the magnetization within a small single domain is constant, usually referred to as the saturation magnetization M_s

(the temperature is usually required to be well below T_c, the Curie temperature of specific materials). The conservation of M_s is very useful in research, as it reduces the degree of freedom from three to two and can simplify various problems. A good example is that magnetization dynamics can be investigated in spherical coordinates system using the polar and azimuthal angles (θ, φ):

$$\boldsymbol{M}(\boldsymbol{r},t)=\begin{pmatrix} M_x(t) \\ M_y(t) \\ M_z(t) \end{pmatrix}=M_s\begin{pmatrix} \sin\theta\cos\varphi \\ \sin\theta\sin\varphi \\ \cos\varphi \end{pmatrix} \qquad (2\text{-}14)$$

Some theoretical and computational applications benefiting from this approach will be presented in the following sections.

2.3. Interactions contributing to $\boldsymbol{H}_{\text{eff}}$

2.3.1. The magnetic energy density

The energy of a magnetic system is a summation of various physical mechanisms, and this energy can be treated as the point product of the local magnetic dipole moments and the effective field:

$$E=-\sum\nolimits_V \boldsymbol{\mu}\cdot\boldsymbol{H}_{\text{eff}} \qquad (2\text{-}15)$$

so the energy density is

$$\varepsilon \equiv \frac{E}{V} = -\boldsymbol{M} \cdot \boldsymbol{H}_{\text{eff}} \tag{2-16}$$

To calculate the effective field, one can assume an infinitesimal rotation of ***M***, and examine how the energy density is changed [Mansuripur1988]:

$$\delta\varepsilon = -\delta \boldsymbol{M} \cdot \boldsymbol{H}_{\text{eff}} \tag{2-17}$$

then the effective field can be expressed as

$$\boldsymbol{H}_{\text{eff}} = -\frac{\partial \varepsilon}{\partial \boldsymbol{M}} \tag{2-18}$$

In Cartesian coordinates system, Eq.(2-18) simply leads to

$$H_{\text{eff},i} = -\frac{\partial \varepsilon}{\partial M_i} \qquad (i = x, y, z) \tag{2-19}$$

In spherical coordinates system, however, the conservation of M_s provides the following way to express the components:

$$\begin{aligned} \delta\varepsilon &= -(H_r\hat{r} + H_\theta\hat{\theta} + H_\varphi\hat{\varphi}) \cdot (M_s\delta\theta\hat{\theta} + M_s \sin\theta\delta\varphi\hat{\varphi}) \\ &= -M_s H_\theta \delta\theta - M_s H_\varphi \sin\theta\delta\varphi \end{aligned} \tag{2-20}$$

so they are directly related to the derivatives of the energy density in terms of (θ, φ), which are usually convenient to derive.

$$\begin{aligned} H_\theta &= -\frac{1}{M_s}\frac{\partial \varepsilon}{\partial \theta} \\ H_\varphi &= -\frac{1}{M_s \sin\theta}\frac{\partial \varepsilon}{\partial \varphi} \end{aligned} \tag{2-21}$$

2.3.2. External energy

The energy associated to the applied bias field and the excitation pulse field has the simple form similar to Eq.(2-16), and the components of these fields can be directly added into $\boldsymbol{H}_{\mathrm{eff}}$. The bias field is known; the pulse field usually cannot be precisely measured in experiments, but can be calculated using the Biot-Savart law. Fortunately, the pulse strength does not need to be calculated exactly, since the scaling of spin dynamics with the pulse strength is almost linear in the small-amplitude regime.

2.3.3. Demagnetization energy

This contribution is caused by the magnetostatic interaction between magnetic dipole moments:

$$\varepsilon_d = \frac{1}{2}\sum_{i \neq j} \frac{3(\boldsymbol{\mu}_i \cdot \boldsymbol{r}_{ij})(\boldsymbol{\mu}_j \cdot \boldsymbol{r}_{ij}) - r_{ij}^{\;2}}{r_{ij}^{\;5}} \qquad \text{(2-22)}$$

where $\boldsymbol{r}_{ij}$ is the vector connecting any two dipole moments $\boldsymbol{\mu}_1$ and $\boldsymbol{\mu}_2$ in the system, and the 1/2 factor reflects the fact that the summation is double counted. The energy density is always positive, so the effective field due to this interaction, defined as

$$\boldsymbol{H}_d = -\frac{\partial \varepsilon_d}{\partial \boldsymbol{M}} \qquad (2\text{-}23)$$

is generally anti-parallel to the external field, thus is called "demagnetizing" field. In many cases, Eq.(2-23) can be written in the form of

$$\boldsymbol{H}_d = -\mathcal{N} \cdot \boldsymbol{M} \qquad (2\text{-}24)$$

where $\mathcal{N}$ is called the demagnetization tensor. For example, from Eq.(2-22) one can find the tensor between two dipole moments (with Cartesian coordinates),

$$\mathcal{N}_0 = -\frac{1}{r^2}\begin{pmatrix} 3x^2 - r^2 & 3xy & 3xz \\ 3xy & 3y^2 - r^2 & 3yz \\ 3xz & 3yz & 3z^2 - r^2 \end{pmatrix} \qquad (2\text{-}25)$$

For magnetic bodies with ellipsoidal shape, the demagnetization tensor has some good properties (for example, it will be diagonal). Fig.2-1 presents the results for several special cases. The geometry for a tangentally magnetized thin film is particularly useful for discussing the experimental results in later chapters. In this case, the demagnetizing field is simply [Gurevich1996, Miltat2002]

$$\boldsymbol{H}_d = -4\pi M_x \hat{\boldsymbol{x}} \qquad (2\text{-}26)$$

Clearly, this field is trying to pull back ("demagnetize") the magnetization into the film plane.

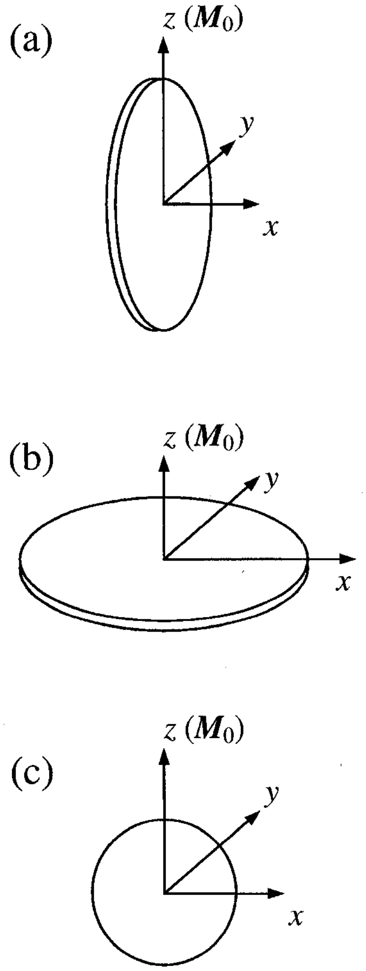

$$\begin{pmatrix} 4\pi & 0 & 0 \\ 0 & 0 & 0 \\ 0 & 0 & 0 \end{pmatrix}$$

$$\begin{pmatrix} 0 & 0 & 0 \\ 0 & 0 & 0 \\ 0 & 0 & 4\pi \end{pmatrix}$$

$$\begin{pmatrix} \frac{4\pi}{3} & 0 & 0 \\ 0 & \frac{4\pi}{3} & 0 \\ 0 & 0 & \frac{4\pi}{3} \end{pmatrix}$$

Fig. 2-1: Demagnetization tensors for selected ellipsoid geometries. (a), an infinite thin film with in-plane magnetization. (b), an infinite thin film with out-of-plane magnetization. (c), a

When the interested system has arbitrary shapes, numerical calculations are usually the only effective method for demagnetization problems. Then the demagnetization tensors for small rectangular cells (the finite elements used in the calculations) are particularly interesting. This problem has been solved with different methods [Nakatani1989, Newell1993, Hayashi1996, Fukushima1998]; a relatively new approach was also studied by the present author, and the results are summarized in the appendix of this Chapter.

2.3.4. Exchange energy

Exchange energy is related with the short-range interactions between neighboring magnetic atoms or molecules, mainly due to the Pauli principle modification of Coulomb interaction between neighboring electron spins. Unlike the long-range magnetostatic interactions which prefer anti-parallel configurations, exchange interactions tend to pull neighboring magnetic dipole moments towards the same direction. Exchange mechanisms are addressed using profound knowledge on quantum mechanics and chemistry, and will not be covered here. In common practice, the exchange energy density can be described by the following phenomenological equation:

$$\varepsilon_{exchange} = \frac{2A_x}{d^2}\left(1 - \frac{1}{M_s^2} M_1 \cdot M_2\right) \qquad (2\text{-}27)$$

where A_x is the exchange stiffness coefficient, and d is the distance between the two magnetization vectors $\boldsymbol{M}_1$ and $\boldsymbol{M}_2$ [Mansuripur1988]. The effective field can be similarly derived from the exchange energy density.

2.3.5. Anisotropy energy

Anisotropies are manifest as certain preferred configurations of the magnetization, arising from multiple physical origins such as anisotropic crystalline structures, magnetic memory, macroscopic shapes, different material properties at surfaces, etc. Mostly governed by quantum physics, many of these effects can still be described with phenomenological approaches and can be calculated classically [Mansuripur1995]. Since the material studied in this thesis, Permalloy, does not have notable anisotropies (one of the reasons it extensively appears in researches when people want to make the problem more concise), this term is neglected in the following chapters.

2.3.6. Thermal fluctuations

The magnetic dipole moments in a system are also subject to temperature-dependent interactions with the environment (primarily phonons). The resulting effect is that after a small amount of time Δt, each spin will be randomly pushed away from the projected final state uniquely determined by the LLG equation [Palacios1998]. This kind of thermal fluctuations are proved to behave as a Gaussian random process, and the associated effective field can be expressed as

$$\boldsymbol{H}_{\mathrm{th}} = \boldsymbol{G}\sqrt{\frac{2\alpha k_B T}{\gamma_0 M_s V \Delta t}} \qquad (2\text{-}28)$$

where k_B is the Boltzmann constant, and $\boldsymbol{G}$ is a vector whose components are within the range of (–1, 1] and are created by a Gaussian random number generator. In numerical calculations, Δt can just equal the time step because it is usually small enough.

2.4. Small-amplitude solutions of LLG equation; spin waves.

The experiments discussed in the following chapters will be using a rather weak magnetic pulse (~ 10 Oe) to drive the ferromagnetic specimens slightly out of equilibrium, so the resulting phenomena are mostly small-amplitude perturbations (spin waves), instead of those with large angle rotations (such as magnetic switching). This section will present some results that have provided support for those experimental projects.

2.4.1. Linearization of LLG equation

In general, magnetization dynamics can be investigated based on the concept of spin waves. Since magnetization $\boldsymbol{M}(\boldsymbol{r},t)$ and $\boldsymbol{H}(\boldsymbol{r},t)$ are continuous and smooth functions of space and time, they can always be written as the sums of their Fourier transform components:

$$\begin{aligned} \boldsymbol{M}(\boldsymbol{r},t) &= \sum_{\omega}\sum_{k} \boldsymbol{m}_{\omega,k} \exp(i\omega t - \boldsymbol{k}\cdot\boldsymbol{r}) \\ \boldsymbol{H}(\boldsymbol{r},t) &= \sum_{\omega}\sum_{k} \boldsymbol{h}_{\omega,k} \exp(i\omega t - \boldsymbol{k}\cdot\boldsymbol{r}) \end{aligned} \qquad (2\text{-}29)$$

Individual spin wave components are described by their frequency ω and wave vector $\boldsymbol{k}$, whose relation is determined by the dispersion law, $\omega(\boldsymbol{k})$. $\boldsymbol{m}_{\omega,k}$ and $\boldsymbol{h}_{\omega,k}$ are the Fourier coefficients of magnetization and magnetic field, respectively, and the summations are taken over all excited spin waves in the system.

When only small-amplitude *coherent* (i.e., $\boldsymbol{k} = 0$) spin waves are concerned, the Fourier space representations of spin waves and magnetic fields can be conventionally separated into their static part and alternating part:

$$\begin{aligned} \boldsymbol{M} &= \boldsymbol{M}_0 + \boldsymbol{m}\exp(i\omega t) \\ \boldsymbol{H}_{\text{eff}} &= \boldsymbol{H}_{\text{eff}\,0} + \boldsymbol{h}_{\text{eff}}\exp(i\omega t) \end{aligned} \qquad (2\text{-}30)$$

where $\boldsymbol{M}_0$ is the equilibrium state magnetization, and $M_0 = M_s$; $\boldsymbol{H}_{\text{eff}0}$ is the static effective field. The harmonic components $\boldsymbol{m}$ and $\boldsymbol{h}_{\text{eff}}$ are much smaller than the static counterparts: $m << M_s$, $h_{\text{eff}} << H_{\text{eff}0}$. Substitute $\boldsymbol{M}$ and $\boldsymbol{H}_{\text{eff}}$ into the LLG equation Eq.(2-12) and the linearized LLG equation is obtained [Gurevich1996]:

$$i\omega \boldsymbol{m} + \gamma_0 \boldsymbol{m} \times \boldsymbol{H}_{\text{eff}0} + \frac{i\alpha\omega}{M_s} \boldsymbol{m} \times \boldsymbol{M}_0 = -\gamma_0 \boldsymbol{M}_0 \times \boldsymbol{h}_{\text{eff}} \qquad (2\text{-}31)$$

Consider an isolated single-domain grain (equivalent to a dipole moment), where the effective field just consists of the applied bias field $\boldsymbol{H}_0$ and the excitation pulse field $\boldsymbol{h}$. This simple case is the basis for more complicated systems where the effects discussed in Section 2.3 have to be incorporated into the effective field. To investigate *eigenoscillations* the damping is also neglected for now. Suppose $\boldsymbol{H}_0$ and $\boldsymbol{M}_0$ are along the *z*-axis (see Fig.2-1(a) for reference), the Cartesian coordinates components of Eq.(2-37) are

$$\begin{aligned} & i\omega m_x + \gamma_0 H_0 m_y = \gamma_0 M_0 h_y \\ & -\gamma_0 H_0 m_x + i\omega m_y = -\gamma_0 M_0 h_x \\ & i\omega m_z = 0 \end{aligned} \qquad (2\text{-}32)$$

The solution can be written in a tensor form:

$$\boldsymbol{m} = \ddot{\chi}\boldsymbol{h} = \begin{pmatrix} \chi & i\chi_a & 0 \\ -i\chi_a & \chi & 0 \\ 0 & 0 & 0 \end{pmatrix} \boldsymbol{h} \qquad (2\text{-}33)$$

The tensor $\ddot{\chi}$ is called the high-frequency magnetic susceptibility, and the components are

$$\chi = \frac{\gamma_0 M_0 \omega_H}{\omega_H^2 - \omega^2}$$
$$\chi_a = \frac{\gamma_0 M_0 \omega}{\omega_H^2 - \omega^2} \qquad (2\text{-}34)$$

where $\omega_H \equiv \gamma_0 H_0$. From the denominators of Eq.(2-34) it is clear that ω_H is the resonance frequency (eigenfrequency) of this particular system.

Eq.(2-33) describes how the magnetic oscillations respond to an external ac field. Now substitute Eq.(2-33) into $\boldsymbol{b} = \boldsymbol{h} + 4\pi\boldsymbol{m}$ and one gets

$$\boldsymbol{b} = \breve{\mu}\boldsymbol{h} \qquad (2\text{-}35)$$

where $\breve{\mu}$ is called the high-frequency magnetic permeability, defined as

$$\breve{\mu} = 1 + 4\pi\breve{\chi} \qquad (2\text{-}36)$$

Eq.(2-35) tells how the magnetic induction behaves subject to an external pulse field. Therefore, $\breve{\chi}$ and $\breve{\mu}$ can completely describe the dynamics of a magnetic system [Gurevich1996, Cottam2005]; they will have more complicated forms under different conditions, but the basic linearization method presented above is quite general. For example, consider coherent oscillations in ellipsoid-shaped samples, where both the static and alternating parts of effective fields can be quantified using their demagnetizing tensor:

$$\boldsymbol{H}_{\text{eff}\,0} = \boldsymbol{H}_0 - \mathcal{N}\cdot\boldsymbol{M}_0$$
$$\boldsymbol{h}_{\text{eff}} = \boldsymbol{h} - \mathcal{N}\cdot\boldsymbol{m} \qquad (2\text{-}37)$$

Again, $\boldsymbol{H}_0$ and $\boldsymbol{h}$ are the *external* static field and the pulse field, respectively.

Eq.(2-31) can then be rewritten as

$$i\omega\boldsymbol{m}+\gamma_0\boldsymbol{m}\times\left(\boldsymbol{H}_0-\mathcal{N}\cdot\boldsymbol{M}_0\right)+\gamma_0\left(\mathcal{N}\cdot\boldsymbol{m}\right)\times\boldsymbol{M}_0+\frac{i\alpha\omega}{M_s}\boldsymbol{m}\times\boldsymbol{M}_0=-\gamma_0\boldsymbol{M}_0\times\boldsymbol{h} \quad (2\text{-}38)$$

The quantities in Eq.(2-38) are usually known (the applied bias field, the excitation pulse, and the demagnetizing factors for thin films, spheres etc.), thus it is very useful in solving magnetization dynamics in various geometries. Further details will be presented in Chapter 4.

2.4.2. General damping behavior of pulsed spin dynamics

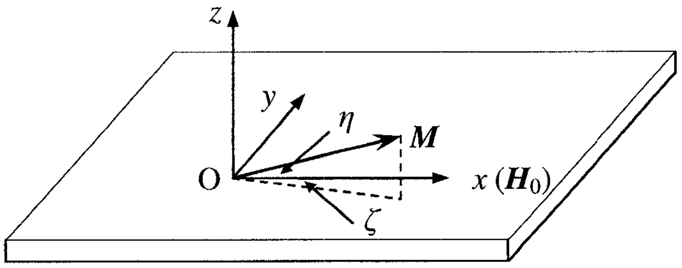

Fig. 2-2: The geometry for deriving Eq.(2-26) to Eq.(2-32). The *small* angles η and ζ have been exaggerated for clarity.

Spin dynamics in response to a short magnetic pulse is an extensively studied phenomenon, and many observations indicate that the damping oscillations generally follow an exponential profile. This can be easily deduced from the

LLG equation; here the spherical coordinates are used (see Eq.(2-14)) to rewrite the LLG equation as [Miltat2002]

$$\begin{cases} (1+\alpha^2)\dfrac{d\theta}{dt} = -\dfrac{\gamma_0}{\mu_0 M_s}\left(\alpha\dfrac{\partial w}{\partial\theta} + \dfrac{1}{\sin\theta}\dfrac{\partial w}{\partial\phi}\right) \\ (1+\alpha^2)\dfrac{d\phi}{dt} = \dfrac{\gamma_0}{\mu_0 M_s}\left(\dfrac{1}{\sin\theta}\dfrac{\partial w}{\partial\theta} - \dfrac{\alpha}{\sin^2\theta}\dfrac{\partial w}{\partial\phi}\right) \end{cases} \qquad (2\text{-}39)$$

The energy density functional can be very complicated for different conditions. A simple case is considered here, as shown in Fig.2-2, where an isotropic thin film is magnetized in-plane along *x*-direction by a bias field H_0, and all spins oscillate coherently (exchange interaction can be neglected). The energy density functional is then

$$w = -\mu_0 M_s H_0 \sin\theta\cos\phi + (\mu_0 M_s{}^2 \cos^2\theta)/2 \qquad (2\text{-}40)$$

The first term is the Zeeman energy provided by the bias field, and the second term is the demagnetization energy. Since the equilibrium orientation is $(90^\circ, 0^\circ)$, the following transformations are needed:

$$\begin{aligned} \theta &= 90^\circ + \eta \\ \phi &= 0^\circ + \zeta \end{aligned} \qquad (2\text{-}41)$$

so that (η, ζ) correspond to small-angle perturbations, and the following approximations can be made:

$$\begin{cases} \sin\theta = \cos\eta = 1 - \frac{1}{2}\eta^2 + \cdots \approx 1 \\ \cos\theta = -\sin\eta = -\eta + \frac{1}{6}\eta^3 - \cdots \approx -\eta \\ \sin\phi = \sin\zeta = \zeta - \frac{1}{6}\zeta^3 + \cdots \approx \zeta \\ \cos\phi = \cos\zeta = 1 - \frac{1}{2}\zeta^2 + \cdots \approx 1 \end{cases} \tag{2-42}$$

Using these approximations, Eq.(2-25) is differentiated as

$$\begin{cases} \frac{\partial w}{\partial\theta} = -\mu_0 M_s H_0 \cos\theta\cos\phi - \mu_0 M_s^{\,2} \cos\theta\sin\theta \approx \mu_0 M_s (H_0 + M_s)\eta \\ \frac{\partial w}{\partial\phi} = \mu_0 M_s H_0 \sin\theta\sin\phi \approx \mu_0 M_s H_0 \zeta \end{cases} \tag{2-43}$$

Inputting Eq.(2-28) into Eq.(2-24) leads to the equation of motion for (η, ζ):

$$\begin{cases} \frac{1+\alpha^2}{\gamma_0}\frac{d\eta}{dt} = -\alpha(H_0 + M_s)\eta - H_0\zeta \\ \frac{1+\alpha^2}{\gamma_0}\frac{d\zeta}{dt} = (H_0 + M_s)\eta - \alpha H_0\zeta \end{cases} \tag{2-44}$$

Therefore this is also a linearization approach for the LLG equation. According to standard theories of first-order differential equations, the solutions can be found by the characteristic equation:

$$\begin{vmatrix} -\alpha(H_0 + M_s) - p & -H_0 \\ H_0 + M_s & -\alpha H_0 - p \end{vmatrix} = 0 \tag{2-45}$$

where p is the eigenvalue. The solutions of p are conjugate complex numbers

$$p = -\frac{\alpha(2H_0 + M_s)}{2} \pm i\frac{1}{2}\sqrt{4(1+\alpha^2)H_0(H_0 + M_s) - \alpha^2(2H_0 + M_s)^2} \tag{2-46}$$

The real part of p corresponds to a damping term and the imaginary part corresponds to a sinusoidal terms; so the spin dynamics in terms of the off-equilibrium components will have the general form of

$$\eta, \zeta \propto e^{-t/\tau} \sin(\omega t + \psi_0) \qquad \text{(2-47)}$$

where τ is the exponential decay time, which is directly related to Gilbert's damping constant:

$$\tau = \frac{2}{\alpha \gamma_0 (2H_0 + M_s)} \qquad \text{(2-48)}$$

The phase parameter ψ_0 can be set to zero if one assumes the dynamics immediately follows the rise of the excitation pulse.

The eigenfrequency ω has the simple form after neglecting the α^2 terms,

$$\omega = \sqrt{H_0 (H_0 + M_s)} \qquad \text{(2-49)}$$

which is the Kittel's famous formula for this geometry. With the spherical coordinates approach, the eigenfrequency can also be determined by the Smit-Suhl formula [Gurevich1996]:

$$\omega = \frac{\gamma_0}{M_s \sin\theta_0} \sqrt{\frac{\partial^2 w}{\partial \theta^2} \frac{\partial^2 w}{\partial \varphi^2} - \left(\frac{\partial^2 w}{\partial \theta \partial \varphi} \right)^2} \qquad \text{(2-50)}$$

where θ_0 is the polar angle of the equilibrium orientation.

Although the solutions in Eq.(2-32) are derived for the simple geometry shown in Fig.2-2, the *exponential* damping behavior is a general result, as can be seen from Eq.(2-29). No matter how complicated the system's Hamiltonian is, the energy density functional w will end up with a Taylor's expansion in terms of the angles η and ζ. In the small-angle regime, the terms with power of two or higher (η^2, ζ^2, $\eta\zeta$ etc.) can always be neglected and the differential equations in Eq.(2-29) will remain first-order. The exponentially damping sinusoid in Eq.(2-32) will always be the general solutions of such equations.

2.4.3. Magnetostatic limit

This section begins to consider incoherent spin waves, i.e. $\boldsymbol{k} \neq 0$. Fig.2-3 shows a categorization according to k [DeWames1970]. This thesis focuses on the magnetostatic spin waves because the size of excitation devices to be introduced in the later experimental chapters are on the μm scales, which means the majority of the excited spin waves fall into the magnetostatic region.

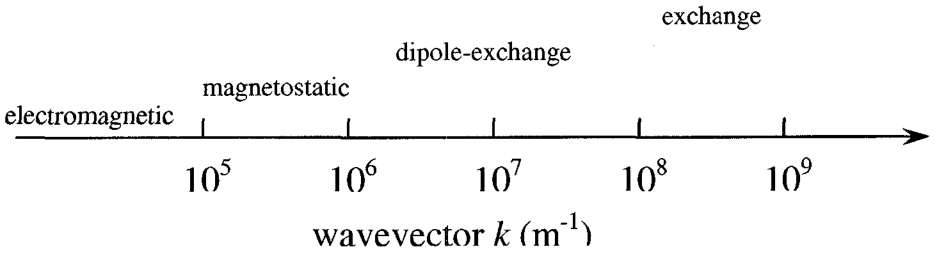

Fig.2-3: Typical spin waves with different ranges of wavevectors.

We start from the Maxwell equations:

$$\begin{aligned}
&\nabla\times\boldsymbol{E}+\frac{1}{c}\frac{\partial\boldsymbol{B}}{\partial t}=0\\
&\nabla\cdot\boldsymbol{B}=0\\
&\nabla\times\boldsymbol{H}-\frac{1}{c}\frac{\partial\boldsymbol{D}}{\partial t}=\frac{4\pi}{c}\boldsymbol{J}\\
&\nabla\cdot\boldsymbol{D}=4\pi\rho
\end{aligned}\tag{2-51}$$

where $\boldsymbol{D}=\boldsymbol{E}+4\pi\boldsymbol{P}$, $\boldsymbol{H}=\boldsymbol{B}-4\pi\boldsymbol{M}$. These quantities can also be divided into their static and alternating components (complex amplitudes), and one can easily derive the equations for electrostatics and magnetostatics:

$$\begin{aligned}
&\nabla\times\boldsymbol{H}_0=\frac{4\pi}{c}\boldsymbol{J}_0\\
&\nabla\cdot\boldsymbol{B}_0=0
\end{aligned}\tag{2-52}$$

and those for small-amplitude electromagnetic waves:

$$\begin{aligned}&\nabla\times\boldsymbol{e}+\frac{i\omega}{c}\boldsymbol{b}=0\\&\nabla\cdot\boldsymbol{b}=0\\&\nabla\times\boldsymbol{h}-\frac{i\omega}{c}\boldsymbol{d}=\frac{4\pi}{c}\boldsymbol{j}\\&\nabla\cdot\boldsymbol{d}=4\pi\rho\end{aligned}\qquad(2\text{-}53)$$

It is the third equation in Eq.(2-5-3) that is useful here to establish the so-called magnetostatic limit; for the magnetic systems considered in this thesis, the spin waves are too slow as compared with light, and there is no current, so we simply have

$$\nabla\times\boldsymbol{h}=0\qquad(2\text{-}54)$$

Therefore, the magnetostatic potential can be introduced to reduce the vector problem into a scalar one:

$$\boldsymbol{h}=\nabla\psi\qquad(2\text{-}55)$$

The divergence equation of $\boldsymbol{b}$ in Eq.(2-53) can be rewritten as (also recall Eq.(2-35)) [Gurevich1996]

$$\nabla\cdot(\boldsymbol{h}+4\pi\boldsymbol{m})\equiv\nabla\cdot(\vec{\mu}\boldsymbol{h})=\nabla\cdot(\vec{\mu}\nabla\psi)=0\qquad(2\text{-}56)$$

which is named after Walker [Walker1957], one of the pioneers in exploring the field. Clearly, in free space the Walker's equation reduces to the Laplace equation:

$$\nabla^2\psi=0\qquad(2\text{-}57)$$

At the interfaces between two media, the boundary conditions for the magnetostatic potential ψ can be deduced from the Maxwell equations regarding the continuity of ***h*** and ***b*** fields. Suppose the interface is in y-z plane and x-axis is the normal, these boundary conditions are [Gurevich1996]:

$$\begin{aligned} \frac{\partial\psi_1}{\partial y} &= \frac{\partial\psi_2}{\partial y} \\ \frac{\partial\psi_1}{\partial z} &= \frac{\partial\psi_2}{\partial z} \\ (\ddot{\mu}_1\nabla\psi_1)_x &= (\ddot{\mu}_2\nabla\psi_2)_x \end{aligned} \qquad (2\text{-}58)$$

2.4.4. Magnetostatic spin waves

Magnetostatic spin waves, in terms of ψ, can be generally expressed as

$$\psi = \psi_0 \exp\left(-ik_x x - ik_y y - ik_z z\right) \qquad (2\text{-}59)$$

where ψ_0 is a constant. When the permeability tensor for a specific problem is deduced, one can substitute Eq.(2-59) into Eq.(2-56) and Eq.(2-57), then use the boundary conditions Eq.(2-58) to find the dispersion law of the spin waves of interest. The studies on this subject have been intensive through 1950's to 1970's by many authors, such as Kittel, Walker, Damon and Eshbach, Wolfram etc. [Kittel1948, Walker1957, DE1961, DeWames1970]. Their methods were somewhat different, some were approximated, but mostly were consistent with each other. Here we jump to the typical results for two special cases – an infinitely large, tangentally magnetized thin film, with wave vectors parallel or perpendicular to the saturated magnetization [Gurevich1996, Cottam2005]. These two cases will be experimentally studied in Chapter 4.

When $\boldsymbol{k} \perp \boldsymbol{M}_0$ (i.e., $k = k_y$ and $k_z = 0$, since it is assumed that $\boldsymbol{M}_0$ is on the z-axis), it has been shown that the wave vector along the film thickness (k_x) will be imaginary: $k_x = \pm i k_y$. The spin waves are then localized near the surface and are exponentially decaying along the film thickness. Therefore they are called magnetostatic surface spin waves (MSSW). Their dispersion law is:

$$\omega = \left[\left(\omega_H + \frac{\omega_M}{2} \right)^2 - \left(\frac{\omega_M}{2} \right)^2 \exp(-2kd) \right]^{1/2} \qquad (2\text{-}60)$$

where $\omega_H = \gamma_0 H_0$, $\omega_M = 4\pi \gamma_0 M_0$, and d is the film thickness. The group velocity, defined as $v_g \equiv d\omega/dk$, is

$$v_g = \frac{d\omega_M^2}{4\omega} \exp(-2kd) \qquad (2\text{-}61)$$

When $\boldsymbol{k} \,//\, \boldsymbol{M}_0$, the excited spin waves belong to *volume* waves, with the dispersion law [Bailleul2001]:

$$\omega = \left[\omega_H{}^2 + \omega_H \omega_M \frac{1 - \exp(-kd)}{kd} \right]^{1/2} \qquad (2\text{-}62)$$

and the group velocity is

$$v_g = \omega_H \omega_M \frac{(kd+1)\exp(-kd)-1}{2\omega k^2 d} \tag{2-63}$$

When $kd \ll 1$ (thin film limit), the numerator in Eq.(2-63) can be approximated as $-(kd)^2/2$ and is negative, indicating that the waves propagate anti-parallel to the wave vector (and the phase velocity), so they are called magnetostatic *backward* volume waves (MSBVW). More details on the group velocities of MSSW and MSBVW will be discussed in Chapter 4.

2.5. Numerical approach – micromagnetic simulation

Micromagnetic simulation has been proven a very useful tool to study both the quasi-static behavior and ultrafast dynamics of magnetic systems. This is a highly participated-in research area, and a large variety of numerical methods have been established, such as finite-element methods, finite-variance methods, and Monte-Carlo methods. The studies discussed in this thesis adopt a standard finite-element approach, in which the magnetic specimen is divided into many sufficiently small rectangular cells, each of which obeys the LLG equation in the spherical coordinates form (Eq.(2-39)). The energy terms contributed to the effective field have been discussed in Section 2.3. The effective field calculations occupy the majority of the computation loads, especially for the demagnetization field which requires a fast Fourier transform (FFT) algorithm. Starting from an initial magnetization configuration, Eq.(2-39) is then solved step-by-step using a fifth-order, self-adaptive Runge-Kutta algorithm [Press1992], and the evolutions of θ and φ for all the cells can be revealed. The details of the calculations are included in the author's Master thesis [Liu2003].

2.6. A brief introduction to the magneto-optical Kerr effect

Magneto-optical effects were first discovered as early as 1845 by Faraday, who observed that the plane of polarization of a linearly polarized light was rotated after going through a medium in a magnetic field. If the light is reflected from the medium surface, similar polarization change also occurs, and is known as the magneto-optical Kerr effect (MOKE). These effects originate from the interactions between the intrinsic electron spins and the angular momentum of the orbiting electrons (spin-orbital coupling). In the presence of a magnetic field, these interactions will generate multiple spin-dependent energy levels in the system's Hamiltonian [Freiser1968]. Light emission from such a system will show Zeeman splitting: the majority of the light is polarized parallel to the magnetic field with unchanged frequency, while two small components are polarized perpendicular to the magnetic field with displaced frequencies; if more than three components are observed, the effect is usually referred to as the "anomalous" Zeeman splitting. As a macroscopic result, certain optical properties of the materials will also be changed by the magnetic field, such as the index of refraction and the coefficients for absorption and reflection, and the polarization rotations of an incident light are induced by these changes. The solutions of such problems certainly have involved a great deal of work in many decades, but the phenomenological description, which is the basis for most magneto-optical applications, is quite straightforward. If the complex amplitude of the incident polarized light is taken as unity, the reflected light will consist of two orthogonal parts: the Fresnel reflection component r and the Kerr component k. The effect can be specified by writing

$$\frac{k}{r} = \theta_K + i\varepsilon_K \tag{2-64}$$

where θ_K is called Kerr rotation and ε_K is called Kerr ellipticity (both are real quantities), and $|k/r| << 1$ for all materials.

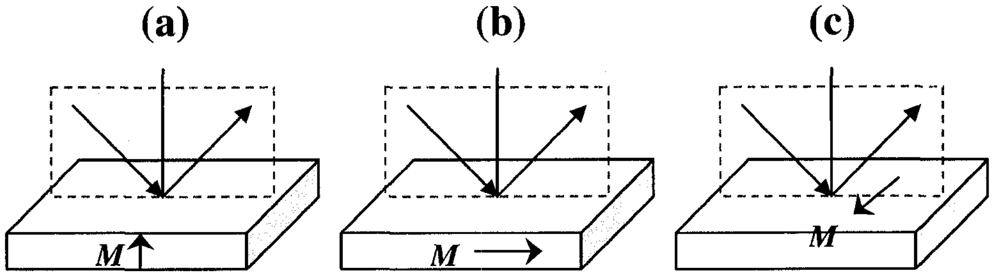

Fig.2-4: The three types of magneto-optical Kerr effect. (a), Polar. (b), Longitudinal. (c), Transverse. The dashed rectangles stand for the plane of incidence.

There are three types of MOKE's according to the geometry, as illustrated in Fig.2-4 [Freiser1968]. If the magnetization is parallel to the plane of incidence and is perpendicular to the sample surface, it is called the polar Kerr effect (Fig.2-4(a)); if the magnetization is parallel both to the plane of incidence and to the surface, it is called the longitudinal Kerr effect (Fig.2-4(b)); if the magnetization is perpendicular to the plane of incidence (and therefore is necessarily parallel to the surface), it is called the transverse or equatorial Kerr effect (Fig.2-4(c)).

Now consider *normal* incidence of a linearly polarized light for the case of polar Kerr effect, which is the geometry adopted in many experiments including those to be discussed in this thesis. Linear polarization means that the light can be decomposed into two circularly polarized lights with equal amplitude and opposite helicities. Due to the Zeeman effect, the indices of refraction of these two components are different, denoted as $n_+(\omega)$ and $n_-(\omega)$, where ω is the frequency of the light. In this geometry, the reflected amplitudes (Fresnel coefficient) can be expressed as

$$r_\pm = -\frac{n_\pm - 1}{n_\pm + 1} = |r_\pm| \exp(i\phi_\pm) \tag{2-65}$$

where $\phi_\pm$ are the phase angles. When these two reflected components are combined together, the result will be an elliptically (no longer linearly) polarized light. It can be shown that to the first order of $n_+ - n_-$, the Kerr rotation is

$$\theta_K = -\frac{1}{2}(\phi_+ - \phi_-) \approx -\mathrm{Im}\frac{n_+ - n_-}{n_+ n_- - 1} \tag{2-66}$$

The Kerr ellipticity is then

$$\varepsilon_K \approx -\mathrm{Re}\frac{n_+ - n_-}{n_+ n_- - 1} \tag{2-67}$$

Now the important question is how the magnetic field is related to the polar Kerr effect described by Eq.(2-66,2-67). When a magnetic field is present, the index of refraction will change from n to n', and can be generally written, to the first order, as

$$n'(\omega) = n(\omega) + \frac{dn}{d\omega}\Delta\omega \qquad (2\text{-}68)$$

where $\Delta\omega$ is the small frequency shift (perturbation) as a result of turning on the magnetic field. In classical physics, this kind of induced oscillation is nothing but the Larmor precession driven by the Lorentz force, and $\Delta\omega$ is just the Larmor frequency:

$$\omega_L = \frac{e}{2m_e}H \qquad (2\text{-}69)$$

This simple model can be generalized and is called Larmor's theorem, which says that the properties of a system of electrons in a magnetic field are the same as the zero-field case but are observed from a frame that rotates about the field direction with the Larmor frequency. Concerning the indices of refraction of the circularly polarized lights, Eq.(2-68) will give

$$n_+(\omega) - n_-(\omega) = 2\omega_L \frac{dn}{d\omega} \qquad (2\text{-}70)$$

Combining Eq.(2-69, 2-70) with Eq.(2-66, 2-67) it is clear that Kerr rotation and Kerr ellipticity are indeed proportional to the magnetic field (or the magnetization of the sample itself). The quantum mechanical version of the theory is much more complicated but yields a similar result, that Kerr rotation and Kerr ellipticity are proportional to the expectation value of the average spin components along the surface normal (M_z). Thus the out-of-plane magnetization near the sample surface can be measured through the polar Kerr effect.

Appendix of Chapter 2

Volume-average magnetostatic interaction between single domain magnets with arbitrary shapes

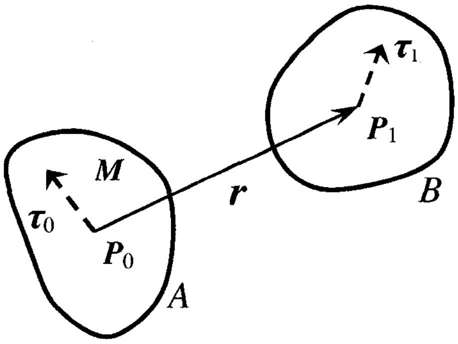

Fig. 2-5: Two objects, *A* and *B*, with arbitrary shapes. *A* is uniformly magnetized with magnetization ***M***.

Assume two objects, *A* and *B*, are labeled by a reference point inside each of them, $\boldsymbol{P}_0$ and $\boldsymbol{P}_1$. For simplicity, $\boldsymbol{P}_0$ is set as the origin of the coordinates system, and $\boldsymbol{P}_1$ is now located at $\boldsymbol{r}$, as illustrated in Fig.2-5. If *A* is uniformly magnetized with magnetization $\boldsymbol{M}$, the average magnetic vector potential that is applied on *B* can be written as [Brown1962, Jackson1975]

$$\langle A \rangle(\boldsymbol{r}) = \frac{1}{V_1} \int_{V_1} d^3\boldsymbol{\tau}_1 \int_{V_0} d^3\boldsymbol{\tau}_0 \boldsymbol{M} \times \frac{\boldsymbol{r}+\boldsymbol{\tau}_1-\boldsymbol{\tau}_0}{|\boldsymbol{r}+\boldsymbol{\tau}_1-\boldsymbol{\tau}_0|^3} \tag{A2-1}$$

where $\boldsymbol{\tau}_0$ and $\boldsymbol{\tau}_1$ are arbitrary points inside *A* and *B*, V_0 and V_1 are the volumes of *A* and B, respectively. The shape functions, $D_0(\boldsymbol{\tau}_0)$ and $D_1(\boldsymbol{\tau}_1)$, are used to describe the spatial confinements of the two objects. They are generally defined as

$$D(\boldsymbol{\tau}) \equiv \begin{cases} 1, \text{ if a point } \boldsymbol{\tau} \text{ is inside the object} \\ 0, \text{ otherwise} \end{cases} \tag{A2-2}$$

Now the integrals in Eq.A2-1 can be extended to the whole space, and the following deductions can be made using the properties of convolution and cross-correlation:

$$\begin{aligned} \langle \boldsymbol{A} \rangle(\boldsymbol{r}) &= \frac{1}{V_1} \int_\infty d^3\boldsymbol{\tau}_1 D_1(\boldsymbol{\tau}_1) \int_\infty d^3\boldsymbol{\tau}_0 D_0(\boldsymbol{\tau}_0) \boldsymbol{M} \times \frac{\boldsymbol{r} + \boldsymbol{\tau}_1 - \boldsymbol{\tau}_0}{|\boldsymbol{r} + \boldsymbol{\tau}_1 - \boldsymbol{\tau}_0|^3} \\ &= \frac{1}{V_1} \int_\infty d^3\boldsymbol{\tau}_1 D_1(\boldsymbol{\tau}_1) [D_0(\boldsymbol{r} + \boldsymbol{\tau}_1) \otimes (\boldsymbol{M} \times \frac{\boldsymbol{r} + \boldsymbol{\tau}_1}{|\boldsymbol{r} + \boldsymbol{\tau}_1|^3})] \\ &= \frac{1}{V_1} D_1(-\boldsymbol{r}) \otimes D_0(\boldsymbol{r}) \otimes (\boldsymbol{M} \times \frac{\boldsymbol{r}}{r^3}) \\ &\equiv V_0 S(\boldsymbol{r}) \otimes (\boldsymbol{M} \times \frac{\boldsymbol{r}}{r^3}) \end{aligned} \tag{A2-3}$$

where $\otimes$ is the convolution operator, and a shape factor for a two-body system is introduced, which plays a key role in this model:

$$S(\boldsymbol{r}) \equiv \frac{1}{V_0 V_1} D_1(-\boldsymbol{r}) \otimes D_0(\boldsymbol{r}) \tag{A2-4}$$

To compute the magnetic flux density, we start from

$$\boldsymbol{B}(\boldsymbol{r}) = \nabla \times \boldsymbol{A}(\boldsymbol{r}) \tag{A2-5}$$

Recall the macroscopic version of Maxwell's equations, and follow the discussion in Ref.[Newell1993], we shall have the same relation after averaging over the source and observing objects, provided that sizes of the objects are much larger than atomic spacing while small enough to build a smooth field:

$$\langle \boldsymbol{B} \rangle(\boldsymbol{r}) = \nabla \times \langle \boldsymbol{A} \rangle(\boldsymbol{r}) \qquad \text{(A2-6)}$$

Plug (A2-3) into (A2-6), and use the derivation rule of convolution, we have

$$\begin{aligned} \langle \boldsymbol{B} \rangle(\boldsymbol{r}) &= V_0 S(\boldsymbol{r}) \otimes (\nabla \times \boldsymbol{M} \times \frac{\boldsymbol{r}}{r^3}) \\ &= V_0 S(\boldsymbol{r}) \otimes (\nabla \cdot \frac{\boldsymbol{r}}{r^3}) \boldsymbol{M} - V_0 S(\boldsymbol{r}) \otimes (\boldsymbol{M} \cdot \nabla) \frac{\boldsymbol{r}}{r^3} \end{aligned} \qquad \text{(A2-7)}$$

In the second line of (A2-7), the first term can be easily shown to be $4\pi\boldsymbol{M}(\boldsymbol{r})$. The second term is then the average demagnetizing field, which has the following form after some vector algebra:

$$\langle \boldsymbol{H} \rangle(\boldsymbol{r}) = -S(\boldsymbol{r}) \otimes \mathcal{N}_0(\boldsymbol{r}) \cdot \boldsymbol{M} \qquad \text{(A2-8)}$$

where $\mathcal{N}_0(\boldsymbol{r})$ is the dipolar demagnetizing tensor introduced in Eq.(2-25). Compare Eq.(A2-8) with Eq.(2-24), the volume-averaged demagnetizing tensor is simply given by

$$\mathcal{N}(\boldsymbol{r}) = S(\boldsymbol{r}) \otimes \mathcal{N}_0(\boldsymbol{r}) \qquad \text{(A2-9)}$$

The physical significance of above relations is that the volume-averaged interaction differs from the ideal dipolar interaction only by a convolution with the shape factor, $S(\boldsymbol{r})$, which reflects the intrinsic geometric property of a two-body system.

Now focus on a special case of above model, namely the two objects are rectangular cells (cuboids) with same dimensions a, b, c in the x, y and z directions, respectively. The shape function is simply a 3D rectangle function:

$$D(\boldsymbol{r}) = \Pi(\frac{x}{a})\Pi(\frac{y}{b})\Pi(\frac{z}{c}) \tag{A2-10}$$

with $\Pi(x) = 1$ if $-1/2 \le x \le 1/2$ and 0 otherwise. It is easy to show from Eq.(A2-4) that the shape factor is a modified 3D triangle function:

$$S(\boldsymbol{r}) = \frac{1}{(abc)^2}\Lambda(x,a)\Lambda(y,b)\Lambda(z,c) \tag{A2-11}$$

with

$$\Lambda(x,a) = \begin{cases} x+a, \text{ if } -a \le x < 0 \\ -x+a, \text{ if } 0 \le x \le a \\ 0, \text{ otherwise} \end{cases} \tag{A2-12}$$

The elements of $\mathcal{N}$ can be analytically computed. Take $\mathcal{N}_{xx}$ as an example:

$$\begin{aligned} \mathcal{N}_{xx}(x,y,z) = -\frac{1}{abc}\int_{-a}^{a}dx'\int_{-b}^{b}dy'\int_{-c}^{c}dz'\Lambda(x',a)\Lambda(y',b)\Lambda(z',c) \\ \cdot\frac{2(x-x')^2-(y-y')^2-(z-z')^2}{[(x-x')^2+(y-y')^2+(z-z')^2]^{5/2}} \end{aligned} \tag{A2-13}$$

Because the 3D triangle function is piecewise linear in each octant in the Cartesian coordinates, it is convenient to split Eq.(A2-13) into eight terms. Changes of variables and integration limits can be performed to write the integrals in a unified form:

$$\mathcal{N}_{xx}(x,y,z) = -\frac{1}{abc}\sum_{i=1}^{2}\sum_{j=1}^{2}\sum_{k=1}^{2} F_{xx}[|x+(-1)^i a|,|x|,|y+(-1)^j b|,|y|,|z+(-1)^k c|,|z|] \tag{A2-14}$$

where

$$F_{xx}(x_0,x_1,y_0,y_1,z_0,z_1) = \int_{x_0}^{x_1}dx\int_{y_0}^{y_1}dy\int_{z_0}^{z_1}dz\frac{(x-x_0)(y-y_0)(z-z_0)(2x^2-y^2-z^2)}{(x^2+y^2+z^2)^{5/2}} \tag{A2-15}$$

Note all input variables of F_{xx} are non-negative. According to the first fundamental theorem of calculus, multi-fold definite integrals can be evaluated via their indefinite counterparts. A relevant discussion on this topic can be found in Ref.[Fukushima1998], and the result is:

$$\begin{aligned} F_{xx}(x_0,x_1,y_0,y_1,z_0,z_1) = \\ & -G_{xx}(x_0,y_0,z_0)+G_{xx}(x_1,y_0,z_0) \\ & +G_{xx}(x_0,y_1,z_0)+G_{xx}(x_0,y_0,z_1) \\ & -G_{xx}(x_1,y_1,z_0)-G_{xx}(x_1,y_0,z_1) \\ & -G_{xx}(x_0,y_1,z_1)+G_{xx}(x_1,y_1,z_1) \end{aligned} \tag{A2-16}$$

where G_{xx} is an indefinite integral:

$$\int dz\int dy\int dx\frac{(x-x_0)(y-y_0)(z-z_0)(2x^2-y^2-z^2)}{(x^2+y^2+z^2)^{5/2}} \tag{A2-17}$$

where x_0, y_0 and z_0 are the same input variables of F_{xx}. The integration result contains lengthy terms, but some of them will be cancelled out when evaluating Eq.(A2-16). By omitting such terms, we finally find

$$\begin{aligned} G_{xx}(x,y,z) &= (y_0 z/2)(z-2z_0)\ln(y+r) \\ &\quad -(z_0/2)(x^2-2x_0x-y^2+2y_0y)\ln(z+r) \\ &\quad -(y_0x/4)(x-2x_0)\ln[(x^2+y^2+yr)^2+x^2z^2] \\ &\quad -x_0y_0z_0\arctan[xz/(x^2+y^2+yr)] \\ &\quad +(r/6)(4x^2-6x_0x-2y^2+3y_0y-2z^2+3z_0z) \end{aligned} \tag{A2-18}$$

where $r = (x^2 + y^2 + z^2)^{1/2}$. From Eq.(A2-14) and Eq.(A2-16) one can see that either $x = x_0$, or $y = y_0$, or $z = z_0$ will hold for every G_{xx}. Therefore, no divergence will occur at the odd point $x = y = z = 0$, ensuring this formula for to be complete.

Now turn to the off-diagonal element, $\mathcal{N}_{xy}(\boldsymbol{r})$:

$$\begin{aligned} \mathcal{N}_{xy}(x,y,z) &= -\frac{1}{abc}\int_{-a}^{a}dx'\int_{-b}^{b}dy'\int_{-c}^{c}dz'\Lambda(x',a)\Lambda(y',b)\Lambda(z',c) \\ &\quad \cdot\frac{3(x-x')(y-y')}{[(x-x')^2+(y-y')^2+(z-z')^2]^{5/2}} \end{aligned} \tag{A2-19}$$

It can be calculated in the same way as $\mathcal{N}_{xx}$, but the result looks a little more complicated due to the anti-symmetry in terms of $(x-x')$ and $(y-y')$:

$$\begin{aligned} \mathcal{N}_{xy}(x,y,z) &= -\frac{1}{abc}\sum_{i=1}^{2}\sum_{j=1}^{2}\sum_{k=1}^{2}\{\operatorname{sgn}[x+(-1)^i a]\cdot\operatorname{sgn}[y+(-1)^j b] \\ &\quad \cdot F_{xy}[|x+(-1)^i a|,|x|,|y+(-1)^j b|,|y|,|z+(-1)^k c|,|z|]\} \end{aligned} \tag{A2-20}$$

where $\operatorname{sgn}(x) = +1$ for $x \geq 0$ and -1 for $x < 0$, and

$$
\begin{aligned}
F_{xy}(x_0, x_1, y_0, y_1, z_0, z_1) = \\
&-G_{xy}(x_0, y_0, z_0) + G_{xy}(x_1, y_0, z_0) \\
&+G_{xy}(x_0, y_1, z_0) + G_{xy}(x_0, y_0, z_1) \\
&-G_{xy}(x_1, y_1, z_0) - G_{xy}(x_1, y_0, z_1) \\
&-G_{xy}(x_0, y_1, z_1) + G_{xy}(x_1, y_1, z_1)
\end{aligned}
\tag{A2-21}
$$

with

$$
\begin{aligned}
G_{xy}(x, y, z) = &-(z_0 y/2)(y - 2y_0)\arctan(xz/yr) \\
&+(z^2/6)(2z - 3z_0)\arctan[-yz/(x^2 + z^2 + xr)^2] \\
&-(z_0 x/2)(x - 2x_0)\arctan[xy/(x^2 + z^2 + zr)^2] \\
&-(y^2/6)(2y - 3y_0)\ln(x + r) \\
&-(1/6)(2x^3 - 3x_0 x^2 - 3x_0 z^2 + 6x_0 z_0 z)\ln(y + r) \\
&+(y_0 z/4)(z - 2z_0)\ln[(x^2 + z^2 + xr)^2 + y^2 z^2] \\
&-(x_0 y_0 z_0/2)\ln[(x^2 + z^2 + zr)^2 + x^2 y^2] \\
&+(r/6)(6x_0 y_0 - 3y_0 x - 3x_0 y + 2xy)
\end{aligned}
\tag{A2-22}
$$

Again, x_0, y_0 and z_0 are just the same input variables of F_{xy}, and no divergence will occur at the point $x = y = z = 0$.

Since $\mathcal{N}_{xx}$ and $\mathcal{N}_{xy}$ have been found, other elements of $\mathcal{N}(\boldsymbol{r})$ can be obtained simply by commutations of variables [Newell1993, Fukushima1998].

An obvious feature of the model, as shown from Eq.(A2-3) to Eq.(A2-9), is the intensive involvement of real-space convolutions. This inspires us to map the problem into the Fourier space [Mansuripur1995, Beleggia2003a, Belleggia2003b, Tandon2004, Beleggia2004], where convolutions become direct products. First, the Fourier transform (FT) of the shape factor is given by

$$S(\boldsymbol{k}) \equiv \mathrm{FT}[S(\boldsymbol{r})] = \frac{1}{V_0 V_1} D_0(\boldsymbol{k}) D_1(-\boldsymbol{k}) \tag{A2-23}$$

Eq.(A2-3) can also be transformed into Fourier space:

$$\langle \boldsymbol{A} \rangle(\boldsymbol{k}) = V_0 S(\boldsymbol{k}) \boldsymbol{M} \times (-4\pi i \frac{\boldsymbol{k}}{k^2}) \tag{A2-24}$$

where the following FT identity is used [Mansuripur1995]:

$$\mathrm{FT}(\frac{\boldsymbol{r}}{r^3}) = -4\pi i \frac{\boldsymbol{k}}{k^2} \tag{A2-25}$$

In Fourier space, the nabla operator is transformed as ***ik*** [Beleggia2003a], so the FT of magnetic induction is

$$\begin{aligned} B(k) &= i\boldsymbol{k} \times [V_0 S(\boldsymbol{k}) \boldsymbol{M} \times (-4\pi i \frac{\boldsymbol{k}}{k^2})] \\ &= 4\pi V_0 S(\boldsymbol{k}) [\boldsymbol{M} - \frac{(\boldsymbol{k} \cdot \boldsymbol{M})\boldsymbol{k}}{k^2}] \end{aligned} \tag{A2-26}$$

Analogous to the discussion following (A2-7), the first term in the second line of (4.4) gives $4\pi \boldsymbol{M}(\boldsymbol{k})$, and the second term corresponds to the average demagnetizing field:

$$\langle H \rangle(k) = -\mathcal{N}(\boldsymbol{k}) \cdot \boldsymbol{M} \tag{A2-27}$$

with the elements of $\mathcal{N}(\boldsymbol{k})$ given by

$$\mathcal{N}_{ij}(\boldsymbol{k}) = 4\pi V_0 S(\boldsymbol{k}) \frac{k_i k_j}{k^2} \tag{A2-28}$$

and the elements of $\mathcal{N}(\boldsymbol{r})$ can be obtained by inverse Fourier transform (IFT):

$$\mathcal{N}_{ij}(\boldsymbol{r}) = \frac{4\pi V_0}{(2\pi)^3} \int_\infty d^3\boldsymbol{k}\, S(\boldsymbol{k}) \frac{k_i k_j}{k^2} \exp(i\boldsymbol{k} \cdot \boldsymbol{r}) \tag{A2-29}$$

Chapter 3

Sample preparation and experimental techniques

3.1. Selecting the materials

The experimental projects to be discussed in the following chapters will use different kinds of materials. Firstly, various thin film ferromagnetic samples, some of which will be patterned into elements under 100 nm in lateral size, need to be deposited. Permalloy, an alloy of ~ 80% nickel and ~ 20% iron (the atomic percentage ratio can span a wide range for different applications), is a good candidate for our experiments. It has a strong saturation magnetization ~ 800 emu/cm^3 under room temperature, and the Curie temperature is about 850 K (~ 580°C) [Bozorth1994]. Compared to some ferromagnetic metals (pure iron for example) that are vulnerable to oxidation and other degradations, Permalloy has good chemical stability to allow for several months of operations under ambient conditions. High quality polycrystalline Permalloy thin films can be readily grown using low-cost techniques such as magnetron sputtering, thermal evaporation and electron-beam evaporation. Coercive fields of Permalloy films magnetized along the easy axis are very low (typically a few Oersted) [Blois1955], making single-domain investigations easier. Permalloy films also have very small crystalline anisotropy (usually on the order of 10^3 erg/cm and can be minimized down to zero by changing the composition of Ni and Fe; in some applications, an external field is intentionally applied during the film growth to create an extra uniaxial anisotropy) [Smith1958, Lewis1964], which simplifies the systems under study.

Nonmagnetic metals are necessary to fabricate photoconductive switches and transmission lines for generating and carrying the excitation pulses. Gold (> 99.99%) is used for the switches because of its excellent chemical stability (copper switches also work, but have shorter life time). For the transmission lines, however, gold is not rigid enough since the coplanar structures are subject to direct contact and friction with the samples to be measured; therefore, a thick copper film (~ 250 nm) is grown first and then a gold cap layer of ~ 10 nm is deposited for chemical protection. In some cases, chromium (Cr) is also used to form a cohesion enhancement layer, because gold or copper films may not stick well on certain types of glass.

Finally, substrate materials need to be carefully selected according to different applications. The photoconductive switches are grown on semi-insulating GaAs substrates. The transmission lines are grown on ~ 1.5 mm thick borofloat glass, since they need to be relatively rigid. The Permalloy films, however, are grown on much thinner glass substrates (~ 150 μm) because the probe laser beam has to penetrate the substrate in some experiments. For the project covered in Chapter 5, the patterned Permalloy samples are very small (< 200 nm in lateral sizes) and the transmission lines have to be fabricated on the same substrate; for better results, sapphire substrates are used for such samples thanks to their excellent surface quality (they are single crystals), low electrical conductivity (to avoid short circuit between the transmission lines and the Permalloy elements) and high thermal conductivity (sapphire's 25.1 W/m·K versus borofloat's 1.2 W/m·K at ~ 100°C).

3.2. Sample fabrications

3.2.1. Substrate cleaning

Glass substrates (including sapphire) can be cleaned in hot Piranha solution for about 15 minutes; the recipe is 3:1 mixture of H_2SO_4 and H_2O_2. Operators must make sure that H_2O_2 is gently poured into H_2SO_4, not the other way, otherwise explosive damages may occur. The substrates are then rinsed in distilled water and are dried with a nitrogen gun. Piranha will destroy GaAs substrates (but OK for some other semiconductor wafers like Si), so diluted hydrochloric acid (< 20%) is used for cleaning. Noncorrosive recipes are also available, such as acetone and isopropyl alcohol (IPA), to clean the samples when metal films are already present.

3.2.2. Thin film deposition

Thin films of gold, copper and other nonmagnetic metals were deposited in the sputtering system in the Nanofab. The system can be pumped down to $\sim 5 \times 10^{-7}$ Torr, and two targets can be mounted in the main chamber, so that bilayers of copper and gold (for the transmission lines) can be deposited without breaking the vacuum. However, this sputtering system cannot monitor the film thickness *in situ*; the Nanofab staff offers calibration data for a variety of materials, and the film thickness can be measured more accurately using the Nanofab's Alphastep 200 profilometer.

The Permalloy films were deposited using electron beam evaporation because the Nanofab's sputtering machine does not show satisfactory burning conditions for the Permalloy target that used to be good (e.g. for the Ph.D projects conducted by Belov [Belov2004]). E-beam evaporation can be done in the Nanofab and in the high vacuum lab of the Department of Physics. Both systems have a digital crystal thickness monitor to measure the film thickness and the deposition rates, thus the rates can be controlled by adjusting the electron beam intensity. The system in the Physics building also has a thermal couple attached to the substrate holder to measure the substrate temperature, since there are concerns that the melted metals in the evaporation chamber may overheat the substrate and damage some structures (such as photoresist patterns). Since the Permalloy films are quite thin in these projects and do not need a long growth time, the measured substrate temperatures never exceeded 80°C. The base pressures of the evaporation systems are in the same level with the sputtering system.

3.2.3. Micrometer-scale patterning: photolithography

The Nanofab's photolithography facilities include a pattern generator, three mask aligners specialized for different wavelengths, and equipments for wet-processing, baking, spin-coating, etc. The masks were first designed using Tanner L-Edit® layout editor. The designs were then converted into standard GDSII files that can be processed by the pattern generator (Heidelberg DWL-200). Raw masks are 4-inch square quartz plates and have an opaque chrome layer covered by a HPR504 photoresist layer. The pattern generator decomposes the photoresist in the specified areas with a focused laser beam, thus minimum features ~ 1 μm can be safely generated. But the following steps of resist developing and Chrome etching are tricky handwork, so the minimum features of the finished masks are 1.5 ~ 3.0 μm.

The cleaned substrates are firstly spin-coated with a LOR-series (MicroChem Corp.) resist layer, depending on the desired thickness of the thin films; LOR-5B is usually adopted for samples below 300 nm. Then a second spin-coating is processed with HPR504 resist. When such samples are exposed under ultraviolet light (for 4.0 second) in the mask aligner, the decomposing rate of the top HPR504 layer is lower than the bottom LOR layer, such that an "undercut" structure can be generated after the decomposed resists are removed by standard developing procedures, as shown in Fig.3-1. Thin films are then grown on these developed samples, as introduced in Section 3.2.2. The undercuts can avoid the deposited materials from sticking with the bottom resist layer and being damaged in the lift-off process (using Remover PG from MicroChem Corp., operating temperature 70 – 80°C).

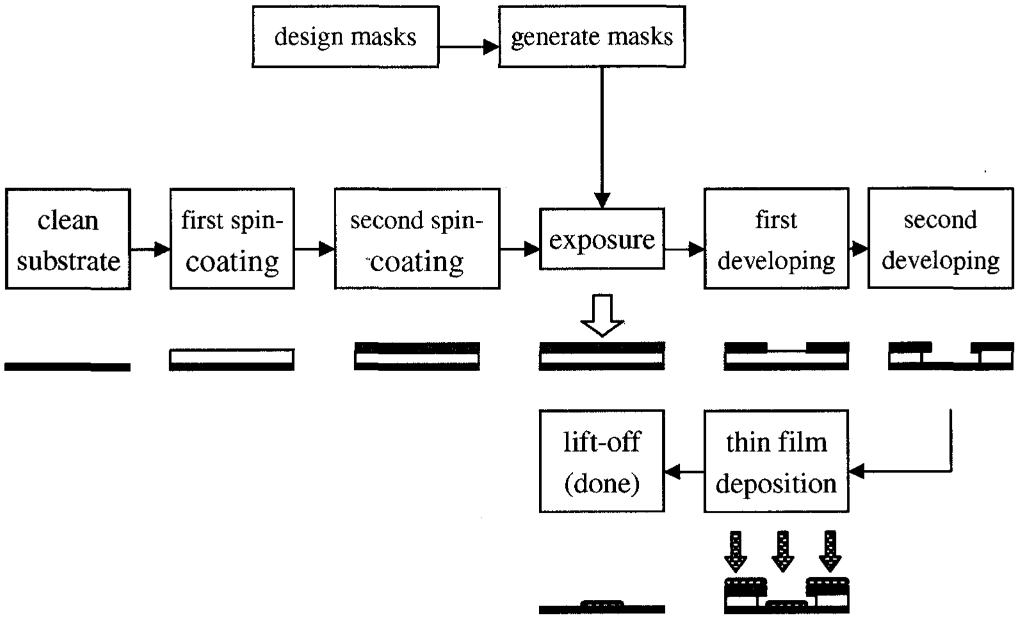

Fig.3-1: Flowing chart for double-resists photolithography. The cartoons beneath some of the charts are schematics of the samples at the corresponding stages. The thicknesses of the substrate and the resist layers are not drawn in-scale for visibility.

Two types of samples were fabricated by photolithography: transmission lines and photoconductive switches. The size parameters of the transmission lines are the width of the two striplines and the gap between them, w, and the length of the *parallel* part of the striplines, L. For the project covered in Chapter 4 (magnetostatic spin waves in continuous Permalloy films), $w = 3$ μm and $L = 400$

μm; the particularly long striplines can ensure the excited spin waves to be quasi-one-dimensional. For the project covered in Chapter 5 (spin dynamics in Permalloy nanomagnets), the striplines do not need to be long, so w = 3 μm and L = 80 μm. A major difficulty in fabricating the photoconductive switches arises because it takes *two* rounds of photolithography. The first layer is thin (~ 10 nm) and has wider finger structures; the second layer is aligned right on top of the first layer, but is thick (~ 250 nm) and has narrower fingers, as shown in Fig.3-2. This design can reduce the illumination loss due to the shadow of the fingers when the pump beam is not perfectly perpendicular to the sample plane.

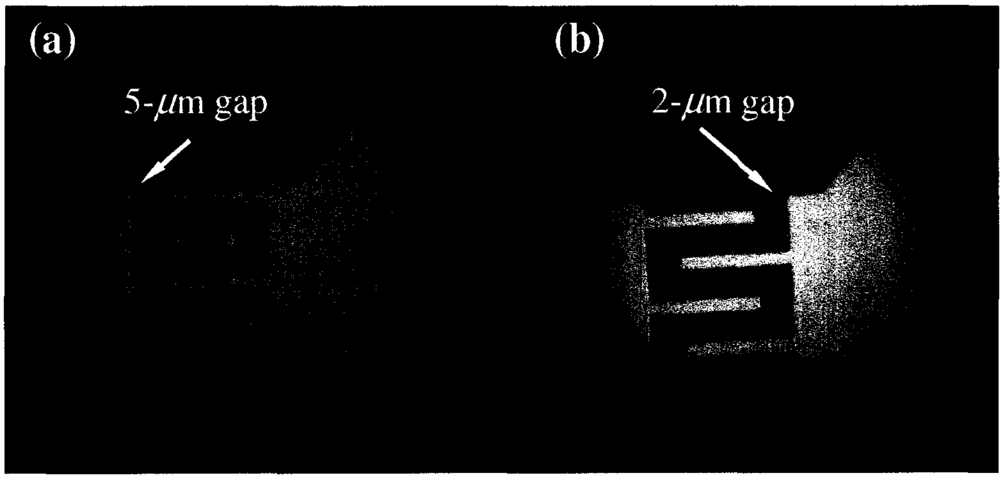

Fig. 3-2 (color): Images of photoconductive switches fabricated through the two-step photolithography scheme described in the text.

The minimum feature of the samples fabricated by photolithography depends on various factors. The spatial resolution of the pattern generator is determined by the diffraction limit of the focused laser beam, which is significantly less than 1 μm for the Heidelberg DWL-200 model in the Nanofab. The subsequent photoresist developing and chrome etching will slightly enlarge the openings, but for skilled operators, the minimum feature on finished masks can still be less than 1 μm. When the patterns are to be converted onto the substrates covered with photoresist, further difficulties will come up, especially in the second developing process for creating the undercuts (the developer for LOR-series resist is Shipley's MF-319). If the developing time is too short, the lateral size of the undercuts may not be enough to avoid the metal structures from sticking with the photoresist; if the developing time is too long instead, the undercuts may be too large and neighboring resist openings may crash with each other and the sample will fail. These complications make the minimum feature of the finished samples larger than 1 μm. Fig.3-3 shows the image of transmission lines with w = 1.5 μm, which is the smallest feature ever produced in these projects. It can be seen that the gap looks a little larger than the width of the striplines, which may also be attributed by the undercut size.

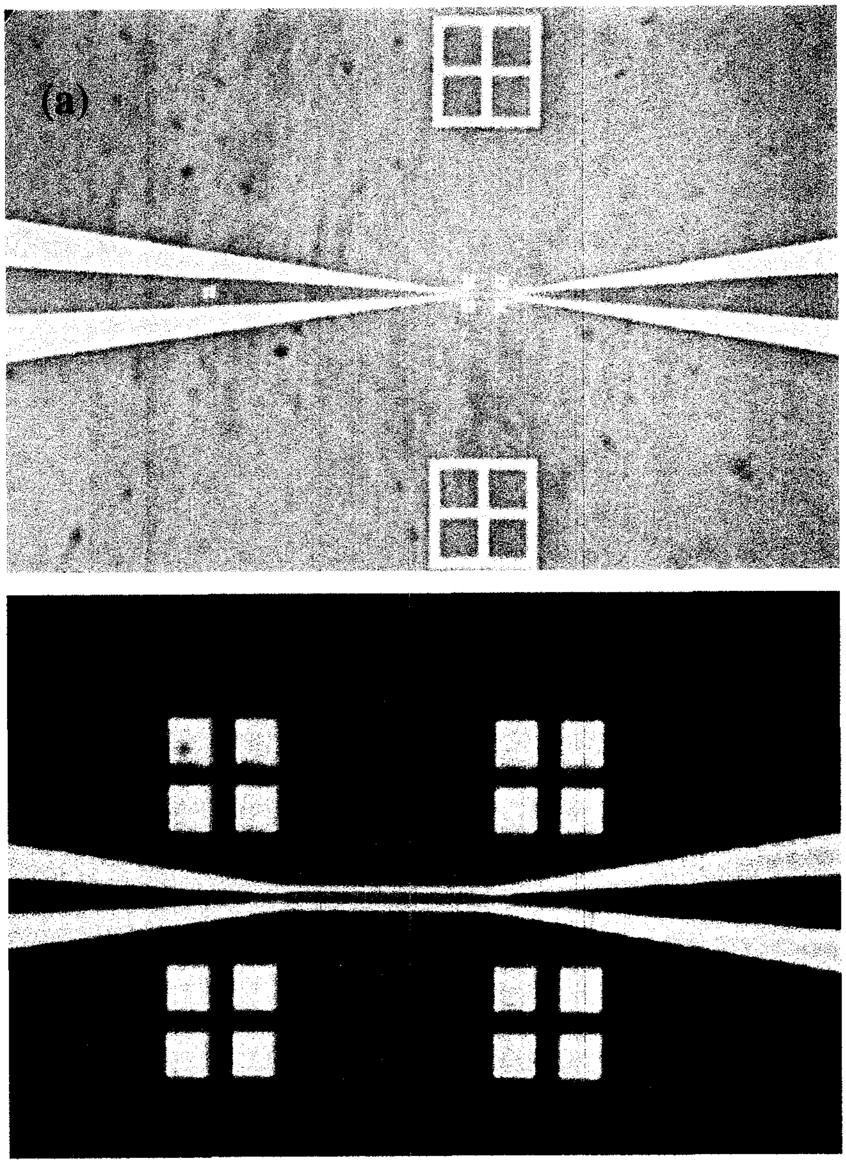

Fig. 3-3 (color): The smallest structures generated by photolithography. (a), the zoom-out image of the transmission lines with $w = 1.5\ \mu m$ and $L = 40\ \mu m$. (b), the zoom-in image of the same transmission lines.

3.2.4. 10^2-nm-scale patterning: electron beam lithography

To fabricate sub-μm structures like the Permalloy nanomagnets to be discussed in Chapter 5, electron beam lithography (EBL) is utilized taking advantage of the Nanofab's Raith150 system (whose ultimate resolution is down to 20 nm). The patterns are designed using L-Edit® and are converted into GDSII files. The resists used in EBL are copolymer EL6 (bottom layer) and polymethylmethacrylate (PMMA) 950 (top layer); they are spin-coated on cleaned sapphire substrates by using Head-way Resist Spinner. The electron exposure rates are different for the two resists so that after being developed, the resists openings will have undercuts analogous to the photolithography case. The metallization is done by e-beam evaporation, as introduced in Section 3.2.2. The lift-off is performed in an acetone bath for about 20 minutes, assisted by an ultrasonic treatment. Then, the samples with Permalloy nanostructures are immediately processed with the second round of photolithography to fabricate the transmission lines. A number of markers are carefully designed around the nanomagnets and transmission lines that can match each other by using the mask aligner. The details of the designs and the samples will be presented in the first section of Chapter 5.

3.3. Time-resolved magneto-optical Kerr effect microscopy

To measure magnetization *dynamics* using the polar Kerr effect introduced in Section 2.6, it is the *change* of M_z with respect to its equilibrium value that needs to be concerned. The reflected probe beam which contains the Kerr signals is usually analyzed by a polarization-dependent beam splitter such as the Glan-Thompson prism. The outcoming *s*-light and *p*-light are separately collected by a pair of semiconductor photodiodes. When the system is at equilibrium, the photodiodes are manually balanced to give equal signals; consequently, any out-of-equilibrium Kerr signals will be obtained by subtracting the off-balanced signals from the two photodiodes. This differential approach can enhance the signals by a factor of two, and can reduce noise by common-mode rejection.

To perform time-resolved measurements, an optical time delay is established between the pump and probe beams; by setting a proper starting point t_0 (usually ~ 200 ps before the onset of the excitation pulse) and then controlling the time delay Δt, the evolution of the magnetization $M_z(t_0 + \Delta t)$ can be monitored. The time delay can be as large as ~ 5 ns, and can be changed almost continuously (the time resolution is less than 0.5 ps for the current settings, and can be further refined by using better gearing shafts). On the other hand, spatially resolved measurements are implemented by mounting the sample onto a piezo-stage, which can move in three dimensions (while the probe beam and the objective lens are fixed); the spatial resolution of the piezo-stage is less than 50 nm, much better than the diffraction limit of the optical objectives.

Since the magnetic signals are very small (typical Kerr rotation angles are 10^{-5} – 10^{-3} rad), the pump-probe measurements are performed in a stroboscopic scheme. A 2.3 kHz reference signal is used to trigger the pump pulses, and the data acquisition system is also phase-locked at this frequency. Then the signals from about 10^3 repeated events can be summed up to yield notable signals (10^2 – 10^3 μV).

Chapter 4:

Locally-excited magnetostatic spin waves in Permalloy films

4.1. Project overview.

The main purpose of this project is to measure and quantitatively explain the spin wave dynamics excited by spatially inhomogeneous magnetic pulses in a continuous Permalloy film (that is, the sample itself is spatially homogeneous). These pulses are generated by the photoconductive switch and transmission lines introduced in Section 3.2; the excited spin waves in the Permalloy film are measured by means of time-resolved scanning Kerr effect microscopy; the measured data are then compared with results calculated by micromagnetic simulations and by a semi-analytical method. Emphasis will be taken on the properties of the localized pulse (in both the real space and the Fourier space) and their effects on the spin wave dynamics. Main results of this project has been published in Ref.[Liu2007].

4.2. Experiment details and representative results.

The Permalloy film was deposited on a 150 μm thick glass substrate using e-beam evaporation introduced in Section 3.2, with a base pressure of ~ 7×10^{-7} Torr and a deposition rate of ~ 0.2 Å/s. The film thickness was measured *in situ* by the crystal thickness monitor to be 10 ± 1 nm. The substrate was then cut into pieces of about 3 mm in size, and was clamped on a 3-μm wide, 400-μm long transmission line structure that has also been introduced in Section 3.2 (although the sizes are different with what were shown in Fig.3-3). A small amount of high-vacuum dielectric grease (Dow Corning® High Vacuum Grease) was applied to stick the Permalloy film on the transmission lines with a strong surface-tension bond and to ensure electrical isolation.

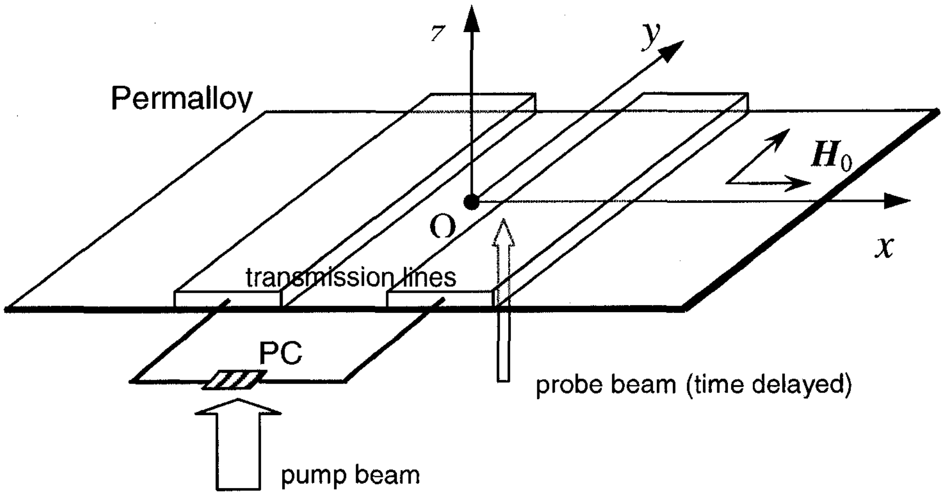

Fig.4-1: Schematic of the experiment layout. The coordinates system is also defined.

In some of our previous experiments [Zhu2005APL, Zhu2005JAP], the probe beam had to penetrate through ~ 1.5 mm thick glass (the substrate for the transmission lines) before hitting the magnetic film. The sample holder was also ~ 1.5 mm thick, so the working distance of the objective lens cannot be very short, limiting the measurement's spatial resolution. In this project, thanks to the thin glass substrate, the whole sample was mounted in a reverse way such that the probe beam penetrated through the 150-μm glass to reach the Permalloy film, as illustrated in Fig.4-1. Thus, an objective lens with numeric aperture (NA) = 0.9 can be used, allowing for spatial resolution down to ~ 500 nm. Some other experiments also adopted this alignment but the measurements were not taken in *scanning* mode and spatial resolution was not a critical concern [Buchanan2004, Buchanan2005, Zhu2005PRB].

A bias field $\boldsymbol{H}_0$ was applied in-plane (i.e., parallel to the film plane). Because of the low coercive field for Permalloy, the static magnetization $\boldsymbol{M}_0$ was sufficiently saturated to be parallel to $\boldsymbol{H}_0$ in the interested range (H_0 = 30 – 300 Oe). In this project, the bias field was either parallel to the transmission lines or perpendicular to them, corresponding to two typical geometries in spin wave studies: $\boldsymbol{k} \perp \boldsymbol{M}_0$ and $\boldsymbol{k} \mathbin{/\!/} \boldsymbol{M}_0$.

The measurements were typically carried out in scanning mode, that is, the Kerr effect signals were collected together with the spatial scans, which requires much longer integration time for the lock-in amplifier than pure spatial scans (which only record reflected light intensity). The scans were taken one dimensionally, along the direction of the $\boldsymbol{k}$ vector (i.e., perpendicular to the transmission lines). Thus, a two dimensional dataset can be obtained after each scan, with a time axis and a spatial axis. Representative intensity images are shown in Fig.4-2(a,c), and their corresponding magnetic images are shown in Fig.4-2(b,d). It can be seen that the spin waves behave very differently for the two excitation schemes. In the $\boldsymbol{k} \perp \boldsymbol{M}_0$ geometry, the spin waves are clearly moving along the x-axis (Fig.4-2(b)), while the spin waves appear to be stationary in the $\boldsymbol{k} \,//\, \boldsymbol{M}_0$ geometry (Fig.4-2(d)). These two distinct behaviors were then measured under varying bias fields (both parallel and perpendicular to the transmission lines) for further analyses.

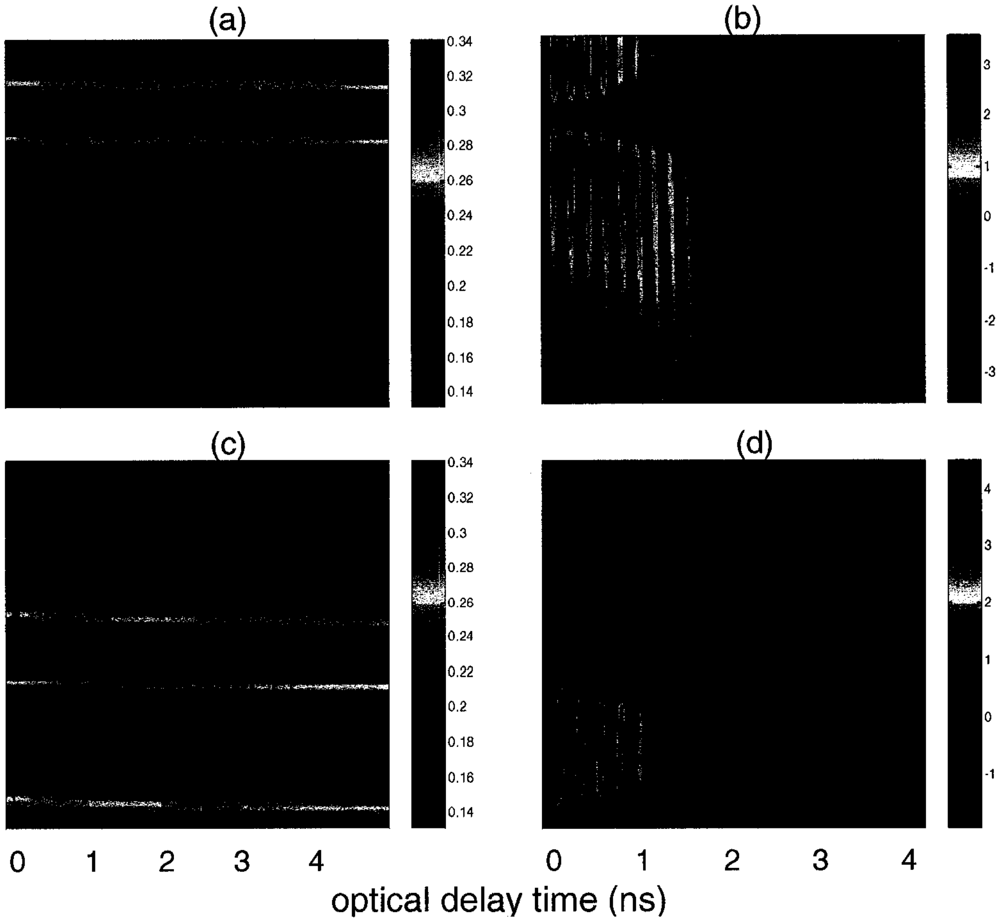

Fig. 4-2 (color): Typical experimental data obtained by TRSKEM. The scans are 1-dimensional along the x-axis; the horizontal axis gives the optical delay time, and the vertical axis gives the locations along the x-axis. The color bars represent normalized values of corresponding channels of the lock-in amplifier, therefore are dimensionless. **(a)**, spatial image near one of the transmission lines. The red area is the transmission line, and the blue area is the background (substrate etc.). **(b)**, polar Kerr signals obtained from the area shown in (a). The colors represent for the $M_z(x,t)$ values and are scaled from minimum (blue) to maximum (red). Orientation and strength of the bias field are shown, corresponding to the $\boldsymbol{k} \perp \boldsymbol{M}_0$ geometry. **(c)**, spatial image above one of the transmission lines. **(d)**, the magnetic image for the area shown in (c), with the bias field is rotated for 90° as compared to the case in (b), corresponding to the $\boldsymbol{k} \,/\!/\, \boldsymbol{M}_0$ geometry.

4.3. Semi-analytical analysis: *k*-space integration

Spin wave theories in thin film ferromagnetic materials have been well established, as briefly introduced in Chapter 1 and 2. Most types of magnetization dynamics, which may be characterized by small-amplitude perturbations (spin waves) or large-angle rotations (magnetic switching), should be continuous and smooth functions of time and space, so they can always be expressed as the superposition of their Fourier components. Theoretically, the wavelength of these components can go from zero to infinity, but the "dominant" range should match the characteristic length of the excitation source. In this experiment, this characteristic length is ~ 3 μm (width and gap of the transmission lines), so the majority of excited spin waves are within the magnetostatic limit, which means the exchange interaction can be neglected (recall the discussion in Section 2.4.3).

Under the condition of linear behavior of magnetostatic spin waves in the small-amplitude regime, the magnetic response is the linear superposition of all plane wave components that can be excited by the pulse. The magnetic energy of these spin wave components dissipates into non-magnetic environment with practically a single damping rate (*intrinsic* damping) [Suhl1998]. In our case, since the spin waves will only propagate in x-direction (perpendicular to the transmission lines), the out-of-plane component of magnetization can be described by:

$$M_z(x,t) \propto e^{-t/\tau} \int_0^{k_c} P(k,\omega(k)) \sin[kx - \omega(k)t + \varphi] dk \qquad (4\text{-}1)$$

where τ is the intrinsic damping rate, $\omega(k)$ is the dispersion relation, and $P(k, \omega(k))$ is the spectral density of the pulse field determined from its spatial and temporal profiles and acts as a relative weighting factor for the different spin wave components in k-space. k_c is the length of a cut-off wave vector for numerical integration ($k_c = 5\ \mu\text{m}^{-1}$ is sufficient for the magnetostatic spin wave regime). The initial phase angle φ is taken to be independent of frequency on account of the pulse excitation. This equation is actually a Fourier integral representation for $M_z(x,t)$, and explicitly includes the influences of the pulse field parameters, the intrinsic damping, and the dispersion relation of the spin waves.

To calculate Eq.(4-1), the dispersion law of spin waves must be known. According to the magnetostatic spin wave theories discussed in Section 2.4.4, the $\boldsymbol{k} \parallel \boldsymbol{M}_0$ geometry will produce magnetostatic backward volume waves (MSBVW) with the dispersion law given by Eq.(2-63), while the $\boldsymbol{k} \perp \boldsymbol{M}_0$ geometry is responsible for magnetostatic surface spin waves (MSSW), whose dispersion law is given by Eq.(2-60). These geometries are schematically shown in Fig.4-3(a,b).

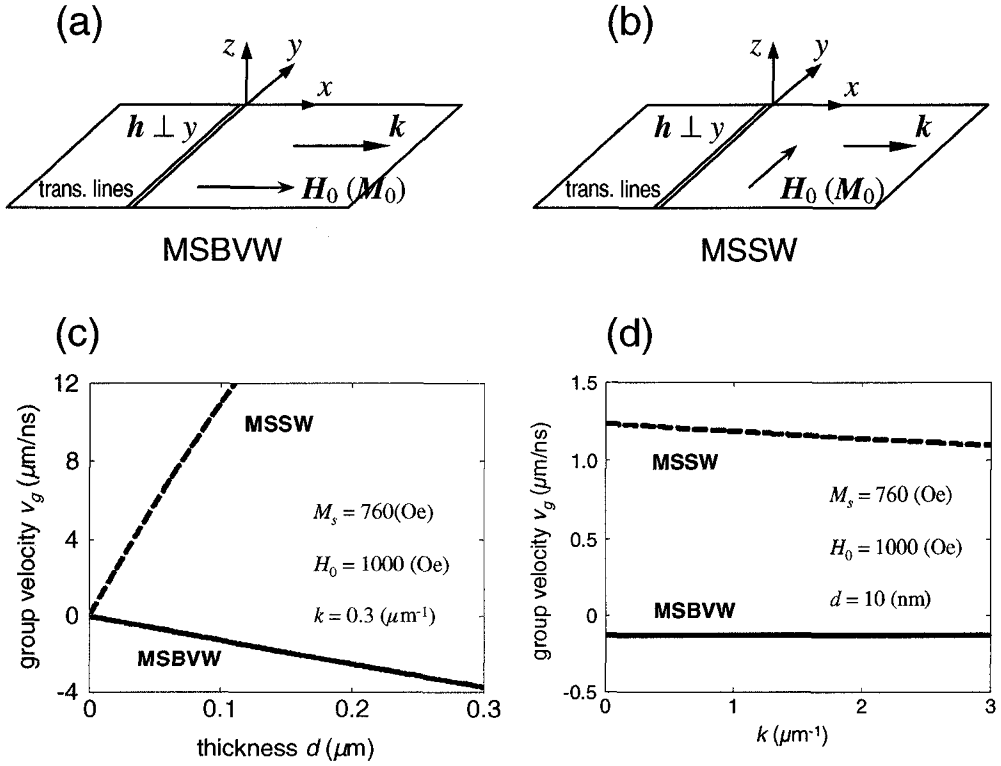

Fig. 4-3: (a), excitation scheme for magnetostatic backward volume waves (MSBVW). (b), excitation scheme for magnetostatic surface waves (MSSW). (c), group velocity as a function of film thickness for MSSW and MSBVW, under the given conditions. (d), group velocity as a function of wave vector for MSSW and MSBVW.

Another important quantity to be determined is the weighting factor $P(k, \omega(k))$, which is closely related to the Fourier space representation of the spin wave dynamics. A standard linearization method can be used here to solve the problem. The linearized LLG equation without the damping term can be expressed as [Gurevich1996]

$$i\omega \boldsymbol{m} + \gamma \boldsymbol{m} \times \boldsymbol{H}_0 = -\gamma \boldsymbol{M}_0 \times \boldsymbol{h} \qquad (4-4)$$

If the Gilbert damping is taken into account, the final results will contain α with power of two or even higher, and only lead to minor corrections. In Cartesian coordinates system, the three components of Eq.(4-4) are:

$$\begin{cases} i\omega m_x + \gamma(m_y H_{0z} - m_z H_{0y}) = -\gamma(M_{0y} h_z - M_{0z} h_y) \\ i\omega m_y + \gamma(m_z H_{0x} - m_x H_{0z}) = -\gamma(M_{0z} h_x - M_{0x} h_z) \\ i\omega m_z + \gamma(m_x H_{0y} - m_y H_{0x}) = -\gamma(M_{0x} h_y - M_{0y} h_x) \end{cases} \qquad (4-5)$$

For the $\boldsymbol{k}$ // $\boldsymbol{M}_0$ geometry, certain terms in Eq.(4-5) will vanish except $H_{0x} \neq 0$, $M_{0x} \neq 0$, $h_x \neq 0$, $h_z \neq 0$ (see Fig.4-3(a)), so the equation reduces to:

$$\left\{\begin{array}{l} i\omega m_x = 0 \\ i\omega m_y + \gamma m_z H_{0x} = \gamma M_{0x} h_z \\ i\omega m_z - \gamma m_y H_{0x} = 0 \end{array}\right. \xrightarrow{\gamma H_{0x} \to \omega_H,\ \gamma M_{0x} \to \omega_M} \left\{\begin{array}{l} m_x = 0 \\ i\omega m_y + \omega_H m_z = \omega_M h_z \\ -\omega_H m_y + i\omega m_z = 0 \end{array}\right. \qquad (4-6)$$

The solution for m_z is then

$$m_z = \frac{\omega_M}{\omega_H^2 - \omega^2} \cdot \omega_H h_z \qquad (4-7)$$

For the $\boldsymbol{k} \perp \boldsymbol{M}_0$ geometry, the non-vanishing terms are $H_{0y} \neq 0$, $M_{0y} \neq 0$, $h_x \neq 0$, $h_z \neq 0$ (see Fig.4-3(b)), so Eq.(4-5) reduces to

$$\begin{cases} i\omega m_x - \gamma m_z H_{0y} = -\gamma M_{0y} h_z \\ i\omega m_y = 0 \\ i\omega m_z + \gamma m_x H_{0y} = \gamma M_{0y} h_x \end{cases} \xrightarrow{\gamma H_{0y} \to \omega_H,\, \gamma M_{0y} \to \omega_M} \begin{cases} i\omega m_x - \omega_H m_z = -\omega_M h_z \\ m_y = 0 \\ \omega_H m_x + i\omega m_z = \omega_M h_x \end{cases} \qquad (4-8)$$

The solution is:

$$m_z = \frac{\omega_M}{\omega_H^2 - \omega^2}(\omega_H h_z + i\omega h_x) \approx \frac{\omega_M}{\omega_H^2 - \omega^2} \cdot i\omega h_x \qquad (4-9)$$

The right hand sides of Eq.(4-7) and Eq.(4-9) quantify the magnetic pulse's "ability" to excite a spin wave component with given wave vector k and frequency ω. They should then be proportional to $P(k, \omega(k))$ for the corresponding geometries. Therefore, the weighting function is just the Fourier transform of the pulse shape, multiplied by a frequency-dependent factor. The pulse profile as a function of x is calculated based on the Biot-Savart law. Typical results for $h_x(x)$ and $h_z(x)$ are shown in Fig.4-4(a). The total pulse strength, $h = (h_x^2 + h_z^2)^{1/2}$, is also shown by the solid curve. The Fourier transform of the fields, $h_x(k)$ and $h_z(k)$, are shown in Fig.4-4(b); they have exactly the same profiles, as expected. The pulse profiles (in both real- and k-space) strongly depend on the gap between the film plane and the top plane of transmission lines, which is denoted as Δ. Accurate measurement of Δ is not quite feasible under the current experimental conditions, so it acts as a fitting parameter in the calculations in Section 4.6 (Δ = 500 nm in Fig.4-4). It is also found that the ω-dependent quantities are insignificant in the calculations (except for a negative sign if $\omega > \omega_H$), so the weighting function can be well approximated by $P(k) = |h(k)|$.

The dispersion relation $\omega(k)$ also determines the group velocity of the excited spin waves: $v_g \equiv d\omega/dk$. Although this quantity is not necessary in doing the k-space calculation, it is worthwhile to show it now because some of the discussions presented in the next few sections will rely on the understanding of group velocity. Fig.4-3(c) presents the group velocities of MSBVW and MSSW as a function of film thickness for a given wave vector, and in Fig.4-3(d) group velocities vary with the wave vector for a given film thickness (10 nm). In both scenarios, MSBVW propagates much slower than MSSW and can be considered effectively stationary [Bailleul2001]. Moreover, in a thin film (thickness is fixed), v_g is effectively independent of wave vectors, i.e., it is insensitive to the spatial properties of the excitation pulse.

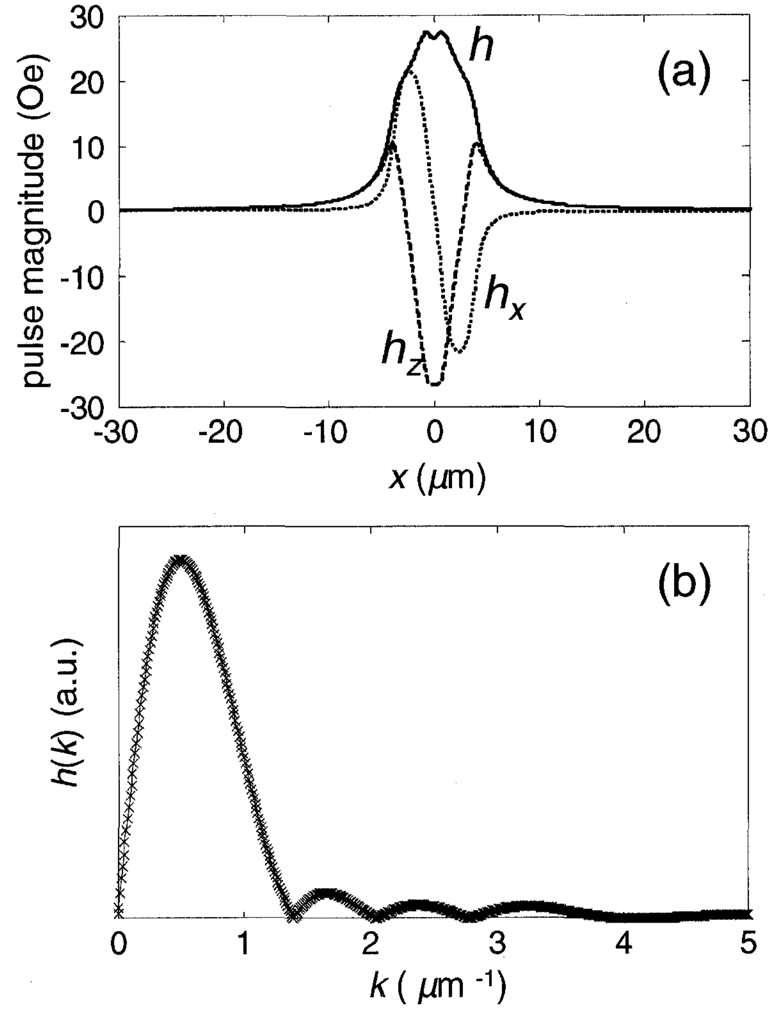

Fig. 4-4: Calculated spatial properties of the magnetic pulse. (a), the field components h_x (dotted curve), h_z (dashed curve), and the total field strength h (solid curve) as a function of x, with $\Delta = 500$ nm. (b), Fourier transforms of h_x (solid curve) and h_z (crosses). Their profiles are identical.

After the dispersion law and the *k*-space weighting function are known, Eq.(4-1) can be numerically integrated along *k*-axis using a sufficiently small step, such as 0.001 μm^{-1}; the memory and time required for the computer calculation are much less than what would be required in a micromagnetic simulation.

4.4. Micromagnetic simulation: a quasi-one-dimensional version.

Micromagnetic simulation serves in this project as a “bridge” tool to explain the experimental results and to test the proposed semi-analytical *k*-space calculation. The spatial scale of the system raises certain difficulties, because the spin waves are expected to propagate for tens of micrometers before damping out. Thus, periodic boundary conditions have to be applied to allow spin waves freely to move away, instead of being reflected back by numerical boundaries that are not present in the experiments. Furthermore, these periodic boundary conditions can also produce unwanted spin waves as if they come from a pair of “mirror” transmission lines, as illustrated in Fig.4-5 which is a schematic of the simulation model. As a result, the calculation must be able to cover at least 100 μm in the propagating direction (along x-axis in our case), which is formidably large for any two dimensional simulation model (the third dimension, along the z-axis, can always be neglected thanks to the small thickness (~ 10 nm)).

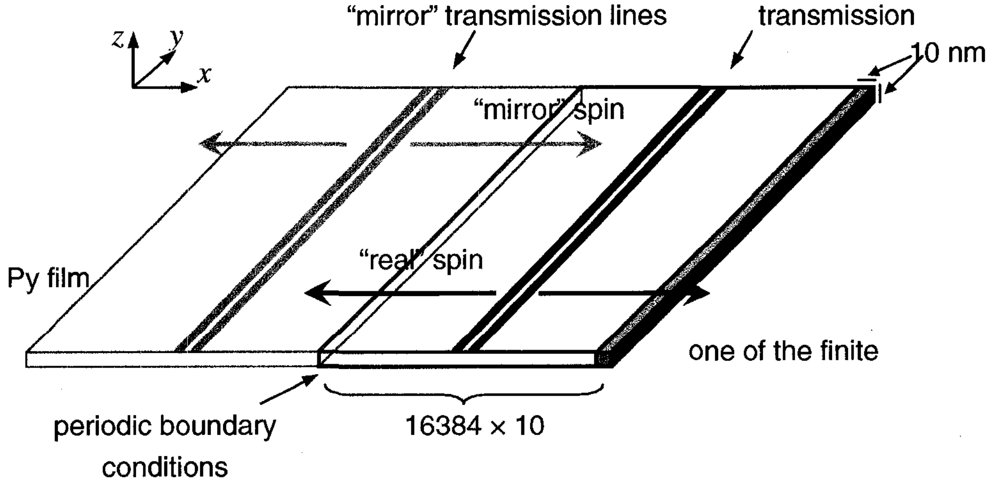

Fig. 4-5: The quasi-1D micromagnetic simulation model. The actual grid is drawn by the dark box, and the transmission lines are located in the middle (the actual input will be the magnetic pulse generated by them). The grey box is one of the "mirror" grids as the consequence of the periodic boundary conditions. The "mirror" transmission lines and the generated "mirror" spin waves are also illustrated.

In this project, the FORTRAN simulation codes are modified into a one dimensional version, taking advantage of the system's symmetry along the y-axis (the directions of the transmission lines). As shown in Fig.4-5, the thin film is discretized only along the x-axis. The "finite elements" are 10 nm in both x- and *z*-directions, while infinitely long in *y*-direction. The spin motion of each element obeys the Landau-Lifshitz-Gilbert (LLG) equation. The spin wave dynamics is then simulated in accordance with the experimental conditions (except for the pulse profiles which use the calculated results introduced in Section 4.3). Calculated spatiotemporal datasets for $M_z(x,t)$ are collected in similar way as in the experiments. Fig.4-6 shows representative results simulated for $\boldsymbol{k} \perp \boldsymbol{M}_0$ and $\boldsymbol{k} \,//\, \boldsymbol{M}_0$ geometries. The main features, such as the effectively stationary volume waves and the propagating surface waves can be clearly sorted out, in consistence with the observations. More quantitative analyses will be presented in the next two sections.

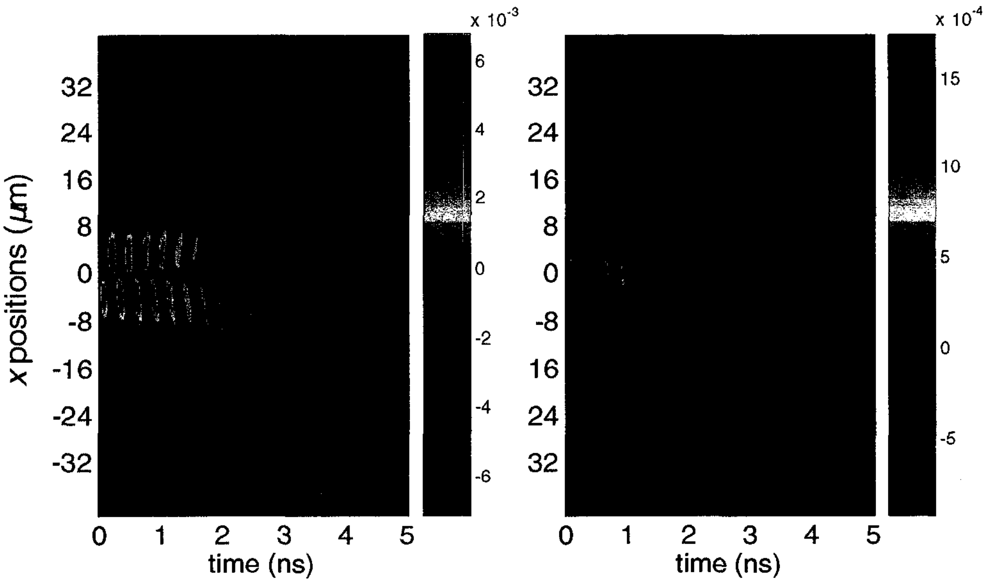

Fig. 4-6 (color): Representative results obtained by the quasi-1D micromagnetic simulations. The color bars represent the normalized out-of-plane magnetization (M_z / M_s). The bias field strength is 200 Oe for both cases, but is differently aligned to generate **(a)**, MSSW and **(b)**, MSBVW, respectively. The pulse field remains the same.

4.5. Results in the "source" area: spin wave relaxation and the determination of α

In this section, the magnetization dynamics near the excitation source is considered. As can be seen in Fig.4-4(a), the magnetic pulse is highly localized near the transmission lines that its components quickly fade to under 10% of the maximum amplitude when $|x| > 8\ \mu$m. The area for $|x| \leq 8\ \mu$m can be defined as the "source" area. The magnetic energy is initially pumped in the source area and then is transferred into the so-called "propagation" area ($|x| > 8\ \mu$m), also accompanied with the intrinsic damping. The main results can be obtained at $x = 0$, because optical imaging on this point will not be significantly affected by the nearby transmission lines, and the dynamics at other points inside the source area is qualitatively similar to $M_z(0,t)$. This kind of measurement can be taken in either scanning mode (for consistent comparison with other points) or stationary mode (to save time).

4.5.1. Volume waves in the $\boldsymbol{k}$ // $\boldsymbol{M_0}$ geometry.

Fig.4-7 presents the results for spin wave dynamics at $x = 0$, when a bias field of 200 Oe is applied perpendicular to the transmission lines. Good agreements can be seen between the measured data (solid curve), the micromagnetic simulation (circles), and the k-space calculation (crosses). The key observation in this $\boldsymbol{k}$ // $\boldsymbol{M_0}$ configuration is that other positions ($x \neq 0$) show almost the same profile but with amplitude decrease with increasing $|x|$. That is, the damping is spatially uniform and not influenced by the propagation of spin waves, consistent with the expectation for magnetostatic backward volume waves (recall the discussion on group velocities in Section 4.3). The Gilbert damping constant α is a fitting parameter in the LLG-based simulations, and the result here is $\alpha = 0.0081 \pm 0.0003$. However, this fitting is not enough to claim that the damping is exponential, although it should go that way according to spin wave relaxation discussed in Section 2.2.2. To verify this point in the measured waveforms, one can apply a low-frequency filtering to the data to remove the background tailing signals, and fit the resulted waveform with a function of the form $\sin(\omega t+\varphi_0)e^{-t/\tau}$, which can be realized in standard data processing software such as Origin and Matlab. However, to avoid applying any "canned" functions to the raw data, a simple algorithm is used here.

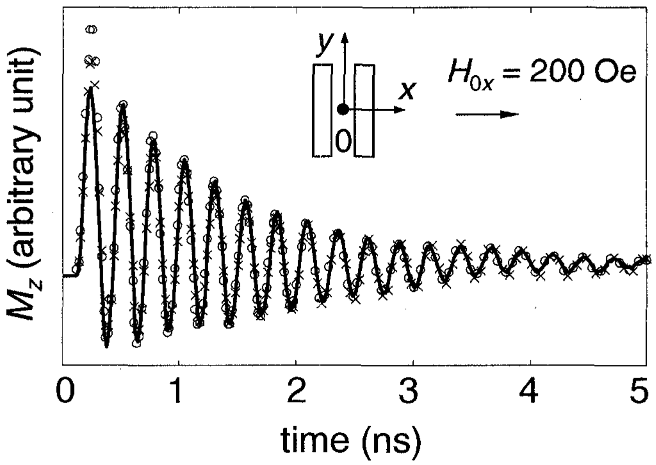

Fig. 4-7: Dynamics of MSBVW at x = 0, with the experimental conditions illustrated by the inset. The measured data are plotted by the solid curve, simulated results are plotted by the circles, and the crosses are calculated by the k-space integration method.

First, the maxima (peaks) and minima (valleys) of the oscillations are picked out. These two arrays have different time points, but can be cubic-interpolated onto a same time axis to outline the upper and lower envelopes of the waveform (Fig.4-8(a)). Generally speaking, data points for t < 0.5 ns are interfered with too much by the sharp peak of the pulse shape and are not considered; data points close to 5 ns are also dropped because the amplitudes have become too small to sustain a good signal-to-noise ratio. The difference between these two envelopes is a good approximation for the decaying amplitudes. Logarithms of the amplitudes data are plotted in Fig.4-8(b), showing fairly good linearity. The line's slope is then found by linear fitting, and the inverse of its absolute value gives the decay time, in this case $\tau = 1.40 \pm 0.01$ ns. Using the conversion formula between τ and α derived in Section 2.2.2 (Eq.(2-48)), the effective Gilbert damping is found to be $\alpha_\tau = 0.00817 \pm 0.00006$, which is consistent with that determined from the LLG simulation. Finally, this τ value is used in the k-space calculation (plotted by crosses in Fig.4-7); but keep in mind, the whole procedure can go in the opposite way – τ can be independently fitted with multiple runs of k-space calculations, and one can use this result to compare with experimentally determined τ, then work out the α value using Eq.(2-48) which the LLG simulations need.

Fig.4-8(c-d) show similar processing on the measured data with a much stronger bias field $H_0 = 1500$ Oe, so that more oscillation cycles are available to reduce fitting errors. In this case, the decay time is determined to be $\tau = 1.13 \pm 0.003$ ns, leading to $\alpha_\tau = 0.00803 \pm 0.00002$, again agrees well with the simulated result. This indicates that a *single* damping coefficient (α or τ) is sufficient to describe the spin wave relaxation in the $\boldsymbol{k} \,//\, \boldsymbol{M}_0$ geometry as long as the bias field is strong enough to fully saturate the magnetization in the probed area. The next question is: what about the $\boldsymbol{k} \perp \boldsymbol{M}_0$ geometry?

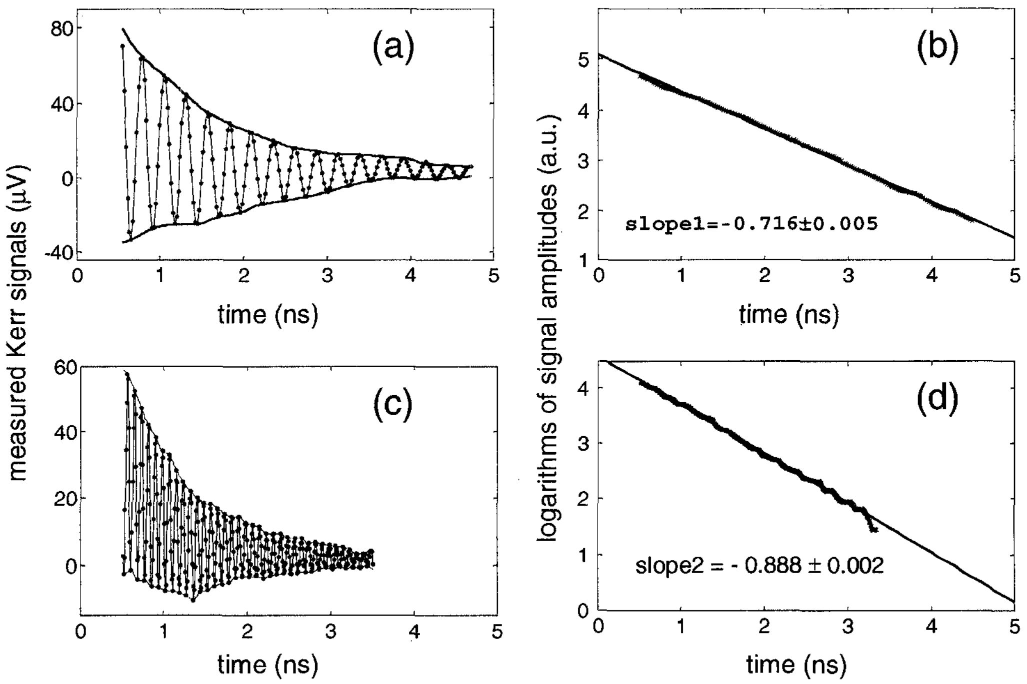

Fig. 4-8 (color): Procedures for fitting the exponential decay rate $1/\tau$ from the experimental data. **(a)**, The black curve corresponds to the experimental data in Fig.4-7. As explained in the text, data for $t < 0.5$ ns and t close to 5 ns are not considered. The upper and lower envelopes are plotted by red curves. **(b)**, logarithm plot of the amplitudes data in (a) (red); the slope is shown for the fitted straight line (blue). **(c – d)** show the same procedure when $H_0 = 1500$ Oe. Data for $t < 0.5$ ns and $t > 3.5$ ns are not considered.

4.5.2. Surface waves in the $k \perp M_0$ geometry.

In the $\boldsymbol{k} \perp \boldsymbol{M}_0$ geometry, the magnetization dynamics at $x = 0$ behaves very differently, but again, good agreements between the measurements, *k*-space calculations, and quasi-1D simulations have been obtained. Some examples are presented in Fig.4-9, when different bias field strengths (110, 200 and 300 Oe) are applied parallel to the transmission lines. The $M_z(0,t)$ traces show significantly enhanced apparent damping (compare Fig.4-9(b) to Fig.4-7), caused by the outflow of spin wave energy from the source area. The apparent damping also varies as H_0 changes; when H_0 goes stronger, the group velocity of MSSW decreases according to Eq.(4-11), which means that the spin wave energy will dissipate from the source area with a lower rate, leading to slower apparent damping.

In this configuration, it is clear that the MSSW's do not decay exponentially, so the intrinsic damping rate τ cannot be fitted directly from the experimental data as for the MSBVW's. As already mentioned in Section 4.5.1, we still can perform independent fittings by *k*-space calculations and the best estimates of τ's for different bias fields are also consistent with the simulated results since they both agree with the measured waveforms reasonably well. After these fitted τ values are translated into α_τ's, they are all fairly close to the simulated result 0.0081, although having a much larger error bar of about ±0.0006. The larger uncertainties are understandable because the surface waves have higher spatial inhomogeneity as compared to the relatively stationary volume waves. Therefore, the intrinsic damping parameter should preferably be determined using magnetostatic backward volume waves in the $\boldsymbol{k} \,//\, \boldsymbol{M}_0$ geometry.

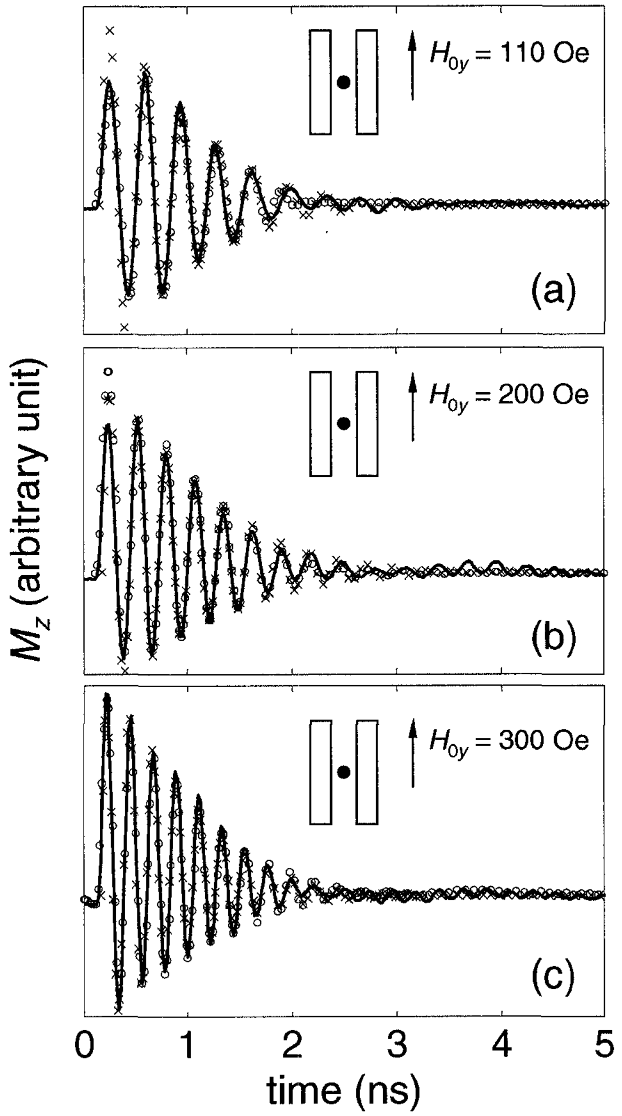

Fig. 4-9: Results obtained by similar approaches with what has been presented in Fig.4-7, but the bias field is aligned to generate MSSW's (with the $\boldsymbol{k} \perp \boldsymbol{M}_0$ geometry). The bias field strength is also varying: 110 Oe in **(a)**, 200 Oe in **(b)**, and 300 Oe in **(c)**.

4.6. Results outside the source area: propagation of individual spin wave packets

When the probing point is moved far away from the transmission lines ($|x| > 8$ μm), the spin wave dynamics for the $\boldsymbol{k}$ // $\boldsymbol{M}_0$ geometry is similar to what has discussed inside the source area (see Fig.4-2(d) and Fig.4-6(b) for the examples by experiment and simulation, respectively). The amplitudes of the oscillations are much smaller, as expected, due to the small local pulse fields. There are also phase lags of up to π, determined by the varying initial torques at different locations. These features, as well as the spatially uniform damping discussed in the last section, do not complicate the problem too much, so the following part of this section will focus on the surface waves in the $\boldsymbol{k} \perp \boldsymbol{M}_0$ geometry.

The results for $H_0 = 80$ Oe are shown in Fig.4-10. The previously determined damping constant $\alpha = 0.0081$ is directly used here, and once again the quasi-1D simulation (circles) and the k-space integration calculation (crosses) agree well with the experimental data. Of particular interest is the asymmetric shape of the wave packets – the increase of the oscillation amplitude appears "slower" than the following decline. Therefore this kind of spin dynamics cannot be accurately described by the Gaussian-type wave packet model (which is symmetric) proposed by Covington *et al.* [Covington2002], but has to be addressed by the more general approach based on Eq.(4-1).

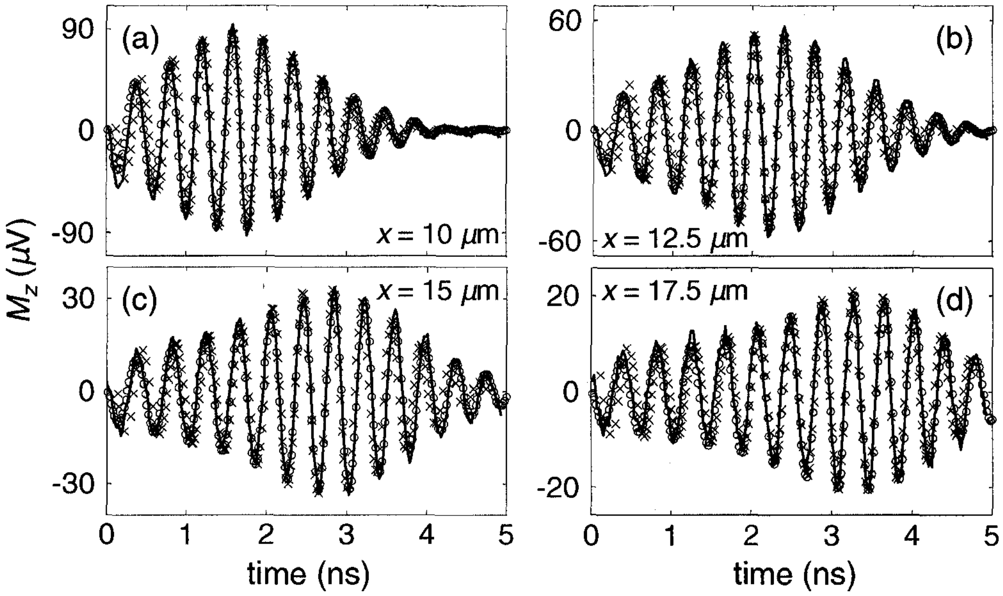

Fig. 4-10: Propagation of a spin wave packet. (a) – (d): $M_z(t)$ traces at $x = 10$, 12.5, 15 and 17.5 μm, respectively, when $H_{0y} = 80$ Oe. The solid curves represent the measured data, which are extracted from a single spatiotemporal scan, the crosses are the k-space calculation results based on Eq.(4-1), and the circles are the simulated results using the quasi-1D LLG model. The simulated and calculated waveforms are scaled to the same amplitude as the experimental data.

From Fig.4-10 it is clear that the group velocity of MSSW is high enough (several micrometers per nanosecond) to be observed in this type of experiment, as also been studied by a number of other groups [Brundle1968, Xia1998, Silva2002, Covington2002, Bailleul2003, Wu2006]. When the pulsed excitation is sufficiently localized in a few-μm region (as for our case and for Covington *et al.*) a well-defined spin wave packet can be observed; then it is quite easy to measure the group velocity – just find the peak times (t_p) of the traveling wave packets at different locations (x), and find the slope in the x-t_p plot by linear fitting. The results are presented in Fig.4-11, where the measurements (dots) and simulations (crosses) both agree with the theoretical prediction (the grey curve) within the studied bias field range (30 – 300 Oe). In some other experiments mentioned above, the excitations were not as localized and the observed surface spin waves did not show explicit wave packets, but the authors still could find the group velocity through a weighted integration algorithm (analogous to the method to find the center of mass of a rigid body).

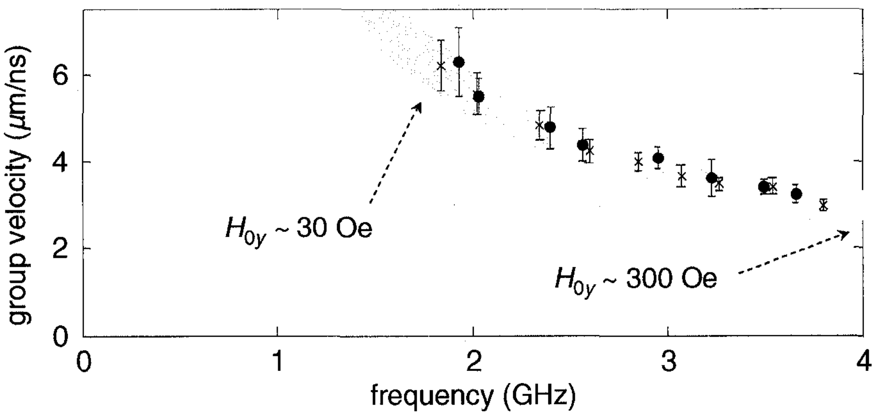

Fig. 4-11: Group velocity of the spin wave packet as a function of oscillation frequency, with H_{0y} ranging from 30 to 300 Oe. The black dots are measured data, and the crosses are results from quasi-1D simulations. The error bars are calculated from the time and space uncertainties when comparing different wave packets measured at different locations. The grey shadow is the theoretical curve calculated from MSSW dispersion law (Eq.(2-61)), with the width reflecting systematic uncertainty in the cutoff wavelength and film thickness ($k = 0 \sim 5\ \mu\mathrm{m}^{-1}$ and $d = 9 \sim 11$ nm.)

As mentioned in the last section, the gap Δ between the Permalloy film and the top plane of transmission lines is a parameter that significantly affects the spatial distribution of the pulse fields, and consequently can change the waveforms of MSSW. This effect can be demonstrated by first calculating the $P(k)$ distributions with different Δ values, as shown in Fig.4-12(a). These $P(k)$'s are then plugged in Eq.4-1 for the k-space calculations, and the results are shown in Fig.4-12(b-d). As Δ increases, the spatial variation of field becomes smoother and $P(k)$ acquires relatively higher spectral density at smaller k. This yields larger relative amplitude at early times before the wave packet peaks, and can be understood here as a consequence of more spin wave components with higher phase velocity $v_p = \omega/k$. Among the three figures, Fig.4-12(c) is the "best-fit" to the experimental data (already shown in Fig.4-10(d)), with $\Delta = 1.6$ μm. This Δ value is also used to fit all the waveforms in Figs. 4-7, 4-9 and 4-10, indicating that different bias fields do not influence the gap significantly (although the gap can still be changed by other experimental conditions – after all, this is a "free-chip" sample).

As the spin wave packet propagates farther away from the source, its shape is gradually broadened and the peak time eventually exceeds the maximum optical delay of the apparatus (5 ns). In this situation, the oscillations are dominated by small-k components. The experiments yield a unique position at each bias field ($x \approx 30$ μm for the case of $H_{0y} = 80$ Oe) where the incoming energy from the propagating mode effectively balances the intrinsic dissipation at that position, such that a nearly time-independent oscillation amplitude is observed throughout the measurement window, as shown in Fig.4-13(a). This "metastable" spin oscillation in response to a transient pulsed excitation might be useful in magnetic or spintronic devices. For larger *x*, the power balance is broken and the intrinsic decay of the long-wavelength oscillations dominates (Fig.4-13(b)).

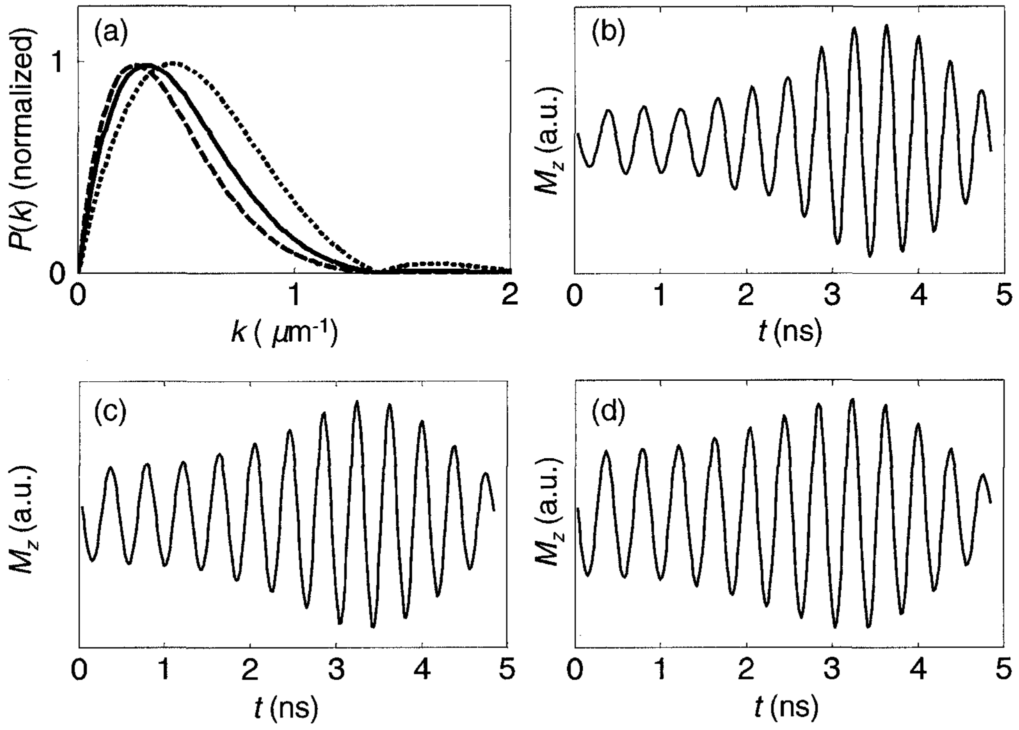

Fig.4-12: Influence of the spatial distribution of the pulse field. (a), Calculated distributions of $P(k)$ for $\Delta = 0.5$ μm (dotted curve), $\Delta = 1.6$ μm (solid curve), and $\Delta = 2.5$ μm (dashed curve). (b) – (d), $M_z(t)$ traces at $x = 17.5$ μm calculated with Eq.(1), using $\Delta = 0.5$ μm, $\Delta = 1.6$ μm, and $\Delta = 2.5$ μm, respectively.

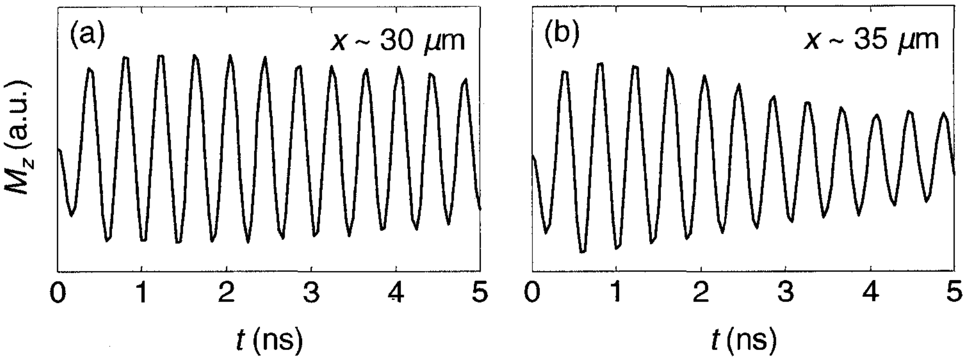

Fig.4-13: Spin wave oscillations measured at (a), $x \approx 30$ μm and (b), $x \approx 35$ μm. The experimental conditions are the same as those in Fig.4-10.

Chapter 5

Spin dynamics in individual Permalloy nanomagnets

5.1. The samples and the experiments

5.1.1. Introduction

As already introduced in Chapter 1, investigations on the magnetization dynamics in sub-micrometer thin film elements have been more and more active in recent years, and the size of the nanomagnets of interest has been decreased dramatically, due to the demand for high-density magnetic storage applications. A technical basis for realizing such applications is the different ground states of nanomagnets under certain conditions, such as the vortex state and quasi-single domain state in a ferromagnetic nanodisk. Therefore it is important to know how these states switch from one to another (state transitions). When the nanomagnets are too small, it can be very difficult to investigate them individually, and some experiments measure the total signals from a large number of elements in two-dimensional arrays, self-assembled composite, etc. [Cowburn1999, Kruglyak2005, Jausovec2006]. Uncertainties due to size and shape variation, and in some cases dipolar coupling within arrays, can give unclear information concerning the behavior of state transitions. Experiments on individual nanomagnets below 200 nm have recently begun to be reported [Krivorotov2005, Barman2006, Pribiag2007], focusing on either the vortex state or the quasi-single domain state. The present project is expected to measure and examine both of these two states and their transitions on individual Permalloy nanodisks with diameter less than 200 nm. Nanofab's e-beam lithography (EBL) system, Raith150, is utilized to fabricate such small structures. Sapphire substrates are used in favor of their good surface quality, low electric conductivity and relatively high thermal conductivity (to reduce laser heating on the metallic samples). After the Permalloy nanomagnets are prepared, a second round of fabrication is conducted to make the excitation device (transmission lines) near the nanomagnets on the same wafer, to realize strong and damage-free excitations in contrast to the "flip-chip" scheme introduced in the last chapter. With minimal features of the transmission lines in few-μm scale, photolithography can be used, but the alignment will be very important and tricky because the mismatch created in a photomask aligner can easily go to several micrometers. Note that for best results, the two fabrication steps should not be swapped (i.e., it is not recommended to do photolithography first and then pattern nanomagnets on top of the transmission lines), since the sapphire surface may not be smooth and clean enough for fabricating small nanomagnets with EBL. Finally, since the TRMOKE setup is about to measure *individual* nanodisks, special points have to be considered in designing the samples, as elaborated below.

5.1.2. First lithography procedure.

1, Pattern designing for EBL: Fig.5-1 shows part of the patterns generated by L-Edit® (software available in Nanofab). This is a negative mask design, which means the red-color features will be deposited with materials (Permalloy for this project). The diameters of various nanodisks are shown. The distance between neighboring nanodisks is about 900 nm, hence their magnetic interactions can be neglected, and only one nanodisk will be imaged and measured by the probe laser beam. The larger ring structures and the numbers ("2", "3", "4", etc.) can help to identify the sample area in the magneto-optical measurements. Not shown in Fig.5-1 are four "corner" patterns to define this EBL area; they are large enough (~ 20 μm) for making alignment in the later photolithography procedure, which will be introduced in Section 5.1.4.

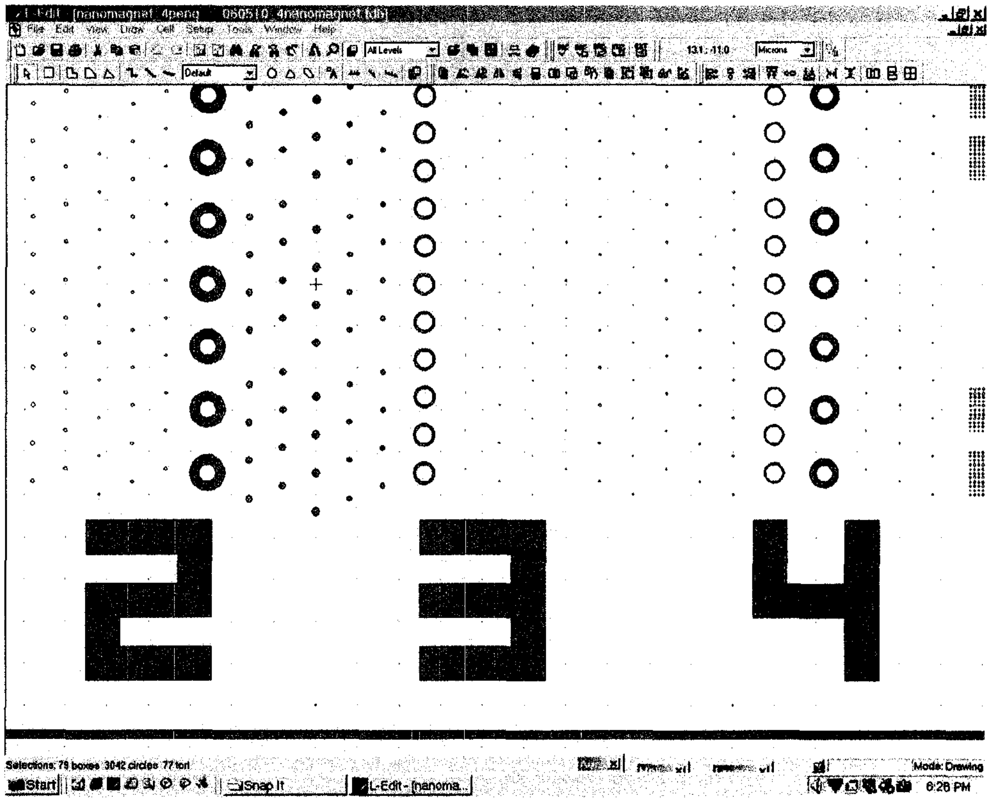

Fig. 5-1 (color): The workspace of L-Edit® showing part of the designed patterns for electron beam lithography. Sizes of the objects are determined by the small black points in the layout background which define a grid with 1 × 1 μm^2 square cells.

2, Brief procedure for EBL: As introduced in Section 3.2.4, two layers of EBL resists are successively spin-coated on a piranha-cleaned sapphire substrate. The substrate is then baked and sent into the Raith150 for electron beam exposure.

The programmed exposure is repeated for thirteen times at different positions on the substrate (see the schematic in Fig.5-2), but with various electron dosages. In this way, a few optimally exposed patterns can be found out of the thirteen units. After the exposure, the sample is developed using standard recipes. The resulted structures will exhibit "undercuts" due to different development rates of the two PMMA layers, so that the material deposited on the substrate will not directly contact with EBL resists to avoid possible damage in the subsequent lift-off process.

3, Metallization: Electron-beam evaporation is used to successively deposit Permalloy and gold (~ 2 nm as cap layer), as introduced in Chapter 3. The thickness of the film is 30 ± 3 nm as measured by the Alphastep 200 profilometer.

4, Lift-off: The sample is then immersed into acetone for about 15 minutes to remove the EBL resists. This lift-off procedure is carried out in an ultrasonic water bath to accelerate the removal.

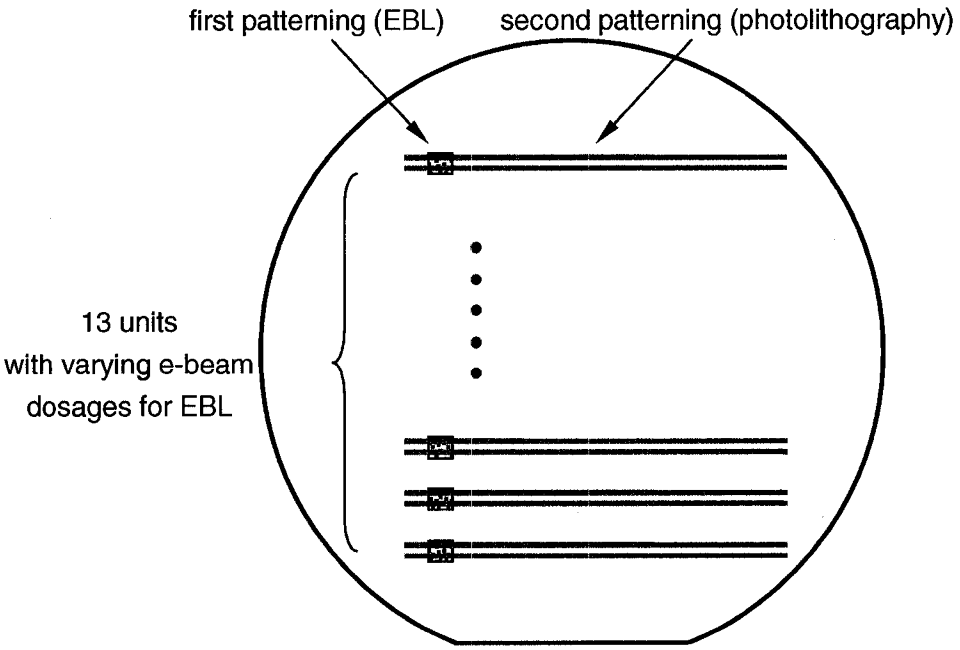

Fig. 5-2: Schematic of the samples on the 2-inch sapphire substrate. The small dotted boxes represent for the nanomagnets patterns made by EBL, and the grey lines are the transmission line structures fabricated in the followed photolithography step.

5.1.3. The second lithography procedure

The photolithography steps were introduced in Chapter 3, but used a different mask than that introduced in Chapter 4. The "kernel" part of the transmission lines (with two arms *parallel* to each other) was just 80 μm in length to cover the nanomagnet pattern area. Because the mask for patterning the transmission lines must be precisely aligned with the nanomagnet structures, specific markers were designed near the transmission lines according to the EBL patterns. It turned out that the alignment could be controlled within 3 μm (the width of the transmission lines), so that reasonably strong excitation is ensured.

5.1.4. Microscopy inspection of the integrated chip.

Fig.5-3 shows an image of the nanomagnet patterns (grey yellow) and the transmission lines (bright yellow), captured by the optical microscope in Nanofab. The alignment markers match fairly well. The width and separation of the two transmission lines are 3 μm.

Fig. 5-3 (color): Image of one of the nanomagnet samples captured by an optical microscope in the Nanofab.

Another sample was sent to the SEM in NINT for high-resolution inspection [NINTSEM]. About 2 nm gold was first sputtered on the entire sample to form a conductive surface (a standard step to avoid sample charging). An overview of the central part of the sample is shown in Fig.5-4(a), which is captured at a 45° tilting angle. There are some darker areas around individual disks, which are caused by zoom-in imaging with much slower scanning speed. The zoom-in images are shown in Fig.5-4(b-e). From the top views one can identify the diameters of the disks, as marked by the red arrows in Fig.5-4(b-d) (the numbers in the images are not very clear and are quoted in the figure caption). From these images one can observe a center-to-edge gradient in the thickness, such that the disks have a "domed" top. These features will be taken into account in later micromagnetic simulations.

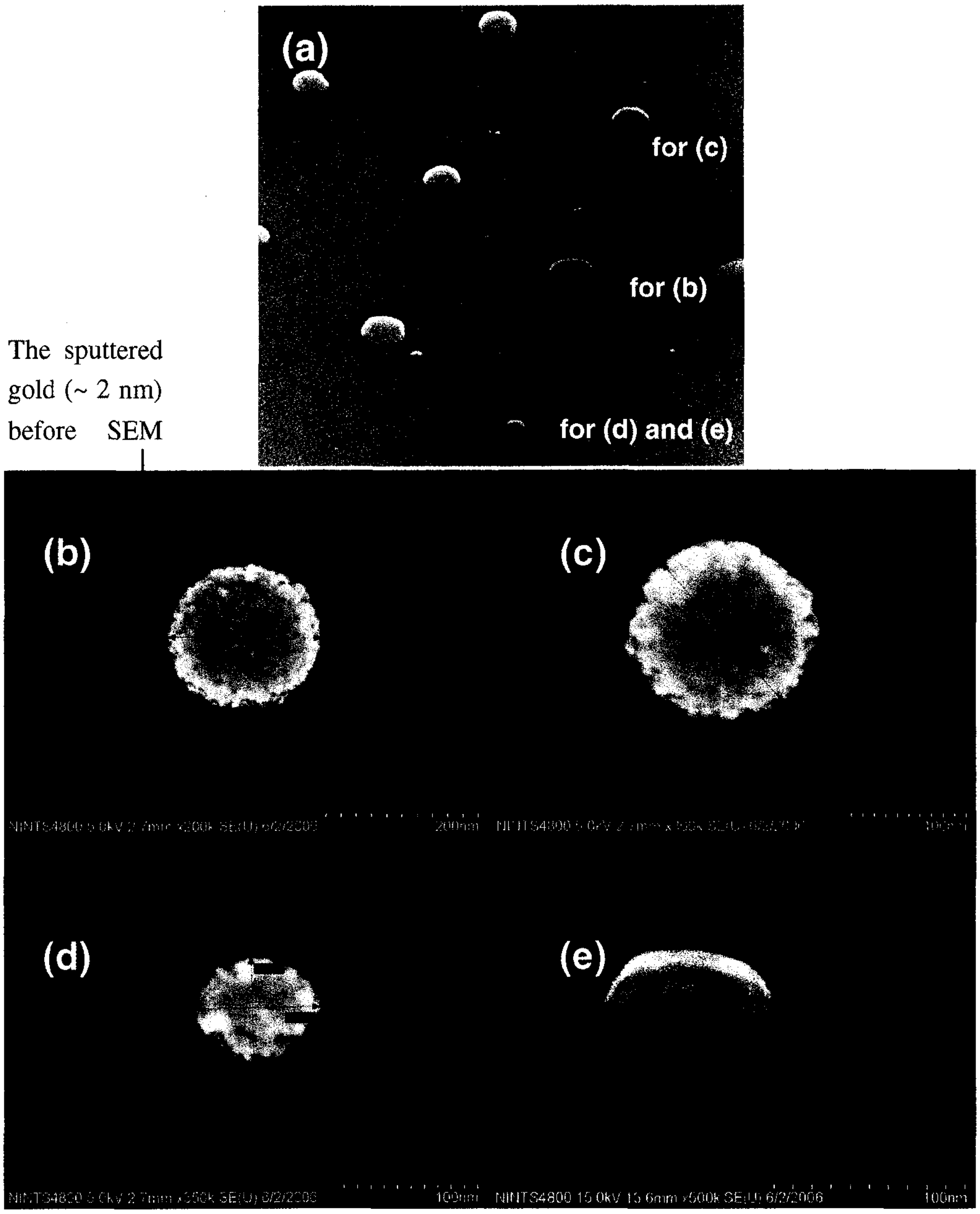

The sputtered gold (~ 2 nm) before SEM

Fig. 5-4 (color): SEM images of the Permalloy disks. **(a)**, Part of the sample captured at 45° tilted angle. The darkened areas are caused by the fine-imaging operations for results shown in (b-e). **(b)**, Top view of one of the disks shown in (a); its diameter is displayed by the SEM software, reading "202.9 nm". The designed size was 200 nm. **(c)**, Top view of one of the disks shown in (a) with diameter measured to be "164.5 nm". The designed size was 160 nm. **(d)**, Top view of an imperfect disk with one axis measured to be "96.4 nm" and the other reading "79.12 nm". The design size was 100 nm. **(e)**, 45° tilted image of the sample shown in (d).

5.1.5. TRMOKE setup and measurement

The magneto-optical measurements are similar with those introduced in the last chapter, except that the spatial scans are not to acquire spatiotemporal Kerr effect signals, but to optimize the focusing of the probe beam. This is done by repeating the scans with fine adjustment to the piezo-stage (along the axis of the objective lens) to find the largest contrast for the spatial intensity signals. A typical spatial image of individual Permalloy disks is shown in Fig.5-5(a). One can see that such optical scans are capable of resolving features smaller than 200 nm, even though the nearby gold transmission lines considerably overshadow the intensity signals from the Permally disks.

When the probe beam is properly focused, the spatial scans are stopped to leave the Permalloy disk at the center of the imaging area, so that the probe beam fully covers the disk. TRMOKE measurements (or "time scans") are then performed to obtain the spin dynamics data. A typical time trace is shown in Fig.5-5(b) (blue curve), and there is an obvious background due to electrical cross talk from the excitation source to the detector. This background can be reduced but not completely eliminated. If a second scan is immediately followed with the probing laser spot moved out of the nanomagnet (typically ~ 2 μm away by tuning the piezo-stage), the background signal can be recorded *without* the magnetic signal superimposed, as shown by the red curve in Fig.5-5(b). Then, by subtracting the two time traces (Fig.5-5(c)), the background can be cancelled out. The subtracted time trace is used in fast Fourier transform (FFT) analyses to obtain the frequencies of the disk's fundamental modes.

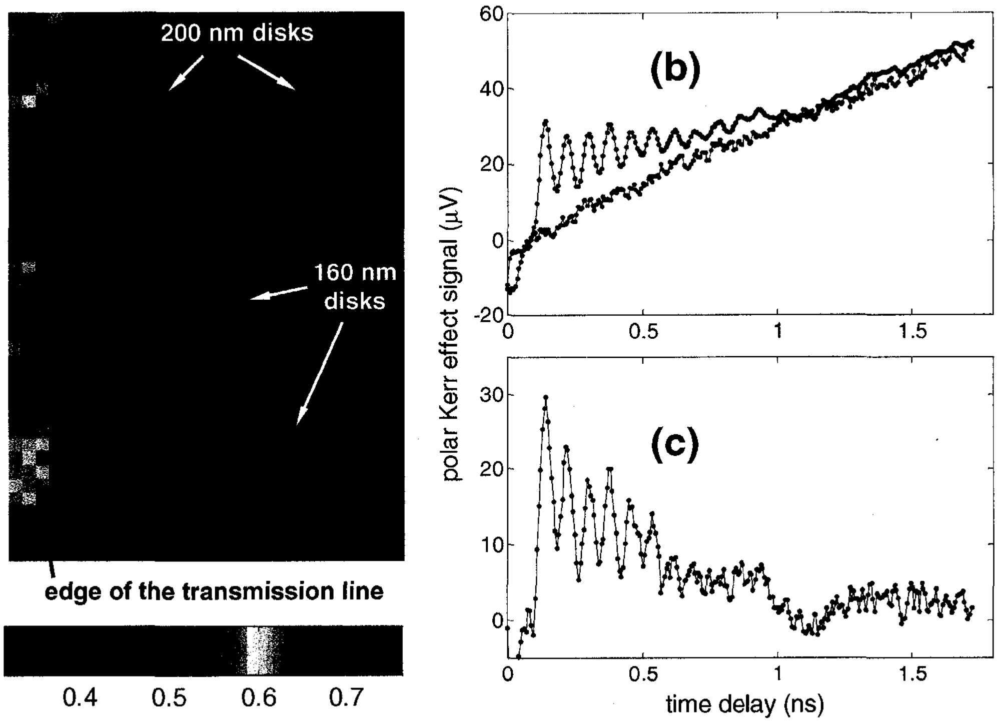

Fig. 5-5 (color): Typical operations to collect data from a single nanodisk. **(a)**, Image of the Permalloy disks by spatial intensity scanning of the TRMOKE system. The color bar represents the range of the normalized intensity signals (dimensionless). The center of this image (a 160 nm disk) is where the probe beam stays to take TRMOKE time scans shown in (b). **(b)**, The measured magnetic (blue) and background (red) signals by two successive time scans. **(c)**, Subtraction of the signals in (b).

5.2. Experimental results

5.2.1. Time-domain and frequency-domain results

Representative results measured by TRMOKE are shown in Fig.5-6. The Permalloy disk is in a single domain state when sufficiently saturated by a strong bias field (H_0 = 1200 Oe in Fig.5-6(a)), and the measured waveform is characterized by low-frequency, fairly coherent oscillations. When the bias field is very small (H_0 = 3 Oe in Fig.5-6(b)), the disk favors the vortex state with much higher mode frequencies. For certain intermediate bias fields, however, both states can be energetically stable such that entirely different dynamics can be observed under the same bias field (H_0 = 500 Oe in Fig.5-6(c-d)). This indicates that the evolution of the disk's ground state must exhibit a hysteresis behavior when the bias field is sweeping up and down in the described range. The most convenient way to investigate such hysteresis behavior is to plot the characteristic frequency of the dynamics (denoted as f_0) as a function of the bias field strength H_0. This requires the spectra of the measured waveforms, which are created by fast Fourier transform (FFT) and shown in the inset of each panel in Fig.5-6. The dynamics associated with quasi-single domain states usually shows a unique, shape peak in frequency domain, and this frequency is selected as f_0. The dynamics associated with vortex states, however, has relatively more complicated spectral profiles, with more than one peaks distributed in the range of 10 – 14 GHz. Although each of these frequencies is much higher than those in the quasi-single domain branch and can serve as an indicator for the vortex state, it is typically the largest frequency that possesses the largest spectral power, and is selected as f_0. Here, the determination of f_0's is for describing the evolution and transition of the ground states. More detailed investigations are needed to interpret the nature of these modes, and are presented in the Appendix of this Chapter with the help of micromagnetic simulation.

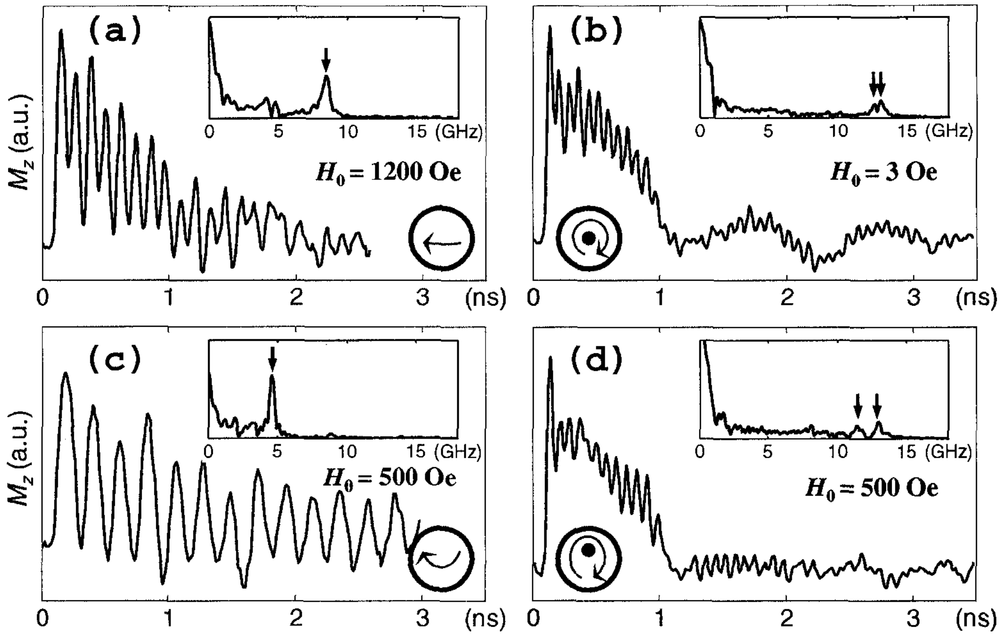

Fig. 5-6: Evolutions of M_z as a function of the pump-probe optical delay time measured under different bias fields and ground states (quasi-single domain **(a,c)** or vortex **(b,d)**), as illustrated by the cartoons in each panel. The power spectral densities (PSD) of the time traces are shown by the insets, with the arrows marking the characteristic frequencies as the indicator for state transitions discussed in the text.

5.2.2. Hysteresis behavior; vortex nucleation and annihilation.

The measured results for the f_0-H_0 relation are shown in Fig.5-7, showing the hysteresis loop. The two branches, for quasi-single domain and vortex states, are well separated. A frequency drop of ~ 10 GHz occurs when H_0 is increased up to ~ 850 Oe, indicating a vortex-to-single transition (vortex annihilation); when H_0 is then decreased (from high-field region) down to ~ 365 Oe, the frequency jumps up for ~ 5 GHz to register a single-to-vortex transition (vortex nucleation). The measurements were performed with multiple bias field sweepings, and the measured nucleation and annihilation fields varied with an uncertainty of ~ 10 Oe, and also had uncertainties of ~ 20 Oe for different disks. However, in a single sweeping cycle, it was observed that a transition can be spontaneously triggered when the bias field was *fixed* in the critical region. Fig.5-8(a) shows an example for H_0 being fixed at 847 Oe. Here one should be reminded that each 12-picosecond delay time step in the pump-probe measurement took about 4 seconds in real time, which is mainly determined by the operation time of the lock-in amplifier. So, before the moment recorded for the annihilation (marked by the small arrow), the vortex state was sustained for more than 10 minutes after the last change in the applied field. Similar behavior was also observed for the vortex nucleation process (Fig.5-8(b)). These observations suggest that there are no metastable intermediate states in terms of the change in bias fields and associated frequency shifts. These observations can only be achieved by measuring *individual* nanodisks; the transition events are stochastic in time and would produce incoherent temporal data if many disks were measured collectively.

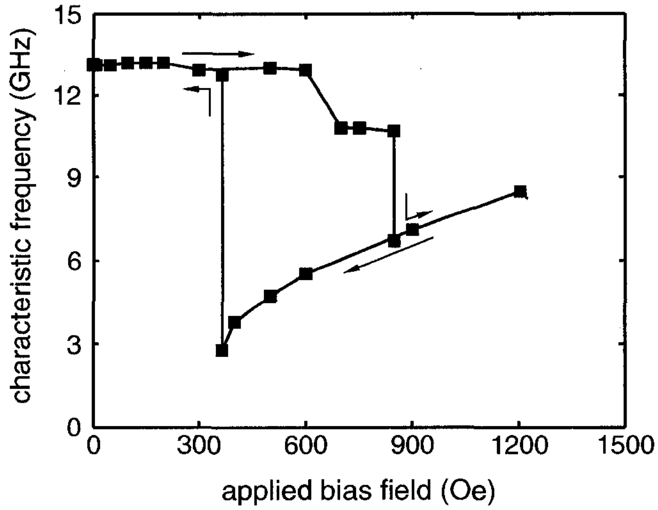

Fig. 5-7: Measured hysteresis behavior of the nanodisk's eigenfrequencies. The arrows indicate the sweeping history of the bias field.

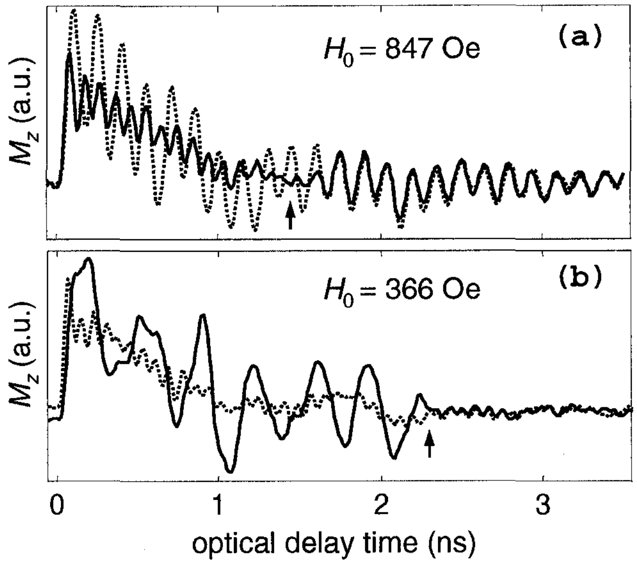

Fig. 5-8: Spontaneous transitions of vortex nucleation and vortex annihilation. **(a)**, the solid curve shows the temporal scan of M_z with an abrupt change in precession behavior, indicating a vortex-to-single transition (marked by the arrow); the dashed curve shows an immediately-followed scan to confirm the disk was already in the single state. The bias field was fixed at 847 Oe during the scans. **(b)**, similar consecutive scans for detecting a single-to-vortex transition. The bias field was fixed at 366 Oe.

5.3. Analytical and numerical calculations: comparison with experiment

5.3.1. Analytical approach for quasi-single domain states.

The eigenfrequency of an *infinite* thin film with a *perfect* single domain configuration can be expressed by the well-known Kittel's formula [Kittel1948, VanVleck1951]:

$$f_0 = \frac{\gamma_0}{2\pi}\sqrt{H_0^2 + 4\pi H_0 M_s} \qquad (5\text{-}1)$$

Guslienko *et al.* discussed the case when the thin film is spatially confined to form a flat cylinder shape, but is still in a perfect single domain state – which is a theoretical paradox often being a good enough approximation. This theory modifies the Kittel's equation as following:

$$f_0 = \frac{\gamma_0}{2\pi}\sqrt{H_0^2 + 4\pi H_0 M_s[1-3F(\beta)]} \qquad (5\text{-}2)$$

where *F*(*β*) is the effective demagnetizing factor for a cylinder with *β* equal to the thickness-to-radius ratio [Guslienko2000]. It basically says that the frequency will be lowered by the demagnetization energy, whose effect becomes more and more significant with increasing aspect ratio of the cylinder.

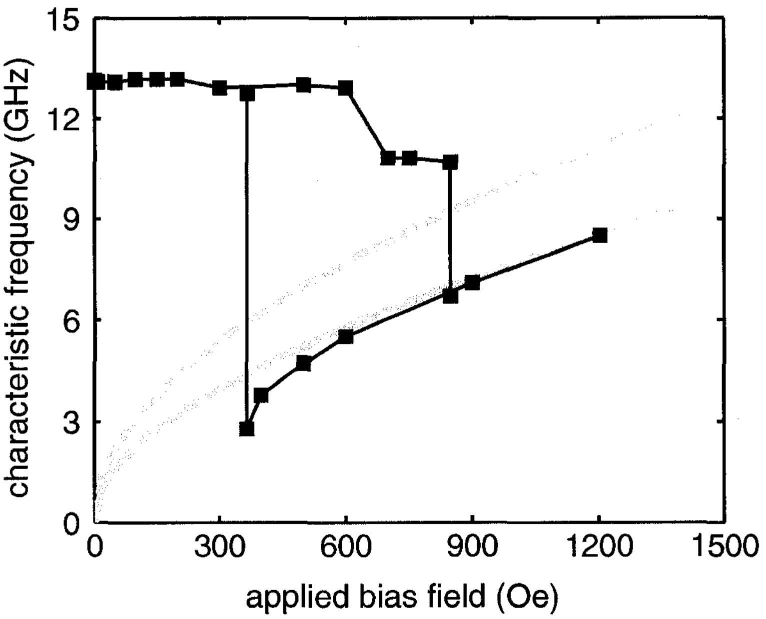

Fig. 5-9: Analytical results for hysteresis behavior of the nanodisk's eigenfrequencies. The grey curve is calculated based on Eq.(5-2) (for our samples, β = 0.375 and $F(\beta) \approx 0.1537$, see Ref.[Guslienko2000] for details); the grey dashed curve represents a reference calculation based on the unmodified Kittel's formula, Eq.(5-1), with $F(\beta) = 0$. The measured data in Fig.5-8 are also present for comparison.

In real samples, however, the magnetization can only be partially magnetized by a finite bias field to form a "quasi-single domain" state that can have either "C" shape or "S" shape [Rahm2003]. The demagnetization effect will then have extra influence to the eigen-frequency, especially when the bias field is not very strong. The calculated results with Eq.(5-1) and Eq.(5-2) are shown in Fig.5-9, together with the measured data points. The modified Kittel's formula fits the experiment fairly well, except for the low-H_0 region (near the critical field for vortex nucleation) where f_0 decreases "faster" than the theory, as expected.

5.3.2. Micromagnetic simulation results.

Analytical approaches for eigenfrequencies in vortex states and the state transition fields (H_{nu} and H_{an}) are also available [Guslienko2001], but their agreement with experiments is relatively coarse as compared to the quasi-single domain case. The following part of this section will present results by micromagnetic simulations for quantitative comparison.

Basic principles of LLG-based micromagnetic simulations have been introduced in Chapter 2, and the one-dimensional version has been used in Chapter 3. Here a three-dimensional version is used, and the shape of the Permalloy disk is defined by a controllable mask within a 64×64×8 grid; the cell size is about 2.6×2.6×3.8 nm^3. For a given bias field, the equilibrium state of the disk is obtained by free relaxation under a very large damping constant $\alpha = 1.8$ (for fast execution). The result can be used as the initial state for pulsed dynamics calculation, with the damping constant $\alpha = 0.008$ for the real material.

The frequency data can then be obtained by FFT analysis on the calculated waveforms. To investigate the vortex annihilation process, the system begins with a vortex state and undergoes a stepping stabilization. In each step, the bias field is increased by just 10 Oe or even smaller, so the critical field for triggering the vortex annihilation (H_{an}) can be found with fairly good accuracy. Similar approach is applied for vortex nucleation process, with the bias field stepping down to find H_{nu}.

The most simple and widely-used model for a nanodisk is a flat cylinder, with geometric symmetry along the out-of-plane direction (defined as the z-axis). Many theoretical and numerical studies have been using this model [Aharoni1990, Novosad2001, Rahm2003, Zaspel2005, Zivieri2005], and the simulations on the present work agree considerably well with some of those results. The simulated results using flat cylinder model are plotted by triangles in Fig.5-11, where the measured data are also there. It can be seen that although the simulated frequencies are consistent with the measurement, the state transitions are poorly described – the simulated annihilation field (~ 1150 Oe) is much larger than the measured value (~ 860 Oe). This discrepancy is unlikely to come from systematic errors in the calculation, because the other critical field for vortex nucleation is reproduced quite well (~ 350 Oe). Moreover, these simulated critical fields are fairly close to the published results by Guslienko *et al.* who also employed the flat cylinder model [Guslienko2001].

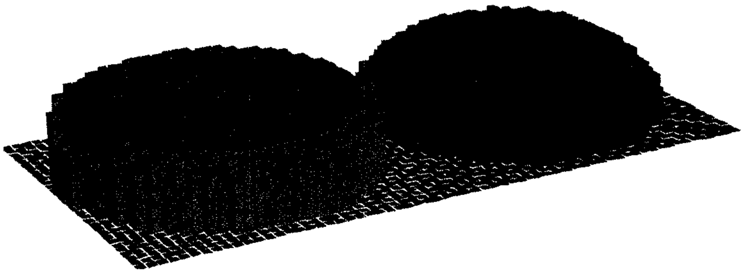

Fig. 5-10: The flat cylinder model and the domed cylinder model used in the micromagnetic simulations.

Therefore, some physical aspect must be missed with the flat cylinder model. Since the vortex annihilation takes place when the vortex core is pushed sufficiently close to the disk edge where it is destabilized geometrically, and then disappears, it is then reasonable to attribute the reduction of H_{an} to extra shape effect at the edge beyond the coverage of the flat cylinder model, so a "domed" cylinder model is proposed based on observation of the sample shape in Section 5.1.4. The flat and domed cylinder models are shown in Fig.5-10, which are 3D plot of the "mask" array for the simulations. Fig. 5-11 shows the simulated results using the domed cylinder model (circles), also with the measured data (squares), the analytical curves and the simulated results by the flat cylinder model (triangles). The annihilation field obtained by the domed cylinder model matches measurement very well, since now the vortex core can touch the disk edge at the top under a much lower bias field, resulting to the earlier annihilation.

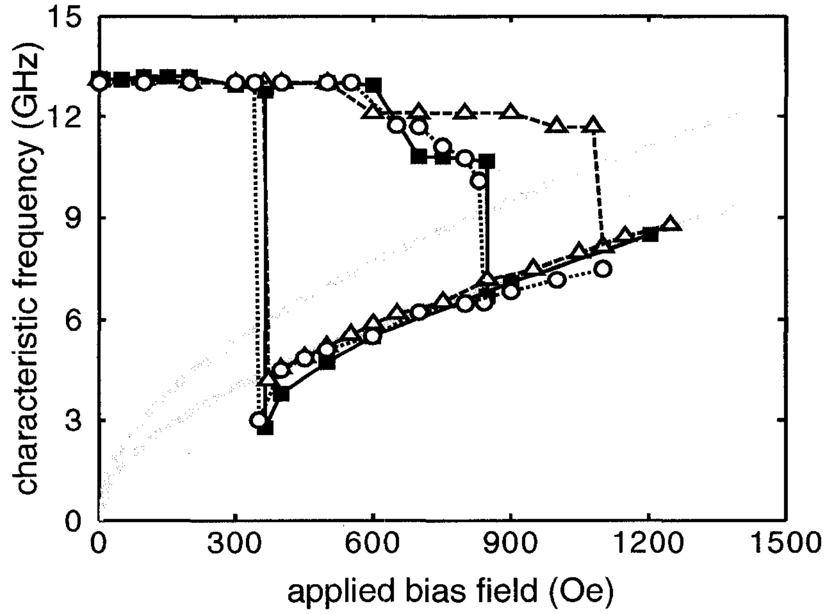

Fig.5-11: Simulation results for hysteresis behavior of the nanodisk's eigenfrequencies. The open circles and triangles are simulated with the domed cylinder model and the flat cylinder model, respectively. The measured data (squares) and the analytical results (grey curves) are also present for comparison, borrowed from Fig.5-8 and Fig.5-10, respectively.

The vortex annihilation process can be conveniently visualized by 3D snapshots of the magnetization configurations, as shown in Fig.5-12. It can be seen that there is a clear intermediate stage for the domed cylinder model where a big part of the vortex core has been destabilized (disappeared) near the top (Fig.5-12(b3)), but the bottom part still exists. For the flat cylinder model, however, the vortex core can sustain all over the thickness direction until a very abrupt annihilation occurs (see Fig.5-12(a3-a4))

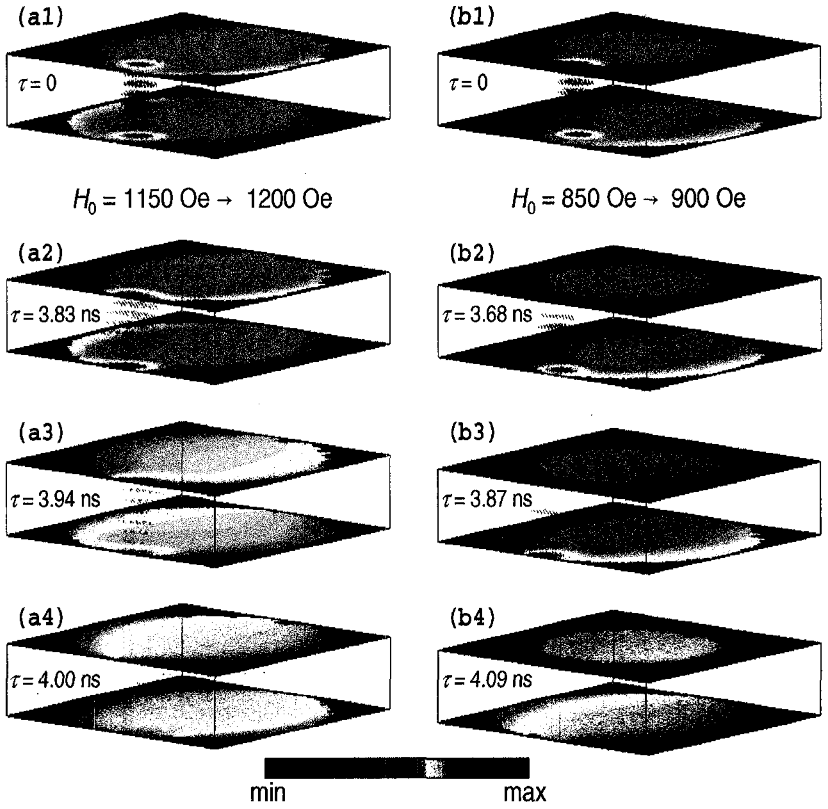

Fig. 5-12 (color): Evolution of magnetization configuration in the vortex annihilation process, simulated with the flat cylinder model (a1 – a4) and the domed cylinder model (b1 – b4). The disks are stabilized into equilibrium with H_0 = 850 Oe (a1) and 1150 Oe (b1), respectively. Then the bias fields increase to 900 Oe and 1200 Oe, respectively, to trigger the annihilation, and typical snapshots are recorded in (a2-a4) and (b2-b4). The τ values are the "effective" time in the simulations with a large damping α = 1.8, so these snapshots do not reflect real time points (in real time, the evolution would be much slower). In each frame, the M_z values at the top and bottom layers of the 3D models are shown by the colored surfaces; the color bar shows a fixed minimum value (-1, assigned for cells outside the disk) and different maximum values for different frames. The small cones between the two surfaces represent the spins *within* the vortex core (the criterion is at least 25° angle off the disk plane); the colors of these cones are also scaled with M_z.

Also shown in Fig.5-11 is the fact that both models produce consistent nucleation field as compared to the experimental value. This indicates that the nucleation process must be governed by a different mechanism that does not rely on changing the top shape of the disk. The simulated evolution of magnetization configurations at different times during vortex nucleation can be revealed by the 3D plots shown in Fig.5-13. In both models, the vortex core emerges from the bottom edge of the nanodisk (although for the flat cylinder model, the bottom and top sides are symmetric in geometry), while the spins near the top of the nanodisk still remain in quasi-single domain state, as can be seen in Fig.5-13(a2,b2); note in these two cases, the spins in the nucleation area just start popping out of the disk plane, and cannot be called as an explicit vortex. This "kernel" region then quickly grows up by involving more and more spins near the top edge of the nanodisk, during the time the spins rotate towards the *z*-axis to form a complete vortex core. Therefore, the early stage of the vortex nucleation has no geometric engagement with the domed top of the nanodisk, and this explains why the nucleation fields produced by the two models are fairly close. After the nucleation, the vortex core moves from the edge to its equilibrium location near the disk center, and its height increases when passing across the edge region (Fig.5-13(b3-b5)).

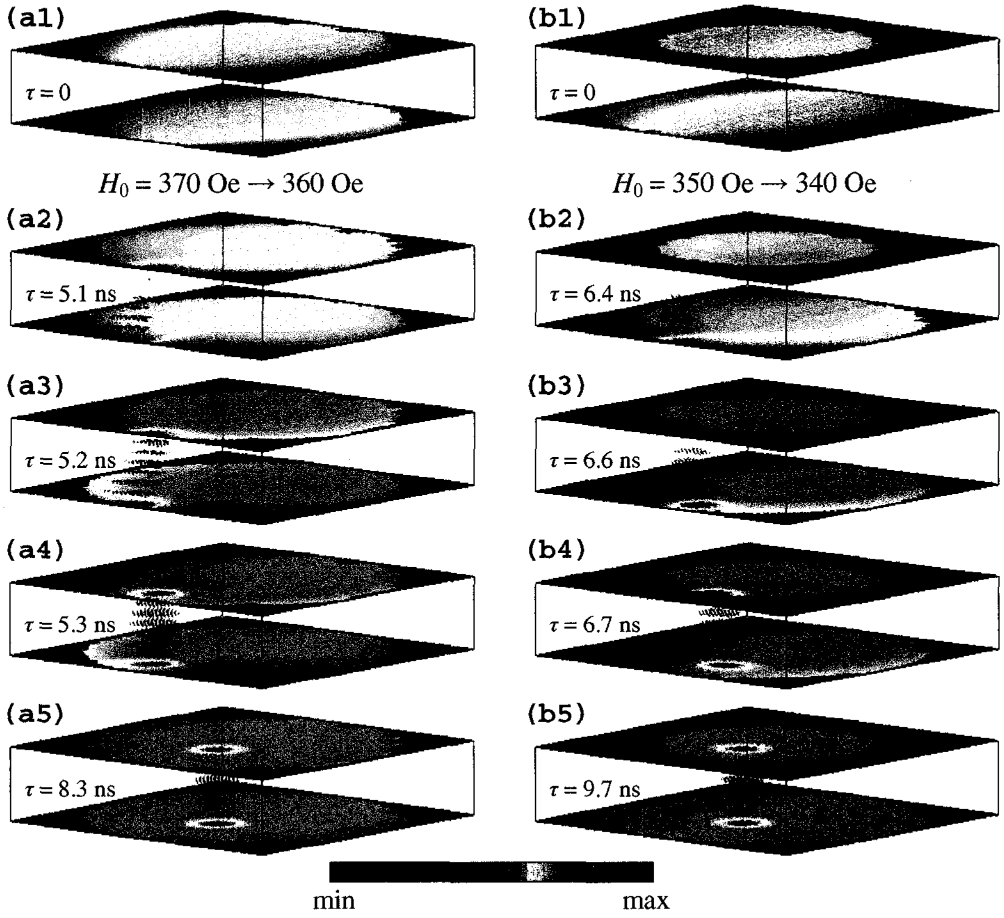

Fig. 5-13 (color): Evolution of magnetization configuration in the vortex nucleation process, simulated with the flat cylinder model (a1 – a5) and the domed cylinder model (b1 – b5). The disks are stabilized into equilibrium with H_0 = 370 Oe (a1) and 350 Oe (b1), respectively. Then the bias fields decrease to 360 Oe and 340 Oe, respectively, to trigger the nucleation, and typical snapshots are recorded in (a2-a5) and (b2-b5). Other features are the same as in Fig. 5-12.

Appendix 1 of Chapter 5:

Spatial distributions of the vortex-state modes (simulation results)

As mentioned in Section 5.2.1, the oscillation modes in the vortex state are more complicated than those in the quasi-single domain state, and magnetic dynamics must be examined with a good *spatial* resolution to figure out the modes' physical nature. However this is not feasible for the current magneto-optical techniques, as the diffraction limit of the probe beam (a few hundreds of nanometers) is much larger than the nanodisk itself. Micromagnetic simulations do not have such restrictions, though, and some typical results are presented in this section to provide a supplementary view.

Since the transmission lines are very close to the nanodisks being measured, both in-plane and out-of-plane components of the excitation pulse can affect the spin dynamics, which will lead to quite different spin wave patterns [Zhu2005PRB]. It is then reasonable to simulate them separately. Fig.5-14 gives the result for out-of-plane excitation under zero bias fields (using the domed cylinder model), and the magnetic response is fairly coherent (Fig.5-14(a)) with a clear peak at ~ 14.8 GHz in frequency domain (Fig.5-14(b)). The dynamics in each cell in the domed cylinder model can be separately Fourier transformed to obtain the magnitude and phase of the oscillations at this particular frequency. After being averaged over the thickness, the 2D distributions of the magnitude and phase can be plotted, as shown in Fig.5-14(c). Then, the real-time behavior of this mode can be reconstructed based on a simple sinusoid waveform:

$$A\sin(2\pi f t + \varphi)$$

Thus, the 14.8 GHz oscillations in all cells can be plotted together to make a movie; one can also add an exponential damping term to the waveform, but the main features of the mode distribution do not change much. This kind of movies cannot be shown here but the movie files (.avi) can be found in the accessory CD of this thesis. It turns out this mode does not have explicit azimuthal rotation around the vortex core [Buess2004, Buess2005, Neudecker2006], which is within expectation because the vortex core is at the disk center, and the out-of-plane pulse does not apply significant torque to the vortex core to break the system's symmetry [Zhu2005PRB].

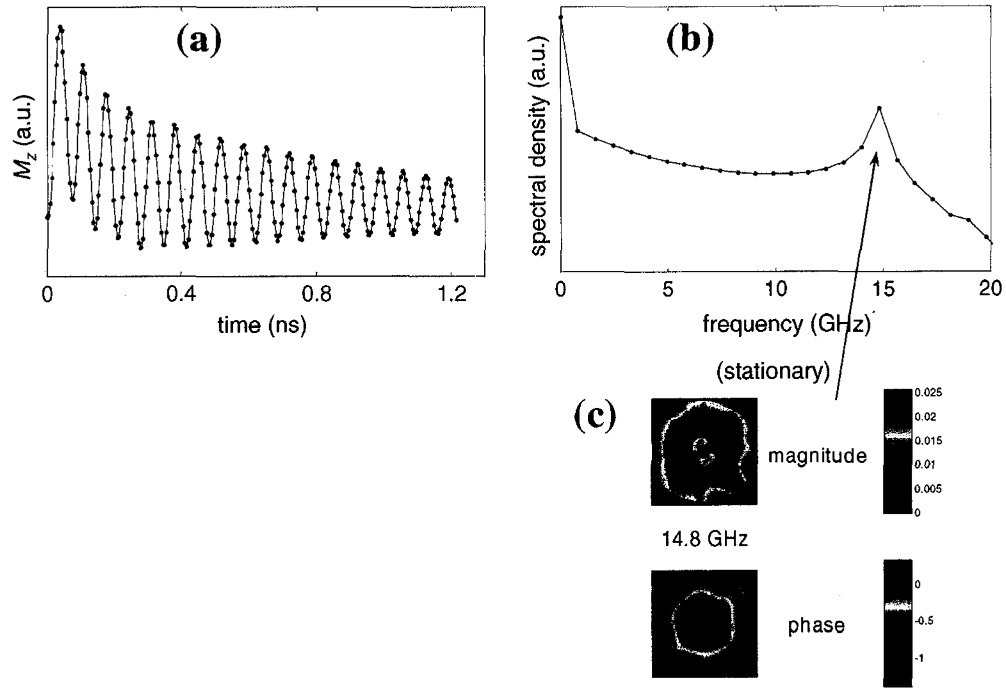

Fig. 5-14 (color): Simulated mode distribution of the vortex state when the excitation pulse is perpendicular to the nanodisk plane and $H_0 = 0$ Oe. The domed cylinder model is used. (a), Time evolution of M_z averaged over the entire disk. (b), Fourier spectrum of (a). (c), the spatial distribution of the 14.8 GHz mode. The top panel shows the magnitude and the bottom panel shows the phase, with color bars labeling their values. The text in the blue parenthesis mark means that the 14.8 GHz mode is not rotating around the vortex core (stationary), as can be seen in the movie stored in the accessory CD.

In the in-plane pulse case, however, the vortex core does have a significant torque due to the excitation pulse and a gyrotropic mode at ~ 1.5 GHz will be created. Consequently, the high-frequency (10 – 15 GHz) mode distributions show quite complicated profiles, with three splitting peaks (Fig.5-15(b)). The magnitude and phase distributions at different frequencies also show different patterns (Fig.5-15(c)); the modes at 12.1 GHz and 13.5 GHz clearly show some azimuthal nodes, indicating they are rotating around the vortex core. These are proved by the movies, and the two modes actually rotate in opposite directions (one clockwise and the other counter-clockwise). The highest-frequency mode (~ 14.7 GHz) is almost stationary, but compared to the one shown in Fig.(5-14), one still can find the difference caused by the vortex core motion.

One drawback of such simulation results is that they seem to be unable to explain the nonuniformity along the azimuthal direction, because the simulations are based on rectangular finite elements and it is usually not easy to exclude the "intrinsic" nonuniformity due to the zigzag edges (which is *not* physical), especially for such small disks.

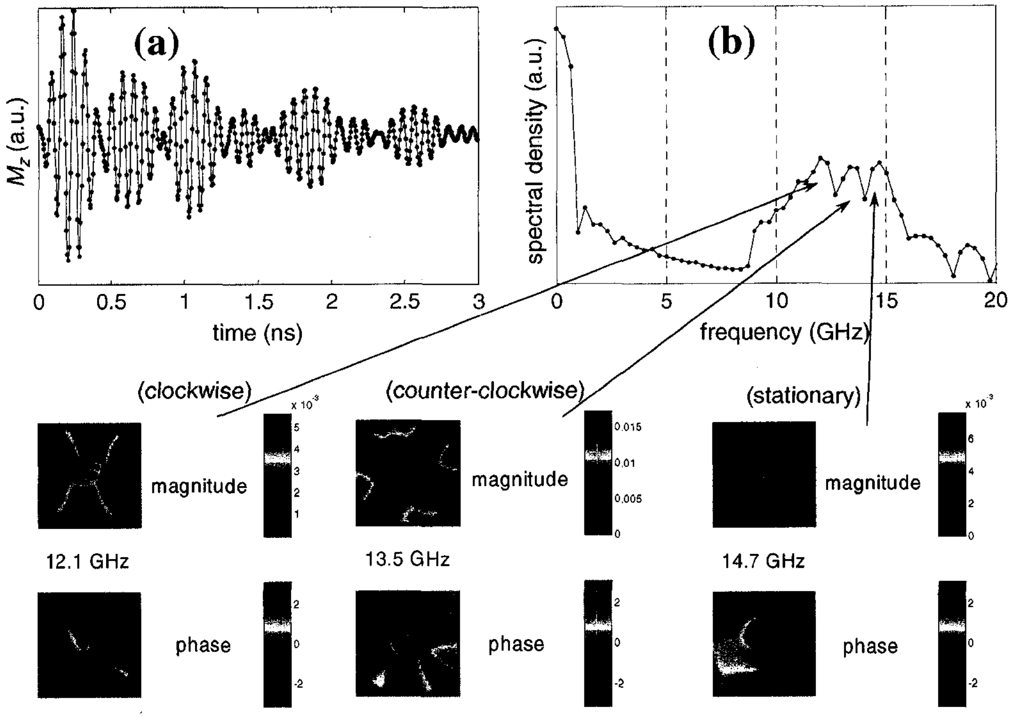

Fig. 5-15 (color): Simulated mode distribution of the vortex state when the excitation pulse is parallel to the nanodisk plane and $H_0 = 0$ Oe. (a), Time evolution of M_z averaged over the entire disk. (b), Fourier spectrum of (a). (c), the spatial distribution of the 14.8 GHz mode. The top panel shows the magnitude and the bottom panel shows the phase, with color bars labeling their values. The text in the blue parenthesis mark means that the 14.8 GHz mode is not rotating around the vortex core (stationary), as can be seen in the movie stored in the accessory CD.

Appendix 2 of Chapter 5:

A brief user guide to the FORTRAN codes for micromagnetic simulations

The FORTRAN codes for micromagnetic simulations were based on the work of previous colleagues, especially Greg Ballentine [Ballentine2003] and Miroslav Belov [Belov2004]. The codes can be found in the present author's Master thesis [Liu2003]; they were then upgraded from FORTRAN77 to FORTRAN95, plus various improvements, and now can be found in the accessory CD of this thesis. The program is saved in several FORTRAN files according to different purposes; their basic structures and functions are similar with those discussed in Ref.[Liu2003], and are briefly summarized below:

global.f: contains the global module; defines the variables and arrays; set mathematical and material parameters (sizes of the sample and the cells, saturation magnetization, temperature, damping constant, exchange stiffness coefficient, etc.).

sim3d.f: initializes the problem; receive preset data if necessary (e.g., resume a simulation from a previously initialized state). This data file is called "datapool.dat".

ode3d.f: runs the ODE solver; saves the results after each step and outputs if necessary.

rk3d.f: the ODE solver; performs self-adjustment to the time step.

deriv3d.f: calculates the exchange field; incorporates all components of the effective field into the LLG equation; define periodic boundary conditions if necessary.

demag3d.f: calculates the demagnetization field; calculates the anisotropy field and thermal-induced field if necessary.

init3d.f: the functions for calculating the external field and for initializing the problem (e.g., define the mask and initial magnetization configuration, calculate the components of the demagnetization tensor).

output3d.f: saves spatial configurations of the magnetization.

func3d.f: miscellaneous functions, such as the subroutine to calculate the components of averaged magnetization, and the formulas for calculating demagnetization tensors

Inside all these files, there are detailed comments to explain and specify the individual variables and operations, thus many tasks can be implemented by simple modifications to the codes.

Chapter 6:

Conclusion and outlook

Two types of experiments have been discussed in this thesis, both having very small spatial confinements (μm-scale excitation devices in Chapter 4 and 100-nm-scale ferromagnetic samples in Chapter 5). Time-resolved magneto-optical Kerr effect microscopy has proved to be an effective technique to detect how the ferromagnetic samples behave where those spatial confinements play a key role.

When the excited spin waves belong to the magnetostatic regime, it has been quantitatively verified that a single parameter is sufficient to describe the intrinsic damping of the magnetic system, although the damping behavior may appear differently at different locations due to the propagation of spin wave energy. The magnetostatic spin waves can be consistently described by a semi-analytical model (Eq.(4-1)), which is closely related to the spatial distribution of the excitation pulse; the calculations bear a same level of accuracy as those produced by micromagnetic simulations, but consume much less computational resources than the latter. This improvement enables us to conveniently *invert* the problem so that arbitrary magnetic waveforms can be “designed” for various spin wave applications.

When thin film magnetic samples are patterned down to 10^2 nm in size, the magnetization configuration at equilibrium will change depending on different conditions, such as the applied bias field, the shape of the nanomagnets, and their magnetic history. For the case of Permalloy nanodisks under studied, the spin dynamics associated with two equilibrium configurations – vortex state and quasi-single domain state – are totally different. The state transitions (vortex annihilation and vortex nucleation) can be detected by the abrupt changes of the waveforms or the modal frequencies. The critical bias fields to trigger such transitions have been determined, and evidences indicate that there is no intermediate or metastable phase between the two states (transitions can occur spontaneously when the bias field is fixed at certain values). When modeling the observed phenomena with micromagnetic simulations, it is found that the extensively used model (a flat cylinder) does not produce consistent critical bias fields as compared to the measurements; a modified domed cylinder model gives much better results, because more realistic shape effects are taken into consideration. These studies have important meaning in the applications dedicated to magnetic storage technologies, which utilize the different magnetic states to store and process information. For example, the read/write operations are typically realized through state transitions of selected magnetic elements (while keep some others "pinned"), whose critical fields are controlled by electric currents (command signals). The circuits then have to be carefully designed based on the nanomagnet state transitions discussed in Chapter 5 to avoid operation errors and to optimize the energy consumption of related devices.

Although TRMOKE is a well developed technique for looking inside tiny magnetic systems, its spatial resolution can hardly be smaller than 300 nm and starts to become incapable in the area of *nanomagnetism.* For example, as already mentioned in Chapter 5, the spatial distributions of the vortex-state modes cannot be measured at present, but have to resort to micromagnetic simulations. Today a number of new techniques begin to show promises of ultrafine spatial resolution in magnetic dynamics research, mostly relying on certain *local* probing schemes (in contrast to the normal far-field optical focusing), such as scanning tunneling microscopy (resolution < 1 nm), magnetic resonance force microscopy (< 1 nm), and electron holography based on transmission electron microscopy (< 10 nm). X-ray based microscopies (scanning transmission X-ray microscopy

(STXM) and X-ray photoemission electron microscopy (X-PEEM)) are now available for stroboscopic operation at several synchrotrons. In the optics community, there are also good opportunities for near-field scanning optical microscopy (NSOM) [Pohl1990, Levy1996a, Levy1996b, Petersen1998], which uses a very small optical fiber to detect the magnetic information, and the resolution has now reached 20 – 50 nm, depending on the fiber's quality. The measurement ability and the knowledge on nanoscale magnetic dynamics will likely be upgraded dramatically in the next several years.

Bibliography:

[Acremann2000], Acremann, Y., C. H. Back, M. Buess, O. Portmann, A. Vaterlaus, D. Pescia, and H. Melchior, "Imaging precessional motion of the magnetization vector", Science 290, 492 (2000).

[Aharoni1990], Aharoni, A., "Upper bound to a single-domain behavior of a ferromagnetic cylinder", J. Appl. Phys. 68, 2892 (1990).

[Arrott2005], Arrott, A. S., "Introduction to Micromagnetics", in "Ultrathin Magnetic Structures IV, Applications of Nanomagnetism", edited by Heinrich, B. and Bland, J. A. C., Springer (2005).

[Bailleul2001], Bailleul, M., D. Olligs, C. Fermon, and S. O. Demokritov, "Spin waves propagation and confinement in conducting films at the micrometer scale", Europhys. Lett. 56, 741 (2001).

[Bailleul2003], Bailleul, M., D. Olligs, and C. Fermon, "Propagating spin wave spectroscopy in a permalloy film: A quantitative analysis", Appl. Phys. Lett. 83, 972 (2003).

[Ballentine2003], Ballentine, G., "Comparison of time resolved micromagnetic dynamics experiments on $Ni_{80}Fe_{20}$ and Landau-Lifshitz-Gilbert micromagnetic simulation", Ph.D thesis, University of Alberta (2003).

[Barman2006], Barman, A., S. Wang, J. D. Maas, A. A.R. Hawkins, S. Kwon, A.

Liddle, J. Bokor, and H. Schmidt, "Magneto-optical observation of picosecond dynamics of single nanomagnets", Nano Letters 6, 2939 (2006).

[Beleggia2003a], Beleggia, M. and Y. Zhu, "Electron-optical phase shift of magnetic nanoparticles I. Basic concepts", Philos. Mag. 83, 1045 (2003).

[Beleggia2003b], Beleggia, M. and M. De Graef, "On the computation of the demagnetization tensor field for an arbitrary particle shape using a Fourier space approach", J. Magn. Magn. Mater. 263, L1 (2003).

[Beleggia2004], Beleggia, M., S.Tandon, Y.Zhu, and M.De Graef, "On the magnetostatic interactions between nanoparticles of arbitrary shape", J. Magn. Magn. Mater. 278, 270 (2004).

[Belov2004], Belov, M., "Spatiotemporal magnetization dynamics of patterned $Ni_{80}Fe_{20}$", Ph.D thesis, University of Alberta (2004).

[Berger1996], Berger, L., "Emission of spin waves by a magnetic multilayer traversed by a current", Phys. Rev. B 54, 9353 (1996).

[Binnig1986], Binnig, G., C. F. Quate, and Ch. Gerber, "Atomic force microscope", Phys. Rev. Lett. 56, 930 (1986).

[Bloch1930], Bloch, F., Z. Physik 61, 206 (1930).

[Bloch1946] Bloch, F., "Nuclear induction", Phys. Rev. 70, 460 (1946).

[Bloembergen1950], Bloembergen, N., "On the ferromagnetic resonance in Nickel and Supermalloy", Phys. Rev. 78, 572 (1950).

[Blois1955], Blois, M. S. Jr., "Preparation of thin magnetic films and their propertie", J. Appl. Phys. 26, 975 (1955).

[Bode1999], Bode, M., M Dreyer, M Getzlaff, M Kleiber, A Wadas, and R Wiesendanger, "Recent progress in high-resolution magnetic imaging using scanning probe techniques", J. Phys.: Condens. Matter 11, 9387 (1999).

[Bozorth1994], Bozorth, R. M., "Ferromagnetism", Wiley, New York, (1994).

[Brown1962], Brown, W. F. Jr., "Magnetostatic Principles in Ferromagnetism", North-Holland, Amsterdam, (1962).

[Brundle1968], Brundle, L. K. and N. J. Freedman, Electron. Lett. 4, 132 (1968).

[Buchanan2004], Buchanan, K. S., A. Krichevsky, M. R. Freeman, and A. Meldrum, "Magnetization dynamics of interacting iron nanocrystals in SiO_2", Phys. Rev. B 70, 174436 (2004).

[Buchanan2005], Buchanan, K. S., X. Zhu, A. Meldrum, and M. R. Freeman, "Ultrafast dynamics of a ferromagnetic nanocomposite", Nano Lett. 5, 383 (2005).

[Buess2004], Buess, M., R. Höllinger, T. Haug, K. Perzlmaier, U. Krey, D. Pescia, M. R. Scheinfein, D.Weiss, and C. H. Back, “Fourier transform imaging of spin vortex eigenmodes”, Phys. Rev. Lett. 93, 077207 (2005).

[Buess2005], Buess, M., T. Haug, M. R. Scheinfein, and C. H. Back, “Micromagnetic dissipation, dispersion, and mode conversion in thin Permalloy platelets”, Phys. Rev. Lett. 94, 127205 (2005).

[Choe2004], Choe, S. B., Y. Acremann, A. Scholl, A. Bauer, A. Doran, J. Stöhr, and H. A. Padmore, “Vortex core-driven magnetization dynamics”, Science 304, 420 (2004).

[Choi2001], Choi, B. C., M. Belov, W. K. Hiebert, G. E. Ballentine, and M. R. Freeman, “Ultrafast magnetization reversal dynamics investigated by time domain imaging”, Phys. Rev. Lett. 86, 728 (2001).

[Cottam2005], Cottam, M. G. and D. R. Tilley., “Introduction to surface and superlattice excitations 2nd edition”, IOP Publishing Ltd. (2005).

[Covington2002], Covington, M., T. M. Crawford, and G. J. Parker, “Time-resolved measurement of propagating spin waves in ferromagnetic thin films”, Phys. Rev. Lett. 89, 237202 (2002).

[Cowburn1999], Cowburn, R. P., D. K. Koltsov, A. O. Adeyeye, M. E. Welland, and D. M. Tricker, “Single-domain circular nanomagnets”, Phys. Rev. Lett. 83, 1042 (1999).

[Damon1961], Damon, R. W. and Eshbach, J. R., "Magnetostatic modes of a ferromagnet slab", J. Phys. Chem. Solids. 19, 308 (1961).

[Dekkers1974], Dekkers, N. H. and Lang, H., "Differential phase contrast in a STEM", Optik 41, 452 (1974).

[Demidov2004], Demidov, V. E., S. O. Demokritov, B. Hillebrands, M. Laufenberg, and P. P. Freitas, "Radiation of spin waves by a single micrometer-sized magnetic element", Appl. Phys. Lett. 85, 2866 (2004).

[Demokritov2006], Demokritov, S. O., V. E. Demidov, O. Dzyapko, G. A. Melkov, A. A. Serga, B. Hillebrands, and A. N. Slavin, "Bose-Einstein condensation of quasi-equilibrium magnons at room temperature under pumping", Nature 443, 430 (2006).

[DeWames1970], De Wames, R. E. and T. Wolfram, "Dipole-exchange spin waves in ferromagnetic films", J. Appl. Phys. 41, 987 (1970).

[Dzyapko2007], Dzyapko, O., V. E. Demidov, S. O. Demokritov, G. A. Melkov, and A. N. Slavin, "Direct observation of Bose–Einstein condensation in a parametrically driven gas of magnons", New J. Phys. 9, 64 (2007).

[Freiser1968], Freiser, M. J., "A survey of magnetooptic effects", IEEE Trans. Magn. MAG-4, 152 (1968).

[Fukushima1998], Fukushima, H., Y. Nakatani, and N. Hayashi, "Volume average demagnetizing tensor of rectangular prisms", IEEE Tran. Magn. 34, 193 (1998).

[Gerrits2002], Gerrits, Th., H. A. M. van den Berg, J. Hohlfeld, L. Bär, and Th. Rasing, "Ultrafast precessional magnetization reversal by picosecond magnetic field pulse shaping", Nature 418, 509 (2002).

[Gilbert1955], Gilbert, T. L., "A Lagrangian formulation of the gyromagnetic equation of the magnetization field", Phys. Rev. 100, 1243 (1955).

[Griffiths1946], Griffiths, J. H. E., Nature 158, 670 (1946).

[Gurevich1996], Gurevich, A. G. and G. A. Melkov, "Magnetization oscillations and waves", CRC Press, New York (1996).

[Guslienko2000], Guslienko, K. Yu., A. N. Slavin, "Spin-waves in cylindrical magnetic dot arrays with in-plane magnetization", J. Appl. Phys. 87, 6337 (2000).

[Guslienko2001], Guslienko, K. Yu., V. Novosad, Y. Otani, H. Shima, and K. Fukamichi, "Magnetization reversal due to vortex nucleation, displacement, and annihilation in submicron ferromagnetic dot arrays", Phys. Rev. B 65, 024414 (2001).

[Guslienko2005], Guslienko, K. Yu., W. Scholz, R. W. Chantrell, and V. Novosad, "Vortex-state oscillations in soft magnetic cylindrical dots", Phys. Rev. B, 71, 144407 (2005).

[Hayashi1996], Hayashi, N., K. Saito, and Y. Nakatani, “Calculation of demagnetizing field distribution based on fast Fourier transform of convolution”, Jpn. J. Appl. Phys. 35, 6065 (1996).

[Herring1951], Herring, C. and Kittel, C., “On the theory of spin waves in ferromagnetic media”, Phys. Rev. 81, 869 (1951).

[Heumann2005], M. Heumann, T. Uhlig, and J. Zweck, “True single domain and configuration-assisted switching of submicron permalloy dots observed by electron holography”, Phys. Rev. Lett. 94, 077202 (2005).

[Hiebert1997], Hiebert, W. K., A. Stankiewicz, and M. R. Freeman, “Direct observation of magnetic relaxation in a small permalloy disk by time-resolved scanning Kerr microscopy”, Phys. Rev. Lett. 79, 1134 (1997).

[Jackson1975], Jackson, J. D., Classical Electrodynamics”, John Wiley, New York, (1975).

[Jausovec2006], Jausovec, A. V., G. Xiong, and R. P. Cowburn, “Cycle-by-cycle observation of single-domain-to-vortex transitions in magnetic nanodisks”, Appl. Phys. Lett. 88, 052501 (2006).

[Johnson2005], Johnson, M., “Spintronics”, J. Phys. Chem. B 109, 14278 (2005).

[Kalinikos1986], Kalinikos, B. A. and A. N. Slavin, "Theory of dipole-exchange spin wave spectrum for ferromagnetic films with mixed exchange boundary conditions", J. Phys. C 19, 7013 (1986).

[Kirtley1995], Kirtley, J. R., M. B. Ketchen, C. C. Tsuei, J. Z. Sun, W. J. Gallagher, Lock See Yu-Jahnes, A. Gupta, K. G. Stawiasz, and S. J. Wind, "Design and applications of a scanning SQUID microscope", IBM J. Res. & Dev., 39, 6 (1995).

[Kirtley1999], Kirtley, J. R. and J. P. Wikswo, Jr., "Scanning SQUID microscopy", Annu. Rev. Mater. Sci. 29, 117 (1999).

[Kittel1948], Kittel, C., "On the theory of ferromagnetic resonance absorption", Phys. Rev. 73, 155 (1948).

[Krivorotov2005], Krivorotov, I. N., N. C. Emley, J. C. Sankey, S. I. Kiselev, D. C. Ralph, and R. A. Buhrman, "Time-domain measurements of nanomagnet dynamics driven by spin-transfer torques", Science 307, 228 (2005).

[Kruglyak2005], Kruglyak, V. V., A. Barman, R. J. Hicken, J. R. Childress, and J. A. Katine, "Precessional dynamics in microarrays of nanomagnets", J. Appl. Phys., 97, 10A706 (2005)

[Landau1935], Landau, L. and E. Lifshitz, "On the theory of the dispersion of magnetic permeability in ferromagnetic bodies", Physik. Z. Sowjetunion 8, 153 (1935).

[Levy1996a], Levy, J., Nikitin, V., Kikkawa, J. M., Awschalom, D. D., "Femtosecond near-field spin microscopy in digital magnetic heterostructures", J. Appl. Phys. 79, 6095 (1996).

[Levy1996b], Levy, J., Nikitin, V., Kikkawa, J. M., Cohen, A., Awschalom, D. D., Samarth, N., and Garcia, R., "Spatiotemporal Near-Field Spin Microscopy in Patterned Magnetic Heterostructures", Phys. Rev. Lett. 76, 1948 (1996).

[Lewis1964], Lewis, B., "The Permalloy problem and anisotropy in nickel-iron magnetic films", Brit. J. Appl. Phys. 15, 531 (1964).

[Liu2003], Liu, Z., "Micromagnetic simulations on $Ni_{80}Fe_{20}$ thin film microstructures", Master thesis, University of Alberta (2003).

[Liu2007], Liu, Z., F. Giesen, X. Zhu, R. D. Sydora, and M. R. Freeman, "Spin wave dynamics and the determination of intrinsic damping in locally excited Permalloy thin films", Phys. Rev. Lett. 98, 087201 (2007).

[Mansuripur1988], Mansuripur, M., "Magnetization reversal dynamics in the media of magneto-optical recording", J. Appl. Phys. 63, 12 (1988).

[Mansuripur1995], Mansuripur, M., "The physical principles of magneto-optic recording", Cambridge University Press (1995).

[Markos1994], Markos, M., Scheinfein, M. R., and Cowley, J. M., "Absolute magnetometry at nanometer transverse spatial resolution: Holography of thin cobalt films in a scanning transmission electron microscope", J. Appl. Phys. 75, 7418 (1994).

[Miltat2002], Miltat, J., G. Albuquerque, and A. Thiaville, "An introduction to micromagnetics in the dynamic regime", in "Spin dynamics in confined magnetic structures I", edited by B. Hillebrands and K. Ounadjela, Springer, New York (2002).

[Nakatani1989], Nakatani, Y., Y. Uesaka, and N. Hayashi, "Direct solution of the Landau-Lifshitz-Gilbert equation for micromagnetics", Jpn. J. Appl. Phys. 28, 2485 (1989).

[Neudecker2006a], Neudecker, I., M. Kläui, K. Perzlmaier, D. Backes, L. J. Heyderman, C. A. F. Vaz, J. A. C. Bland, U. Rüdiger, and C. H. Back, "Spatially resolved dynamic eigenmode spectrum of Co rings", Phys. Rev. Lett. 96, 057207 (2006).

[Neudecker2006b], Neudecker, I., K. Perzlmaier, F. Hoffmann, G. Woltersdorf, M. Buess, D. Weiss, and C. H. Back, "Modal spectrum of permalloy disks excited by in-plane magnetic fields", Phys. Rev. B 73, 134426 (2006).

[Newell1993], Newell, A. J., W. Williams, and D. J. Dunlop, "A generalization of the demagnetizing tensor for non-uniform magnetization", J. Geophys. Res. 98, 9551 (1993).

[NINTSEM], NINT's Hitachi S4800 SEM is introduced through the following links: http://nint-innt.nrc-cnrc.gc.ca/facilities/elec_microscopy_e.html; http://www.hhtc.ca/microscopes/sem/s4800.htm

[Novosad2001], Novosad, V., K. Yu. Guslienko, H. Shima, Y. Otani, K. Fukamichi, N. Kikuchi, O. Kitakami, and Y. Shimada, "nucleation and annihilation of magnetic vortices in sub-micron Permalloy dots", IEEE Trans. Magn. 37, 2088 (2001).

[Palacios1998], García-Palacios, J. L. and F. J. Lázaro, "Langevin-dynamics study of the dynamical properties of small magnetic particles", Phys. Rev. B 58, 22 (1998).

[Park2002], Park, J. P., P. Eames, D. M. Engebretson, J. Berezovsky, and P. A. Crowell, "Spatially resolved dynamics of localized spin-wave modes in ferromagneticwires", Phys. Rev. Lett. 89, 277201 (2002).

[Perzlmaier2005], Perzlmaier, K., M. Buess, C. H. Back, V. E. Demidov, B. Hillebrands, and S. O. Demokritov, "Spin-wave eigenmodes of Permalloy squares with a closure domain structure", Phys. Rev. Lett. 94, 057202 (2005).

[Petersen1998], Petersen, B. L., A. Bauer, G. Meyer, T. Crecelius, and G. Kaindl, "Kerr-rotation imaging in scanning near-field optical microscopy using a modified Sagnac interferometer", Appl. Phys. Lett. 73, 538 (1998).

[Pohl1990], Pohl, D.W., "Scanning near-field optical microscopy", in Advances in

Optical and Electron Microscopy 12, Edited by Sheppard, C. J. R. and Mulvey, T., Academic Press, London (1990).

[Press1992], Press, W. H., S. A. Teukolsky, W. T. Vetterling, and B. P. Flannery, "Numerical recipes in Fortran 77: the art of scientific computing, 2nd edition", Cambridge University Press (1992).

[Pribiag2007], Pribiag, V. S., I. N. Krivorotov, G. D. Fuchs, P. M. Braganca, O. Ozatay, J. C. Sankey, D. C. Ralph, and R. A. Buhrman, "Magnetic vortex oscillator driven by dc spin-polarized current", cond-mat/0702253v1.

[Rahm2003], Rahm, M., M. Schneider, J. Biberger, R. Pulwey, J. Zweck, D. Weiss, and V. Umansky, "Vortex nucleation in submicrometer ferromagnetic disks", Appl. Phys. Lett. 82, 4110 (2003).

[Rugar2004], Rugar, D., R. Budakian, H. J. Mamin, and B. W. Chui, "Single spin detection by magnetic resonance force microscopy", Nature 430, 329 (2004).

[Scheinfein1991], Scheinfein, M. R., J. Unguris, J. L. Blue, K. J. Coakley, D. T. Pierce, R. J. Celotta, and P. J. Ryan, "Micromagnetics of domain walls at surfaces", Phys. Rev. B 43, 3395 (1991).

[Scholz2003], Scholz, W., K.Yu. Guslienko, V. Novosad, D. Suess, T. Schrefl, R.W. Chantrell, and J. Fidler, "Transition from single-domain to vortex state in soft magnetic cylindrical nanodots", J. MMM 266, 155 (2003).

[Schumacher2003a], Schumacher, H. W., C. Chappert, P. Crozat, R. C. Sousa, P. P. Freitas, J. Miltat, J. Fassbender, and B. Hillebrands, "Phase coherent precessional magnetization reversal in microscopic spin valve elements", Phys. Rev. Lett. 90, 017201 (2003).

[Schumacher2003b], Schumacher, H. W., C. Chappert, R. C. Sousa, P. P. Freitas, and J. Miltat, "Quasiballistic magnetization reversal", Phys. Rev. Lett. 90, 017204 (2003).

[Seo2005], Seo, Y., P. C. Zimansky, and V. Chandrasekhar, "Low-temperature high-resolution magnetic force microscopy using a quartz tuning fork", Appl. Phys. Lett. 87, 103103 (2005).

[Sidles1992], Sidles, J. A., J. L. Barbini, and G. P. Drobny, "The theory of oscillator-coupled magnetic resonance with potential applications to molecular imaging", Rev. Sci. Instrum. 63, 3881 (1992).

[Silva1999], Silva, T. J., C. S. Lee, T. M. Crawford, and C. T. Rogers, "Inductive measurement of ultrafast magnetization dynamics in thin-film Permalloy", J. Appl. Phys. 85, 7849 (1999).

[Silva2002], Silva, T. J., M. R. Pufall, and P. Kabos, "Nonlinear magneto-optic measurement of flux propagation dynamics in thin Permalloy films", J. Appl. Phys. 91, 1066 (2002).

[Slonczewski1996], Slonczewski, J. C., "Current-driven excitation of magnetic multilayers", J. Magn. Magn. Mater. 159, L1 (1996).

[Smith1958], Smith, D. O., "Magnetization reversal and thin films: static and dynamic behavior of thin Permalloy films", J. Appl. Phys. 29, 264 (1958).

[Suhl1998], Suhl, H., "Theory of the magnetic damping constant", IEEE Trans. Magn. 34, 1834 (1998).

[Tandon2004], Tandon, S., M. Beleggia, Y. Zhu, and M. De Graef, "On the computation of the demagnetization tensor for uniformly magnetized particles of arbitrary shape", J. Magn. Magn. Mater. 271, 9-26 and 27-38 (2004).

[VanVleck1951], Van Vleck, J. H., "Ferromagnetic resonance", Physica 17, 234 (1951).

[Walker1957], Walker, L. R., "Magnetostatic modes in ferromagnetic resonance", Phys. Rev. 105, 390 (1957).

[Wernsdorfer2000], Wernsdorfer, W., R. Sessoli, A. Caneschi, and D. Gatteschi, A. Cornia, and D. Mailly, "Landau–Zener method to study quantum phase interference of Fe_8 molecular nanomagnets (invited)", J. Appl. Phys. 87, 5481 (2000).

[Woods2001], Woods, S. I., J. R. Kirtley, Shouheng Sun, and R. H. Koch, "Direct investigation of superparamagnetism in Co nanoparticle films", Phys. Rev. Lett. 87, 137205 (2001).

[Wu2006], Wu, M., B. A. Kalinikos, P. Krivosik, and C. E. Patton, "Fast pulse-excited spin waves in yttrium iron garnet thin films", J. Appl. Phys. 99, 013901 (2006).

[Xia1998], Xia, H., P. Kabos, R. A. Staudinger, C. E. Patton, and A. N. Slavin, "Velocity characterizatics of microwave-magnetic-envelope solitons", Phys. Rev. B 58, 2708 (1998).

[Yager1950], Yager, W. A., J. K. Galt, F. R. Merritt, and E. A. Wood, "Ferromagnetic resonance in Nickel Ferrite", Phys. Rev. 80, 744 (1950).

[Zaspel2005], Zaspel, C. E., B. A. Ivanov, J. P. Park, and P. A. Crowell, "Excitations in vortex-state permalloy dots", Phys. Rev. B 72, 024427 (2005).

[Zhu2005APL], Zhu, X., M. Malac, Z. Liu, H. Qian, V. Metlushko, and M. R. Freeman, "Broadband spin dynamics of Permalloy rings in the circulation state", Appl. Phys. Lett. 86, 262502 (2005).

[Zhu2005PRB], Zhu, X., Z. Liu, V. Metlushko, P. Grütter, and M. R. Freeman, "Broadband spin dynamics of the magnetic vortex state: effect of the pulsed field direction", Phys. Rev. B 71, 180408(R) (2005).

[Zhu2005JAP], Zhu, X., C. Blois, K. S. Buchanan, Z. Liu, A. Meldrum, and M. R. Freeman, "Thermal annealing effect on the magnetic properties of Fe nanoparticles implanted into single-crystal yttrium stabilized zirconia", J. Appl.

Phys. 97, 10A720 (2005).

[Zivieri2005], Zivieri, R. and F. Nizzoli, "Theory of spin modes in vortex-state ferromagnetic cylindrical dots", Phys. Rev. B 71, 014411 (2005).

[Zutic2004], Žutić, I., Fabian, J., Das Sarma, S., "Spintronics: Fundamentals and applications", Rev. Mod. Phys. 76, 323 (2004).